# Quantum plasma simulation with a Bohmian smoothed particle hydrodynamic framework


Thomas I. F. Campbell

New College

University of Oxford

Work submitted for the degree of

*Doctor of Philosophy in Atomic and Laser Physics*

Michaelmas, 2024

*For my parents, Leslie and Christine.*

## Abstract

A novel approach to the modelling of quantum plasmas on the electronic timescale is presented in this work, Bohm SPH. The primary purpose of Bohm SPH is to investigate the structural and dynamical properties of warm dense matter, encountered in inertial confinement fusion implosions and certain astrophysical environments. With strong ionic coupling and quantum mechanical electrons, the simulation of warm dense matter presents a formidable challenge. Moving beyond the Born-Oppenheimer approximation applied by the widely used DFT-MD, electron dynamics are included explicitly in Bohm SPH. This is done without enormous computational expense and in a highly parallelisable code structure, enabling the investigation of large warm dense matter systems over ionic timescales at electronic time resolution. Given the novelty of the model and the approximations applied, particularly the use of a smoothed particle hydrodynamic scheme to resolve the electron density and a quantum hydrodynamic Bohm pressure, much of the work involves describing its construction, implementation, and modular validation. In two subsequent chapters, Bohm SPH is tasked with calculating the dynamic structure properties of warm dense hydrogen and the relaxation of non-thermal electrons in an XFEL-generated aluminium plasma, where it has success when the degrees of freedom of the model are properly considered.

# Table of Contents

# List of Figures

# List of Tables

# Chapter 1

# Introduction

An oft-quoted statistic is that more than 99% of visible matter in the Universe exists in the plasma state. At least this is often quoted within the plasma physics department. Nonetheless, it caught my eye when selecting courses in the third year of my undergraduate degree, and captured me sufficiently to continue into graduate study. To have a robust understanding of the contents of our Universe, stars, the interstellar medium, even planetary interiors, is to understand the behaviour of plasmas, across vast regimes of temperature and density.

Plasma, in a physics context, is considered the fourth state of matter. The essential distinction to its more familiar solid, liquid, and gas counterparts, is that electrons have been (at least partially) ionised from the atoms, such that we now have free charged particles, positive ions and negative electrons, interacting through electromagnetic forces. Although only a simple distinction, it unlocks a huge array of complex, collective phenomena.

A significant motivator for plasma physics research is the prospect of harnessing nuclear fusion, the process which powers stars, as a sustainable power source on Earth. We need a few of those. These fusion reactions take place within a plasma state. While abundant in the cosmos, plasma is more elusive on Earth. Lightning is one

dramatic example, the charged particles that stream along the Earth's magnetic field lines and ultimately produce the ethereal light shows we know as the aurorae, are another. Arguably, fire might also be considered as plasma, although there are nuances over when exactly there are sufficient free ions and electrons for it to qualify. Semantics aside, what is certain is that we require highly specialised facilities to generate plasma at the correct conditions and to confine it in place long enough for fusion reactions to occur. Two leading approaches have been adopted: magnetic confinement, where (sparse) plasma is confined via strong magnetic fields (for example in a tokamak or stellarator), or inertial confinement, where the (dense) plasma's own inertia keeps it localised. Inertial confinement fusion is driven, directly or indirectly, by powerful lasers, whose invention in the 1960s and continual refinement since have made a wealth of plasma states accessible in the laboratory.

I am fortunate to have explored a range of laser-generated plasma projects in the course of my DPhil, both theoretical and experimental. Generally these have been concerned with dense plasma systems where quantum mechanical effects are important in determining the electronic behaviour, but there have been some sizeable diversions. Such diversions include: conducting an experiment on fast ions traversing magnetic field structures (with analogies to cosmic rays), the design of x-ray diagnostics and associated algorithms, and consideration of relativistic effects in molecular dynamics codes. This is reflected in the somewhat eclectic collection of publications in Section 1.3.

Ultimately, the main thrust of my research has been the development of a new code for simulating warm dense matter, a type of quantum plasma. The code includes an approximate quantum mechanical treatment of the electrons, full energy exchange between the ions and electrons, and is computationally tractable. It is called Bohm Smoothed Particle Hydrodynamics (Bohm SPH) according to its theoretical underpinning. The development, validation, and application of Bohm SPH constitutes the

entirety of this thesis.

## 1.1 Structure of Thesis

This thesis is divided into six chapters. The remainder of this first chapter (from Section 1.4) introduces warm dense matter (WDM), discusses some techniques used to simulate WDM and their capabilities, and finally describes important structural properties of plasma generally calculable with such techniques. These structural properties, which are experimentally accessible, are calculated during the investigations of warm dense hydrogen in Chapter 4.

Chapter 2 introduces Smoothed Particle Hydrodynamics (SPH) and the Bohm potential in detail, the basic pillars of the model. SPH is used as the fundamental solver for the electron density, upon the gradients of which we can calculate the Bohm force. The Bohm potential, which in its most exact form introduces all quantum mechanical effects, is subsequently discussed and transformed into a simpler form as a function only of the global electron density.

Chapter 3 has three primary sections. The first details the remainder of the Bohm SPH code, including a novel SPH treatment for the Coulomb interaction and a Pauli repulsive potential to approximately capture symmetry effects. The second examines the implementation of the code and some algorithmic details. Here the conservation properties and parallel scaling of the code are demonstrated. The final section validates the general SPH structure, as well as the Bohmian and Coulombic parts of the code, by comparing Bohm SPH outputs to analytical solutions of the quantum harmonic oscillator and the ground state of hydrogen.

Chapter 4 investigates an example warm dense hydrogen system. Three iterations of Bohm SPH are tested and compared to reference calculations from wave packet molecular dynamics (WPMD). The outputs of the first, simple, iteration of Bohm SPH are included to demonstrate problematic thermal effects that arise when not controlling

for additional degrees of freedom in the model (additional compared to the physical situation). This subsequently motivates two further iterations, two-temperature and confinement Bohm SPH, which have improved agreement with WPMD, with the confinement approach yielding compelling electron dynamics. The effect of reducing the strength of the Bohm interaction is also explored.

Chapter 5 makes a first attempt at directly modelling electronic thermal relaxation in an x-ray free electron laser (XFEL) generated plasma, and compares to the elastic electronic collision operator of Fokker-Planck. While exploring the dependence of the thermalisation on the resolution (degrees of freedom) of Bohm SPH, a relation between the timescale of thermalisation and the average Coulomb coupling between SPH particles is noticed. This is leveraged for the direct Bohm SPH - Fokker-Planck comparison.

Finally, Chapter 6 outlines general conclusions regarding Bohm SPH and discusses a number of ideas for future work.

## 1.2 Author Contributions

This work has been conducted within a small group in the Atomic and Laser Physics Department at Oxford, supervised by Professors Gianluca Gregori and Sam Vinko. The project continues the research theme of applying Bohmian mechanics to simulations of warm dense matter, led in recent years by G. Gregori. Prior to this thesis, considerable work was done by Brett Larder, who helped introduce the author to the field. Significant computing resources were provided by STFC Scientific Computing Department's SCARF cluster. More specific contributions to the individual chapters are outlined below.

Chapter 1 is an introduction to warm dense matter and associated simulation techniques. Other than the application of the GCM fitting procedure to free electron dynamic structure factors for the first time, it contains no original work, nor does the theoretical overview of Smoothed Particle Hydrodynamics and the Bohm potential in

Chapter 2.

Chapter 3 details the novel Bohm SPH code. The idea of applying SPH to the problem was first suggested by G. Gregori. Development of the code was performed by the author, with help from Daniel Plummer during the early stages, and with various input from Pontus Svensson, S. Vinko and G. Gregori.

The Bohm SPH investigations of warm dense hydrogen in Chapter 4 were conducted by the author, with advice from G. Gregori and S. Vinko. In particular, P. Svensson provided the reference WPMD calculations alongside useful analysis code to help compute the structure outputs.

The Bohm SPH simulations of thermalisation in Chapter 5 were also conducted by the author, following close discussions with YuanFeng Shi and S. Vinko. Y. Shi conducted the reference CCFLY and Fokker-Planck calculations.

The author outlines several ideas for future work in the final chapter.

## 1.3 Author Publications

Below is the full list of publications on which I am a named author, based on work completed during my DPhil. A brief description of my contribution is attached to each.

1. **T. Campbell** *et al.*, "A molecular dynamics framework coupled with smoothed particle hydrodynamics for quantum plasma simulations", (accepted Physical Review Research) arXiv preprint arXiv:2408.03693, 2024
   *My overview paper on the Bohm SPH method, overlapping largely with the material in Chapters 3 and 4, as well as parts of Chapters 1 and 2.*

2. P. Svensson, **T. Campbell** *et al.*, "Development of a new quantum trajectory molecular dynamics framework", Philosophical Transactions of the Royal Society A, vol. 381, no. 2253, p. 20220325, 2023

*Collaborated on developing an anisotropic WPMD code with similar underlying molecular dynamic structure to Bohm SPH.*

3. T. Gawne, **T. Campbell** *et al.*, "Investigating mechanisms of state localization in highly ionized dense plasmas", Physical Review E, vol. 108, no. 3, p. 035210, 2023

   *Contributed spectral analysis code used to infer ionisation potential depression in experimental spectra. Various discussions with T. Gawne.*

4. K. Moczulski, H. Wen, **T. Campbell** *et al.*, "Numerical simulations of laser-driven experiments of ion acceleration in stochastic magnetic fields", Physics of Plasmas, vol. 31, no. 12, 2024

   *Co-PI and subsequent lead analyst of an experiment at GSI investigating second order Fermi acceleration via a laser-plasma laboratory analogue. Contributed experimental data to this accompanying simulation paper.*

5. D. Testa, [...], **T. Campbell** *et al.*, "Self-diffusion of a relativistic Lennard-Jones gas via semirelativistic molecular dynamics", Physical Review E, vol. 107, no. 5, p. 054138, 2023

   *Co-supervised masters student J. Jackson on molecular dynamic simulations of Lennard-Jones gas with modified (relativistic) equations of motion, project extended by following student D. Testa.*

6. A. Forte, [...], **T. Campbell** *et al.*, "Resonant inelastic x-ray scattering in warm-dense Fe compounds beyond the SASE FEL resolution limit", Communications Physics, vol. 7, no. 1, p. 266, 2024

   *Designed Von Hamos spectrometer, wrote associated spectral analysis code, and provided various diagnostic support in experiment at LCLS.*

7. J. Krása, [...], **T. Campbell** *et al.*, "Ion emission from warm dense matter pro-

duced by irradiation with a soft x-ray free-electron laser", Matter and Radiation at Extremes, vol. 9, no. 1, 2024

*Diagnostic and code support, primarily XANES, for experiment at FLASH2.*

8. C. Crepisson, [...], **T. Campbell** *et al.*, "Shock-driven amorphization and melt in $Fe_2O_3$", Physical Review B, vol. 111, no. 2, p. 024209, 2025

   *See 6.*

9. A. Forte, [...], **T. Campbell** *et al.*, "Methods for energy dispersive x-ray spectroscopy with photon-counting and deconvolution techniques", Journal of Applied Physics, vol. 137, iss. 13, 2025

   *Co-developed spectral analysis code for use in XFEL experiments.*

10. A. Amouretti, [...], **T. Campbell** *et al.*, "Phase transitions of $Fe_2O_3$ under laser shock compression", (in review) arXiv preprint arXiv:2402.18432, 2024

    *See 6.*

## 1.4 Warm Dense Matter

Warm dense matter (WDM) [1] is an exotic plasma state, generally defined by simultaneously having strongly coupled ions and quantum degenerate electrons. This is indicated by the ion coupling $\Gamma = \langle E_P \rangle / \langle E_K \rangle$ (with $E_P$ and $E_K$ the potential and kinetic energies respectively), and the electron degeneracy $\theta = k_B T / E_F$ (with $E_F$ the Fermi energy), both having values around 1. These conditions are typically found in plasmas around solid density and with a temperature of several eV. In this way WDM can be considered a transitional state between condensed matter, where we have solid density and low temperatures, and classical plasma which exists at low densities and high temperatures. A phase-space diagram showing the location of WDM is presented in Figure 1.1.

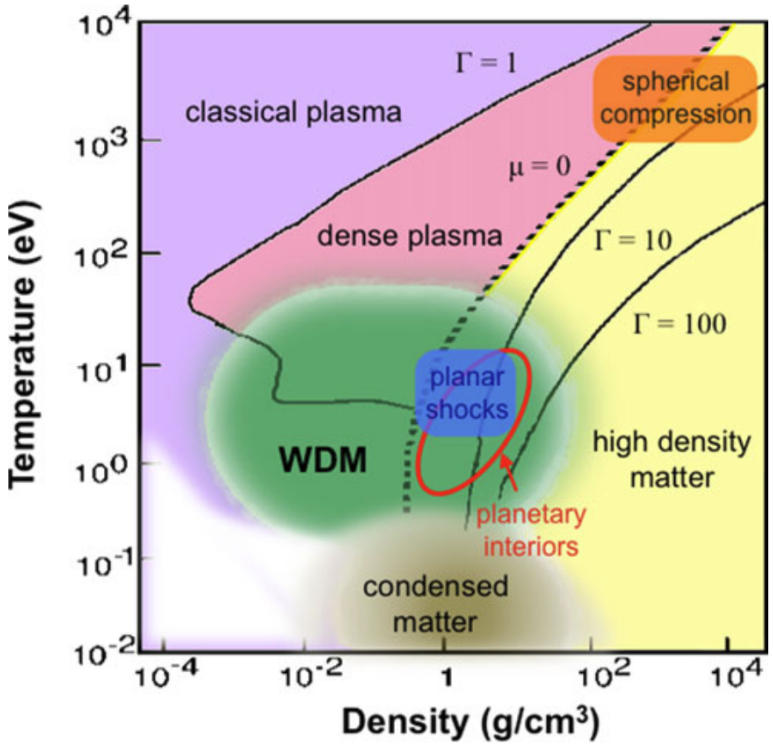


Figure 1.1: Reproduced from [2]. Temperature-density diagram showing the position of WDM in phase space, with $\Gamma$ the ionic coupling and $\mu$ the chemical potential, with $\mu = 0$ occuring when the thermal energy $k_B T$ equals the Fermi energy $\theta = 1$. Calculated for aluminium.

There has been growing interest in the laser-driven production, diagnosis, theoretical treatment, and simulation of WDM in the preceding decades. This has been driven by the advent of high power laser facilities and associated progress in inertial confinement fusion experiments (ICF) [3–5], and also by naturally occurring WDM in astrophysical objects such as the Jovian (and similar exoplanet) interior [6–8], dwarf stars, and neutron star crusts [9]. In ICF experiments, such as those conducted at the OMEGA [10] and NIF [11] laser facilities, the deuterium-tritium capsule passes through the WDM regime en route to ignition [12–14]; indeed, any laser-generated plasma which originates from an initially cool condensed matter sample will have traversed the WDM phase space.

Although transitional between condensed matter and a classical plasma, standard theoretical approaches from both fields, which typically rely on either the kinetic or the

potential energy being small (perturbative models), are inapplicable due to the moderate ionic coupling $\Gamma \approx 1$. This is not to mention the additional requirement of treating the electrons quantum mechanically; exactly solving the many-body Schrödinger equation for large systems is a frankly hopeless task.

To tackle the problem a range of ab-initio simulation techniques have been developed which resolve the system down to the particle (or indeed wavefunction) level, with some approximate form of quantum mechanical behaviour included. In this way, explicit simulation of the ions captures their strong coupling, mediated by screening from the degenerate electrons. A particular motivation is to determine the equation of state (EoS) and transport coefficients of WDM from dynamic microscopic simulations, which can then be used as inputs into larger scale, macroscopic plasma models, such as radiative-hydrodynamic codes (for example [15]). The transport coefficients in particular can be derived using Green-Kubo relations [16, 17]. Importantly, the EoS data and transport coefficients used in radiative-hydrodynamic codes affect their accuracy in modelling ICF implosions and in their determination of optimal target design.

To properly summarise all of the simulation methods applied to WDM problems is beyond the scope of this thesis. For this, the reader is directed to the recently submitted overview paper [18] and the references therein. Ref. [19] is also instructive for comparative estimations of transport coefficients. Here instead is a non-exhaustive list of computational WDM methods: effective ion-ion interaction Molecular Dynamics (MD) [20, 21], MD with classical electrons interacting via effective pairwise quantum statistical potentials (QSP) [22–24], MD with classical electrons interacting via an equilibrium Bohm potential (Bohm MD) [25], Wave Packet Molecular Dynamics (WPMD) [26–28], Quantum Hydrodynamics (QHD) [29, 30] which I will return to in the following chapter, Density Functional Theory coupled to MD (DFT-MD) [31, 32], average-atom models [33, 34], time-dependent Density Functional Theory (TDDFT) [35–37], and Quantum and Path Integral Monte Carlo approaches [38–41]. All of these approaches

have different levels of approximation, regimes of applicability, and computational cost.

A capability I will focus on is capturing dynamic electron behaviour. Dynamic electron behaviour is essential to estimation of system transport properties such as thermal and electrical conductivity. An important experimental WDM example of this is ion-electron thermal equilibration [42, 43], where either the ions (e.g. via shocks [44]) or electrons (e.g. via x-ray absorption [45]) are preferentially heated by the driver, and there are large uncertainties over the timescale of equilibration between the species. Furthermore, a widely used diagnostic technique in experimental WDM is x-ray Thomson scattering (XRTS) [46–48], where the scattering power is proportional to the electronic dynamic structure factor. Accurately simulating electron dynamics provides huge insight into these processes.

Moreover, explicit electron dynamics may be important to the accuracy of computed ion dynamics in WDM systems. This at odds with models that apply the Born-Oppenheimer approximation. This particularly applies to DFT-MD calculations, used widely to simulate dynamical ions in the WDM regime, which assume that at each timestep the electronic background instantaneously adjusts to the new ionic arrangement, meaning there is no energy exchange between the species. Indeed, deficiencies in this adiabatic approach were suggested by DFT-MD simulations of ion modes in a warm dense aluminium system in Ref. [49]. Here, to mimic the dissipative effect of the electrons, a Langevin noise model was included, the strength of which strongly affected the dispersion of the ion acoustic wave. To have confidence in predicted ion dynamics, seemingly we need to properly include dynamic interactions between electrons and ions. This was supported by further work [50] demonstrating significant differences between DFT-MD results for ion diffusion in warm dense hydrogen with results from the non-adiabatic electron force field (eFF) variant of WPMD (which resolves the electron dynamics) [51, 52]. Latterly this conclusion has been challenged in Ref. [53] performing a like-for-like comparison of adiabatic and non-adiabatic methodologies via eFF,

although uncertainty and limitations remain in the WPMD construction. Nonetheless, the first experimental measurements of ion modes in warm dense methane [54] highlight the need for accurate ab initio ion results to corroborate and inform future experiments.

Of the models listed above, only QSP, Bohm MD, WPMD, and TDDFT explicitly model the electron motion. QHD can also contribute dynamic electronic properties such as dispersion relations, however this is only on length scales significantly larger than the Thomas-Fermi screening length [55], precluding microscopic investigations.

QSP approaches are computationally the cheapest, with fixed pairwise potentials meaning the simulations are run with classical complexity. However, this modest computing cost is bought at the expense of relatively severe approximation, with the potentials valid only for weak electron coupling and only at fixed temperatures. At the other extreme, TDDFT has the most quantum mechanically complete description of the electron dynamics, but of course this incurs enormous cost, restricting analysis to short length and time scales (as in the full treatment of the dynamic structure factor in warm dense Beryllium [37]).

Between these limiting treatments sit WPMD and Bohm MD, with an improved description of quantum mechanical effects (relative to QSP) coming at moderate computational cost. With impressive weak parallel scaling, this enables investigation of long time and large length scales closer to the hydrodynamic limit. This is particularly pertinent to our stated goal of using ab initio methods to define the EoS and transport coefficients in macroscopic hydrodynamic codes.

WPMD derives equations of motion for the electrons via a variational principle with a restricted basis of Gaussians for the single particle wavefunctions [56]. Although the difference over short time scales ($\delta t$) between the true and the WPMD quantum dynamics is limited to $\mathcal{O}(\delta t^3)$ [57], the restricted basis is problematic. At low temperatures in particular, a single Gaussian does not ensure proper electron screening or resolve the essential atomic physics, nor indeed can it capture wavefunction break-up [19]. A recent

extension to WPMD has been to use anisotropic Gaussian wave packets [58], enlarging the manifold of accessible quantum states. Outputs from this improved WPMD model are compared against in Chapter 4.

Another recent approach to modelling WDM non-adiabatically has been to leverage Bohm's approach to quantum mechanics [59] (following similar work by de Broglie [60] and Madelung [61]). As I shall explore in the following chapter, the reformulation of the single-particle time-dependent Schrödinger equation yields a continuity and momentum evolution equation, with the latter equivalent to that of a classical system but with an additional potential term produced by the kinetic energy operator, the Bohm potential. The extension of this construction to many-body systems is straightforward, but calculation of the exact Bohm potential in this case is as complex as solving the exact many-body Schrödinger equation, hence some level of approximation is required. Work by Larder *et al* [25] applied a thermally averaged, linearized Bohm potential to capture the quantum kinetic energy of the electrons. This approach applies a two stage methodology where the Bohm potential is first calculated as a function of the equilibrium pair-correlation functions, determined with reference to an ion static structure calculation from an alternative scheme, such as DFT-MD. Once determined, the Bohm potential is then applied in an MD code, equivalent in computational cost to a pairwise classical system.

In this thesis a new Bohmian approach to the simulation of WDM is presented: Bohm Smoothed Particle Hydrodynamics (Bohm SPH). In a similar vein to Ref. [25], the platform is non-adiabatic and computationally tractable, able to evolve a warm dense matter system at electronic resolution for ionic timescales. Importantly however, this work moves beyond the two stage methodology and the Bohm force is not restricted to thermal equilibrium. This is accomplished by calculating a many-body Bohm pressure on-the-fly with an SPH solver. This is introduced in the next chapter, with the subtle difference between Bohm potential and pressure also outlined. A further feature

of the Bohm SPH construction is access to the continuous spatially resolved electron density. In the methodology multiple SPH particles are generally used to model individual electrons. This means that the overall electron shapes are not restricted to the shape of the SPH particles, but can be arbitrarily complex limited only by the number of particles used. Also worth stating is that while WDM investigation is the primary motivator for developing the model, its construction can be applied more broadly to quantum plasmas, defined simply by the electron degeneracy $\theta \lesssim 1$, and also to solving for single particle wavefunctions.

## 1.5 Characterising Structure

Computing the dynamic structure factor, $S(\mathbf{k}, \omega)$, is central to simulation of WDM. This section introduces the dynamic structure factor and its extraction prior to presenting data in Chapter 4, lengthier discussions are found in Ref.s [62, 63]. $S(\mathbf{k}, \omega)$ describes density fluctuations at wavenumber $\mathbf{k}$ and frequency $\omega$, defined as

$$S(\mathbf{k}, \omega) = \frac{1}{2\pi N} \int dt \, \exp(i\omega t) \langle \rho(\mathbf{k}, t) \rho(-\mathbf{k}, 0) \rangle, \tag{1.5.1}$$

where $N$ is the number of particles and $\rho(\mathbf{k}, t)$ is the spatial Fourier transform of the time-dependent density $n(\mathbf{r}, t)$, to which we have access in simulation. $S(\mathbf{k}, \omega)$ is an essential link between theory and experiment. It is related via the fluctuation-dissipation theorem to the density response function $\chi(k, \omega)$

$$S(k, \omega) = \frac{\hbar \, \mathrm{Im} \, \chi(k, \omega)}{\pi n (\exp(-\beta \hbar \omega) - 1)}, \tag{1.5.2}$$

and is directly proportional to the scattered x-ray power from a plasma [46, 64] at a

position $\mathbf{R}$ with solid angle $d\Omega$,

$$P_s(\mathbf{R},\omega)d\Omega d\omega \propto \frac{P_0}{A} S_{ee}(\mathbf{k},\omega)d\Omega d\omega, \tag{1.5.3}$$

where $P_0$ is the incident x-ray power, $A$ the plasma area irradiated by probe x-rays, and $S_{ee}(\mathbf{k},\omega)$ the dynamic electron structure factor. This relation is used in x-ray Thomson scattering, regularly deployed to diagnose the density and temperature of dense plasmas in the laboratory [47, 48].

The dynamic structure factor is the power spectrum of the intermediate scattering function (itself the Fourier transform of the van Hove function [65]),

$$F(\mathbf{k},t) = \frac{1}{N}\langle \rho(\mathbf{k},t)\rho(-\mathbf{k},0)\rangle, \tag{1.5.4}$$

furthermore, the frequency integrated version of the dynamic structure factor, $S(\mathbf{k}) = \int d\omega\, S(\mathbf{k},\omega)$, describes the static structure, and is related (via Fourier transform) to the pair correlation function.

When computing the dynamic structure factor from simulation data, one typically has to smooth out noise in the numerical intermediate scattering function [66]. A useful approach, particularly at large length scales, which can avoid ad-hoc smoothing approaches and moves beyond the discrete time sampling of $F(\mathbf{k},t)$ from the numerical data, is to apply the generalised collective modes (GCM) analysis for fitting the dynamic structure of pure liquids [67]. Lately this has also been applied in work on ionic modes in warm dense aluminium Ref. [68]. Following Ref. [67], a general expression for the (isotropic) intermediate scattering function, applying $N_r$ relaxing and $N_p$ propagating modes, can be written as

$$
\begin{aligned}
F(k,t) = &\sum_{i=1}^{N_\mathrm{r}} A_i(k) \exp\left[-\alpha_i(k)\cdot t\right] \\
&+ \sum_{j=1}^{N_\mathrm{p}} B_j(k) \exp\left[-\beta_j(k)\cdot t\right] \cos\left[\omega_j(k)\cdot t + \varphi_j(k)\right],
\end{aligned}
\tag{1.5.5}
$$

yielding an expression for the dynamic structure factor (dropping the $k$ dependence)

$$
\begin{aligned}
S(k,\omega) = &\sum_{i=1}^{N_\mathrm{r}} \frac{2A_i\alpha_i}{\alpha_i^2+\omega^2} \\
&+ \sum_{j=1}^{N_\mathrm{p}} B_j \left\{ \frac{\beta_j\cos\varphi_j - \left(\omega_j+\omega\right)\sin\varphi_j}{\beta_j^2+\left(\omega_j+\omega\right)^2} \right. \\
&\left. + \frac{\beta_j\cos\varphi_j - \left(\omega_j-\omega\right)\sin\varphi_j}{\beta_j^2+\left(\omega_j-\omega\right)^2} \right\}
\end{aligned}
\tag{1.5.6}
$$

In the case that $N_r = N_p = 1$, we simplify the fitting analysis by leveraging the sum rules of the dynamic structure factor. For classical fluids, the first three are

$$
\begin{aligned}
&\int_{-\infty}^{+\infty} S(k,\omega)\mathrm{d}\omega = S(k) = F(k,0) \\
&\int_{-\infty}^{+\infty} \omega S(k,\omega)\mathrm{d}\omega = -\left.\frac{\partial F(k,t)}{\partial t}\right|_{t=0} = 0 \\
&\int_{-\infty}^{+\infty} \omega^2 S(k,\omega)\mathrm{d}\omega = -\left.\frac{\partial^2 F(k,t)}{\partial t^2}\right|_{t=0} = k^2\frac{k_\mathrm{B}T}{m}.
\end{aligned}
\tag{1.5.7}
$$

Defining $B_1' = B_1\cos\phi_1$ and $B_1'' = B_1\sin\phi_1$, this produces the following relations

$$
\begin{aligned}
A_1 &= \frac{S\left(\beta_1^2+\omega_1^2\right)-C}{\left(\alpha_1-\beta_1\right)^2+\omega_1^2} \\
B_1' &= \frac{S\alpha_1\left(\alpha_1-2\beta_1\right)+C}{\left(\alpha_1-\beta_1\right)^2+\omega_1^2} \\
B_1'' &= \frac{S\alpha_1\left(\beta_1^2-\alpha_1\beta_1-\omega_1^2\right)+C\left(\alpha_1-\beta_1\right)}{\omega_1\left[\left(\alpha_1-\beta_1\right)^2+\omega_1^2\right]}.
\end{aligned}
\tag{1.5.8}
$$

where $S = S(k)$ and $C = k^2 k_B T/m$, reducing the number of independent parameters to three, $\alpha_1$, $\beta_1$, and $\omega_1$. This analysis is applied to generate all dynamic structure data presented in chapter 4, an example of which is given in Figure 1.2 for fitting the free electron intermediate scattering function.

A commonly used decomposition of the electron dynamic structure factor is given by Chihara [69, 70]

$$
\begin{aligned}
S_{ee}(\mathbf{k},\omega) = |f(\mathbf{k})+n(\mathbf{k})|^2 S_{ii}(\mathbf{k},\omega) + S_{ee}^0(\mathbf{k},\omega) \\
+S_{bf}(\mathbf{k},\omega)
\end{aligned}
\tag{1.5.9}
$$

where $f(\mathbf{k})$ is the unscreened bound electron form factor, $n(\mathbf{k})$ the screening cloud form factor, $S_{ii}(\mathbf{k},\omega)$ the ion - ion structure factor, $S_{ee}^0(\mathbf{k},\omega)$ the free electron structure factor, and $S_{bf}(\mathbf{k},\omega)$ a scattering contribution from bound-free transitions.

Bohm SPH explicitly models the electron dynamics. Hence, when applied to simulation of ionised hydrogen, with no contribution from $f(\mathbf{k})$ or $S_{bf}(\mathbf{k},\omega)$ I have access to both $S_{ii}(\mathbf{k},\omega)$ and $S_{ee}(\mathbf{k},\omega)$. Following the procedure outlined in Ref. [71], comparison of the intermediate scattering functions $F_{ee}(\mathbf{k},t)$ and $F_{ii}(\mathbf{k},t)$ enables calculation of the screening cloud form factor $n(\mathbf{k})$ and by extension, isolation of the free electron structure factor $S_{ee}^0(\mathbf{k},\omega)$ [71]. This allows direct calculation of plasmon behaviour. The screening cloud $n(\mathbf{k})$ can also be computed by comparing the proton-proton and

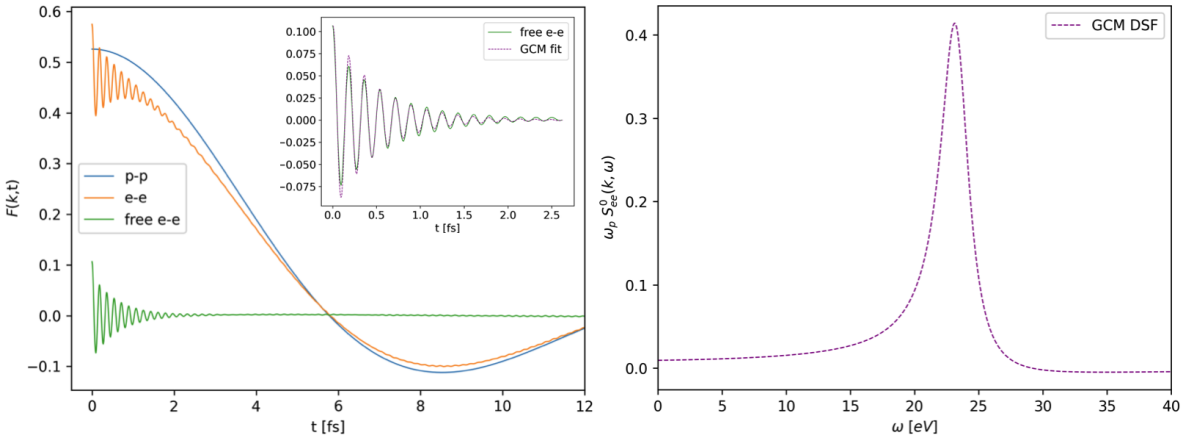


Figure 1.2: Example procedure for extracting the free electron dynamic structure factor, computed for $k = 0.278\, a_B^{-1}$ for strongest confinement run of warm dense hydrogen, details in Section 4.3. The free electron $F^0_{ee}(k,t)$ is isolated by fitting to Equation (1.5.10), after which it is fitted with one propragating and one relaxing mode in the GCM scheme (left inset), used to calculate $S^0_{ee}(k,\omega)$ (right).

proton-electron static structure factors [69] via $S_{pe}(\mathbf{k}) = n(\mathbf{k})S_{pp}(\mathbf{k})$ in the case of hydrogen. Here $n(k)$ (isotropic) is computed by minimising the integrated free electron intermediate scattering function

$$L = \int dt\, [F^0_{ee}(k,t)]^2 = \int dt\, \Big[F_{ee}(k,t) - (n(k))^2 F_{ii}(k,t)\Big]^2. \tag{1.5.10}$$

In addition, given the electrons behave quantum mechanically in WDM, a detailed balance correction is applied to free electron dynamic structure factor $S^0_{ee}(k,\omega)$, as in Ref. [64], of the form $\beta\hbar\omega/(1-e^{-\beta\hbar\omega})$. An example of extracting the free electron structure factor using this analysis and then applying the GCM fitting procedure is shown in Figure 1.2.

# Chapter 2

# Smoothed Particle Hydrodynamics and the Bohm Potential

This chapter provides an overview of Smoothed Particle Hydrodynamics (SPH) and the Bohm potential, two topics central to the construction of a novel code for computing quantum plasma dynamics, appropriately named Bohm SPH. Smoothed Particle Hydrodynamics (SPH) is used to describe the electron density distribution and enable computation of the Bohm pressure tensor. I will show how the SPH construction for evolving particles according to a pressure term can naturally be implemented into a molecular dynamics code.

Following a summary of the SPH methodology, the Bohm potential is introduced and derived. While the Bohm potential does not reduce the complexity of the Schrödinger equation in its exact form, its inclusion of all quantum effects (in principle) offers a conceptually attractive route to introducing quantum behaviour into simulations of quantum plasma. Subsequently, a quantum fluid model is derived with a computationally tractable form of the Bohm potential, with the related (but more general) Bohm pressure adopted for the investigations in the following chapters.

## 2.1 Smoothed Particle Hydrodynamics

Smoothed Particle Hydrodynamics is a meshless Lagrangian scheme for solving fluid equations, applied widely in fields ranging from astrophysics to the computer games industry [72–76]. First appearing in the late 1970s [77, 78], it obtains approximate numerical solutions of the equations of fluid dynamics by replacing the fluid with a set of particles, whose equations of motion are determined by interpolating from the continuum equations of fluid dynamics [77]. Smoothed Particle Hydrodynamics builds upon the definition of the dirac delta function, defined on a domain $\Omega$ such that for some continuous function $A(\mathbf{r})$

$$A(\mathbf{r}) = \int_{\Omega} d\mathbf{r}' A(\mathbf{r}')\delta(\mathbf{r} - \mathbf{r}'). \tag{2.1.1}$$

Then by approximating the delta function with a symmetric kernel function $W$, normalized to unity and with scale length $h$, we write

$$A(\mathbf{r}) \approx \int_{\Omega} d\mathbf{r}' A(\mathbf{r}')W(\mathbf{r} - \mathbf{r}', h). \tag{2.1.2}$$

This first step is known as the *kernel* approximation, and has order $h^2$ accuracy [79, 74]. $W$ is chosen so that it tends to a delta function in the limit $h \to 0$, and is discussed more thoroughly in Section 2.1.1. The second step of the method is the *particle* approximation, and involves dividing the fluid into small mass elements with mass $m_b$, density $\rho_b$ and position $\mathbf{r}_b$. Discretising the integral in Equation (2.1.2) into a summation gives

$$A(\mathbf{r}) = \sum_b m_b \frac{A_b}{\rho_b} W(\mathbf{r} - \mathbf{r}_b, h), \tag{2.1.3}$$

where $A_b$ is the value of the function $A$ at position $\mathbf{r}_b$. Gradients of the quantity $A(\mathbf{r})$

can then be calculated similarly,

$$\nabla A(\mathbf{r}) = \sum_b m_b \frac{A_b}{\rho_b} \nabla W(\mathbf{r} - \mathbf{r}_b, h). \tag{2.1.4}$$

Simple higher order derivatives are either then calculated with respect to Equation (2.1.4), such as

$$\nabla^2 A(\mathbf{r}) = \sum_b m_b \frac{\nabla A_b}{\rho_b} \nabla W(\mathbf{r} - \mathbf{r}_b, h), \tag{2.1.5}$$

or by further differentiation of the kernel function

$$\nabla^2 A(\mathbf{r}) = \sum_b m_b \frac{A_b}{\rho_b} \nabla^2 W(\mathbf{r} - \mathbf{r}_b, h). \tag{2.1.6}$$

It is worth noting that Equation (2.1.5) involves an additional summation to first compute $\nabla A_b$, prior to computing $\nabla^2 A(\mathbf{r})$.

### *2.1.1 Kernel Functions*

Various functions can be used as kernel functions, guided by considerations of accuracy, smoothness and computational cost [80, 72, 81, 74]. As mentioned previously, the function must be normalized to unity,

$$\int_\Omega d\mathbf{r}' W(\mathbf{r} - \mathbf{r}', h) = 1, \tag{2.1.7}$$

and should tend to a delta function as the scaling length decreases

$$\lim_{h\to 0} W(\mathbf{r}-\mathbf{r}',h) = \delta(\mathbf{r}-\mathbf{r}'). \tag{2.1.8}$$

This ensures the relative accuracy of the kernel approximation in Equation (2.1.2). Furthermore the kernel function should be smooth (indicated by the highest order of possible derivative), even, and monotonically decreasing as the distance $|\mathbf{r}-\mathbf{r}'|$ increases. For hydrodynamic simulations it is also necessary to have a positive kernel function at all points in the domain to ensure physically meaningful results. Finally, the smoothing function should be compactly supported such that it tends to zero at some reasonable factor $\sigma$ of the scaling length $h$

$$W(\mathbf{r}-\mathbf{r}',h) = 0, \;\; \text{for}\, |\mathbf{r}-\mathbf{r}'| > \sigma h. \tag{2.1.9}$$

Here $\sigma$ dictates the computational cost of the SPH interpolation. The SPH summation is restricted to the $N_{\text{neigh}}$ within the spherical region of radius $\sigma h$ around the target particle, hence a computational cost of order $\mathcal{O}(N_{\text{neigh}}N)$ for the full SPH estimate of a target property $A$ with $N$ SPH particles.

Gingold and Monaghan selected the Gaussian as a kernel function in their original paper [77], defining $R = |\mathbf{r}-\mathbf{r}'|/h$

$$W(R,h) = \frac{1}{\alpha_d}\exp\Big(-R^2\Big) \tag{2.1.10}$$

where $\alpha_d = (\pi h^2)^{d/2}$ with $d$ the number of dimensions. The Gaussian at first impression is an ideal candidate for the kernel function, satisfying all of the desirable properties apart from that of compact support. Indeed, as it never truly goes to zero, to have an

exact interpolation one must compute over all other particles in the system. In practice, the Gaussian does approach zero numerically quickly, so this constraint is not enforced, with a cutoff ($\sigma$) of 3 deemed tolerable in Ref. [80]. However, it does motivate using alternative kernels that behave like a Gaussian but approach zero faster. The most commonly used kernels [72] are based on Schoenberg $M_n$ splines [82], in particular the $M_4$ spline (known as the cubic spline as it is a piecewise cubic polynomial)

$$W(R,h) = \alpha_d \times \begin{cases} \frac{2}{3} - R^2 + \frac{1}{2}R^3 & 0 \leq R < 1 \\ \frac{1}{6}(2-R)^3 & 1 \leq R < 2 \\ 0 & R \geq 2, \end{cases} \tag{2.1.11}$$

where $\alpha_d = 1/h, 15/7\pi h^2$ and $3/2\pi h^3$ in 1, 2, and 3 dimensions respectively. Clearly, the cubic spline is much more compact than the Gaussian, with $\sigma = 2$, as indicated in Figure 2.1.

Most SPH models employ spherical kernels such as the Gaussian and $M_4$ spline above. These kernels are deficient however in cases where there are anisotropic deformations. This prompted the development of SPH with ellipsoidal kernels which have different smoothing lengths along each axis [83–86]. While not used in this work, such ellipsoidal kernels could improve the application of Bohm SPH to anisotropic problems, such as molecular binding. Indeed, the introduction of anisotropic wave packets into WPMD improved the accuracy of the binding energy calculation of the $H_2$ molecule [58].

A further consideration of SPH is the relative size of the scale length of the kernel $h$ to the average separation of SPH particles $\Delta$. A central result, provided by Ref. [87] and emphasised in Ref. [88], is that $n$th derivatives in SPH with an ordered particle distribution, have an error of order $h^2 + h^{-n}(\Delta/h)^2$. Hence it is not sufficient for $h \to 0$

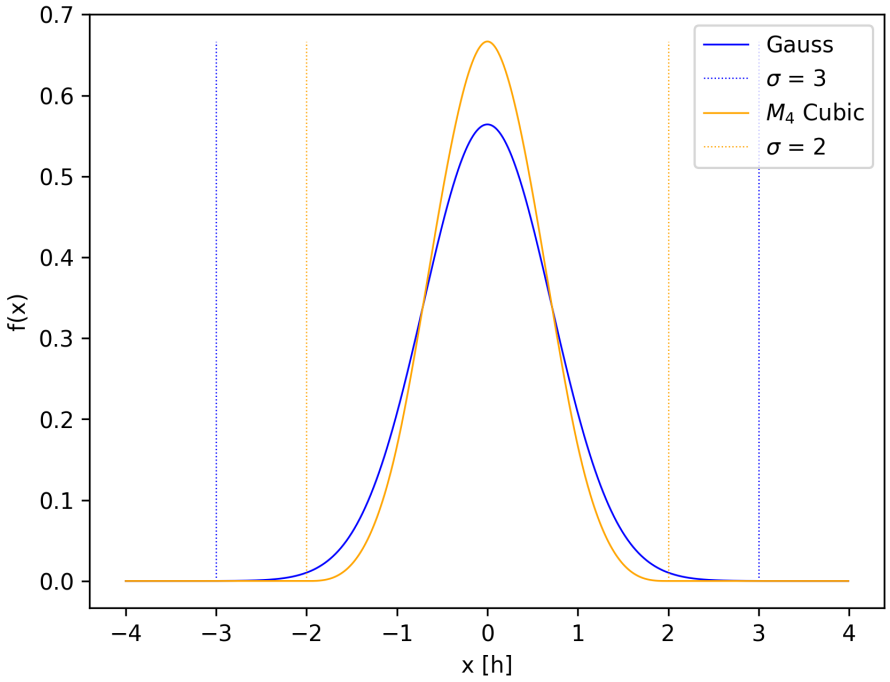


Figure 2.1: Comparison of the one dimensional Gaussian and $M_4$ cubic spline as kernel functions.

but also for $\Delta$ to decrease much faster than $h$. Here 'ordered' means SPH particles have a regular distribution in space. Work in Ref. [89] also showed that both $h \to 0$ and $\Delta/h^2 \to 0$ must be satisfied to achieve a convergent first derivative approximation. The exact requirements for convergence are complicated by having disordered particle arrangements, but these results nonetheless indicate the importance of having $h > \Delta$ for effective SPH interpolation.

Thus far, I have assumed that the scale length in the kernel function $h$ is a fixed, global, parameter. Indeed, in fluid problems with relatively homogeneous densities and regular particle arrangements this can be a satisfactory approach. However, for problems with strong density gradients, such as those I hope to tackle in quantum plasmas with electronic screening clouds around ions, this approach is restrictive, demanding we define a scaling length large enough to resolve the low density voids in the system. Instead it is preferable to resolve the dense and sparse regions of the system evenly, somewhat analogous to the automatic mesh refinement [90] of Eulerian mesh based

approaches to computational fluid dynamics. Although to be clear the particles do not subdivide in SPH, unlike the grid cells in automatic mesh refinement. Rather, the standard procedure for adaptive resolution is to relate the scale length of each particle $h_a$ to its local density $\rho_a$, resulting in the simultaneous equations

$$\rho_a = \sum_b m_b W(\mathbf{r}_a - \mathbf{r}_b, h_a) \tag{2.1.12}$$

$$h_a = \zeta \left( \frac{m_a}{\rho_a} \right)^{1/d}. \tag{2.1.13}$$

Here $d$ is the dimension of the system, and $\zeta$ is set to $> 1$ to ensure the $h > \Delta$ requirement discussed above. Typically, $\zeta$ is set to approximately 1.3 [72]. These relations ensure that the number of neighbours within the compact support radius of each SPH particle, or equivalently the mass inside the smoothing sphere [91], is roughly constant. They are solved via point iteration or via root finding methods such as Newton-Raphson. In this work point iteration is applied and its performance discussed in Section 3.2.1.

When defining density via Equation (2.1.12), we have two choices for the scale length in the summation, either $h_a$ as written, or $h_b$. These correspond to the so-called 'gather' and 'scatter' approaches of SPH respectively [92]. The gather approach is computationally more convenient, enabling $h_a$ to be defined, via Equations (2.1.12) and (2.1.13), as only a function of neighbour positions, and not also neighbour scaling lengths $h_{b \neq a}$. More significantly, this is essential to the derivation of conservative equations of motion for the SPH particles from a Lagrangian.

### *2.1.2 Derivative Forms*

It is well established in the SPH method that naïve derivatives of Equation (2.1.3), as in Equations (2.1.4) - (2.1.6), are not the most accurate [88, 93–95]. As will be outlined in

Section 2.2, derivatives of the electron density profile are required to compute the Bohm potential. Here I improve the accuracy of Equations (2.1.4) and (2.1.6) by introducing a basic difference term

$$\nabla A_a^{\text{diff}} = \sum_b \frac{m_b}{\rho_b} \left(A_b - A_a\right) \nabla W_{ab}(h_a) \tag{2.1.14}$$

$$\nabla^2 A_a^{\text{diff}} = \sum_b \frac{m_b}{\rho_b} \left(A_b - A_a\right) \nabla^2 W_{ab}(h_a), \tag{2.1.15}$$

where $W_{ab}$ is shorthand for $W(\mathbf{r}_a - \mathbf{r}_b, h)$. These derivative expressions, alongside more accurate forms, are discussed in greater detail in Ref. [88], whose analysis I briefly follow here. Improved accuracy of the difference expressions are demonstrated by employing the multi-dimensional Taylor expansion

$$A(\mathbf{r}_b) = \sum_{n=0}^{\infty} \frac{1}{n!} \Big[ \Big( (\mathbf{r}_b - \mathbf{r}_a) \cdot \nabla \Big)^n A(\mathbf{r}) \Big]_{\mathbf{r}=\mathbf{r}_a}. \tag{2.1.16}$$

Writing $\mathbf{r}_b - \mathbf{r}_a = \mathbf{r}_{ba}$, the first three terms are

$$A_b = A_a - \mathbf{r}_{ba} \cdot \nabla A|_a + \frac{1}{2} (\mathbf{r}_{ba} \cdot \nabla)(\mathbf{r}_{ba} \cdot \nabla) A|_a + \cdots . \tag{2.1.17}$$

Applying this expansion to the $A_b$ term in Equation (2.1.4) we extract, using $\langle \nabla A_a \rangle_S$ to denote the SPH interpolation

$$\begin{aligned}\langle \nabla A_a \rangle_S &= \sum_b \frac{m_b}{\rho_b} \Big( A_a - \mathbf{r}_{ba} \cdot \nabla A|_a + \cdots \Big) \nabla W_{ba} \\ &= A_a \sum_b \frac{m_b}{\rho_b} \nabla W_{ba} - \nabla A|_a \cdot \sum_b \frac{m_b}{\rho_b} \mathbf{r}_{ba} \nabla W_{ba} + \cdots .\end{aligned} \tag{2.1.18}$$

The truncation error in the interpolated value compared to the real is then

$$\begin{aligned}Er_a &= \langle \nabla A_a \rangle_S - \nabla A|_a \\ &= A_a \sum_b \frac{m_b}{\rho_b} \nabla W_{ba} - \nabla A|_a \cdot \left( \mathbf{I} + \sum_b \frac{m_b}{\rho_b} \mathbf{r}_{ba} \nabla W_{ba} \right) + \cdots ,\end{aligned} \tag{2.1.19}$$

where $\mathbf{I}$ is the identity matrix. The presence of $A_a$ in the error expression is problematic, as while $\sum_b \frac{m_b}{\rho_b} \nabla W_{ba}$ vanishes when the SPH particles have a regular arrangement, in general it is non-zero [88] . If a constant $A_0$ is added uniformly to the system, the truncation error in $\langle \nabla A_a \rangle_S$ grows proportionally.

If I also Taylor expand $A_b$ in the difference form of first derivative (Equation (2.1.14)), the $A_a$ term cancels

$$\begin{aligned}\langle \nabla A_a^{\text{diff}} \rangle_S &= \sum_b \frac{m_b}{\rho_b} \left( A_a - \mathbf{r}_{ba} \cdot \nabla A|_a + \cdots - A_a \right) \nabla W_{ab}(h_a) \\ &= \sum_b \frac{m_b}{\rho_b} \left( -\mathbf{r}_{ba} \cdot \nabla A|_a + \cdots \right) \nabla W_{ab}(h_a).\end{aligned} \tag{2.1.20}$$

Then the leading term in the truncation error of $\langle \nabla A_a^{\text{diff}} \rangle_S$ is proportional to $\nabla A|_a$,

$$\begin{aligned}Er_{a_{\text{diff}}} &= \langle \nabla A_a^{\text{diff}} \rangle_S - \nabla A|_a \\ &= -\nabla A|_a \cdot \left( \mathbf{I} + \sum_b \frac{m_b}{\rho_b} \mathbf{r}_{ba} \nabla W_{ba} \right) + \cdots ,\end{aligned} \tag{2.1.21}$$

this is an order of magnitude more accurate than the truncation error of $\langle \nabla A_a \rangle_S$, and is equivalent to zeroth-order consistency.

The same analysis can be applied to comparing the errors for second derivatives, with the difference term in Equation (2.1.15) making its truncation error proportional to $\nabla A|_a$, an order of magnitude improvement over Equation (2.1.6) whose truncation error is proportional to $A|_a$. Using a second derivative in Equation (2.1.5), where $\nabla A_a^{\text{diff}}$ is used for the first derivative (Equation (2.1.14)), also has a truncation error proportional to $\nabla A|_a$, however requires an additional summation to compute. It is worth reiterating that more accurate SPH derivative forms exist [88, 94], however these require at least one additional summation over particle neighbours to compute. The difference terms outlined above and adopted here are fast to compute, with only a single summation term needed. The energy conservation of several derivative forms on a simple Bohmian system are checked in Section 3.2.3, where in fact the derivatives with difference terms perform best.

### *2.1.3 SPH Equations of Motion*

In the nascence of SPH, the approach to deriving equations of motion was to heuristically adapt the continuum equations of motion into discretized SPH form. Such an approach does not guarantee the conservation of momentum and energy in the system. Since the turn of the millennium, a variational approach starting from a discretized Lagrangian has become established [91, 96, 72, 75, 97], with the symmetries of the starting Lagrangian guaranteeing certain conservation laws. I now derive the equations of motion for SPH particles with such a variational approach. Beginning with the continuum Lagrangian,

$$\mathfrak{L} = \int d\mathbf{r} \left[ \frac{\rho \mathbf{v}^2}{2} - \rho u(\rho, s) \right], \tag{2.1.22}$$

where $u$ is an internal energy per unit mass and $\mathbf{v}$ is the velocity. We discretise Equation (2.1.22) into an SPH form

$$\mathfrak{L} = \sum_b \frac{m_b}{\rho_b}\left[\frac{\rho_b \mathbf{v}_b^2}{2} - \rho_b u_b(\rho_b, s_b)\right] \tag{2.1.23}$$

$$= \sum_b m_b\Big[\frac{\mathbf{v}_b^2}{2} - u_b(\rho_b, s_b)\Big]. \tag{2.1.24}$$

Assuming this Lagrangian is differentiable, the Euler-Lagrange equations follow

$$\frac{d}{dt}\Big(\frac{\partial \mathfrak{L}}{\partial \mathbf{v}_a}\Big) - \frac{\partial \mathfrak{L}}{\partial \mathbf{r}_a} = 0. \tag{2.1.25}$$

Now to compute a derivative of the Lagrangian with respect to position $\partial\mathfrak{L}/\partial\mathbf{r}_a$, consider the first law of thermodynamics (applicable for macroscopic fluid systems)

$$dU = TdS - PdV, \tag{2.1.26}$$

with $T$ the temperature, $S$ the entropy, $P$ the pressure and $V$ the volume. Noting that the change in volume can be given by $dV = -m/\rho^2 d\rho$, and using per mass quantities

$$du = Tds + \frac{P}{\rho^2}d\rho, \tag{2.1.27}$$

leading to, at constant entropy, an equation for the momentum evolution

$$m_a\frac{dv_a}{dt} = \frac{\partial \mathfrak{L}}{\partial \mathbf{r}_a} = -\sum_b m_b \left.\frac{\partial u_b}{\partial \rho_b}\right|_s \frac{\partial \rho_b}{\partial \mathbf{r}_a} = -\sum_b m_b \frac{P_b}{\rho_b^2}\frac{\partial \rho_b}{\partial \mathbf{r}_a}. \tag{2.1.28}$$

The assumption of constant entropy restricts these equations of motion to inviscid, dissipationless systems, therefore preventing the treatment of shocks. This is overcome by subsequent addition of artificial viscosity to the system [75].

Now the definition of density and kernel scale lengths in Equations (2.1.12) and (2.1.13) become relevant when computing the spatial derivative of the density

$$\frac{\partial \rho_b}{\partial \mathbf{r}_a} = \nabla_a \rho_b + \frac{\partial \rho_b}{\partial h_b}\frac{\partial h_b}{\partial \mathbf{r}_a}, \tag{2.1.29}$$

where in this notation $\nabla_a$ means $\partial/\partial \mathbf{r}_a$ but keeping scaling lengths constant. Equation (2.1.13) means $\rho_a h_a^3 =$ constant, such that

$$\begin{aligned} \frac{\partial}{\partial \mathbf{r}_a}(\rho_b h_b^3) &= \frac{\partial \rho_b}{\partial \mathbf{r}_a} h_b^3 + \rho_b 3 h_b^2 \frac{\partial h_b}{\partial \mathbf{r}_a} = 0 \\ \therefore \frac{\partial h_b}{\partial \mathbf{r}_a} &= -\frac{h_b}{3\rho_b}\frac{\partial \rho_b}{\partial \mathbf{r}_a}. \end{aligned} \tag{2.1.30}$$

Combining Equations (2.1.29) and (2.1.30), we have

$$\begin{aligned} \frac{\partial \rho_b}{\partial \mathbf{r}_a} &= \nabla_a \rho_b + \frac{\partial \rho_b}{\partial h_b}\Big( -\frac{h_b}{3\rho_b}\frac{\partial \rho_b}{\partial \mathbf{r}_a}\Big) \\ \frac{\partial \rho_b}{\partial \mathbf{r}_a} &= \frac{1}{\Omega_b}\nabla_a \rho_b, \end{aligned} \tag{2.1.31}$$

where the $\Omega$ term is defined

$$\Omega_b \equiv 1 + \frac{h_b}{3\rho_b}\frac{\partial \rho_b}{\partial h_b}. \tag{2.1.32}$$

To arrive at the final expression for the momentum equation, consider the exact form of $\nabla_a \rho_b$

$$\nabla_a \rho_b = \nabla_a \sum_c m_c W(\mathbf{r}_b - \mathbf{r}_c, h_b). \tag{2.1.33}$$

Recall that the kernel function is symmetric, such that $W(\mathbf{r}_b - \mathbf{r}_c, h_b) = W(|\mathbf{r}_b - \mathbf{r}_c|, h_b)$. Therefore we need to compute the component-wise derivative of the separation $|\mathbf{r}_b - \mathbf{r}_c|$ (following the treatment in Ref. [73])

$$\nabla_a |\mathbf{r}_b - \mathbf{r}_c| = \frac{(\mathbf{r}_b - \mathbf{r}_c)(\delta_{ba} - \delta_{ca})}{|\mathbf{r}_b - \mathbf{r}_c|} = \hat{e}_{bc}(\delta_{ba} - \delta_{ca}), \tag{2.1.34}$$

where $\delta_{ba}$ is the Kronecker delta. Then denoting $|\mathbf{r}_b - \mathbf{r}_c| = r_{bc}$ and $W_{bc} = W(|\mathbf{r}_b - \mathbf{r}_c|)$, the derivative of the kernel function with respect to an arbitrary coordinate $a$ while keeping the smoothing lengths constant, is

$$\begin{aligned} \nabla_a W_{bc} &= \left.\frac{\partial W_{bc}}{\partial \mathbf{r}_a}\right|_{\{h_b\}} = \left.\frac{\partial W_{bc}}{\partial r_{bc}}\right|_{\{h_b\}} \frac{\partial r_{bc}}{\partial \mathbf{r}_a} = \left.\frac{\partial W_{bc}}{\partial r_{bc}}\right|_{\{h_b\}} \hat{e}_{bc}(\delta_{ba} - \delta_{ca}) \\ &= \nabla_b W_{bc}(\delta_{ba} - \delta_{ca}), \end{aligned} \tag{2.1.35}$$

where $\{h_b\}$ indicates the set of scaling lengths. An extension of this result is that $\nabla_a W_{ab} = -\nabla_b W_{ab}$. Finally, insert these relations into Equation (2.1.28), yielding

$$\begin{aligned} m_a \frac{dv_a}{dt} &= -\sum_b m_b \frac{P_b}{\Omega_b \rho_b^2} \sum_c m_c \nabla_b W_{bc}(h_b)(\delta_{ba} - \delta_{ca}) \\ &= -m_a \frac{P_a}{\Omega_a \rho_a^2} \sum_c m_c \nabla_a W_{ac}(h_a) + \sum_b m_b \frac{P_b}{\Omega_b \rho_b^2} m_a \nabla_b W_{ba}(h_b) \\ &= -m_a \frac{P_a}{\Omega_a \rho_a^2} \sum_b m_b \nabla_a W_{ab}(h_a) - m_a \sum_b m_b \frac{P_b}{\Omega_b \rho_b^2} \nabla_a W_{ba}(h_b) \\ \therefore \frac{dv_a}{dt} &= -\sum_b m_b \Big[ \frac{P_a}{\Omega_a \rho_a^2} \nabla_a W_{ab}(h_a) + \frac{P_b}{\Omega_b \rho_b^2} \nabla_a W_{ab}(h_b) \Big]. \end{aligned} \tag{2.1.36}$$

This is a central equation of SPH. The symmetries of the initial Lagrangian, with no dependence on time, as well as translational and rotational invariance, ensure the

conservation of energy, linear and angular momentum respectively. Although the introduction of non-spherical kernels, discussed previously, introduces a rotational dependence and prevents conservation of angular momentum. The internal energy per particle evolves according to [97]

$$\frac{du_a}{dt} = \frac{P_a}{\Omega_a \rho_a^2} \sum_b m_b \left(\mathbf{v}_a - \mathbf{v}_b\right) \cdot \nabla_a W_{ab}(h_a), \tag{2.1.37}$$

All that remains is to define a suitable form for the pressure in the momentum equation. For an ideal gas for example, this takes the form $P \propto \rho^\gamma$, where $\gamma$ is the adiabatic index.

For my goal of modelling microscopic quantum plasmas, an approximation is required since I have shown how the standard SPH equation of motion Equation (2.1.36) emerges after using a thermodynamic relation in Equation (2.1.26). This central approximation of the Bohm SPH model is that there exists a *quantum* pressure $P \equiv P_B$ able to describe the motion of an ensemble of particles such that the quantum properties emerge in a statistical sense. I refer to $P_B$ as the quantum Bohm pressure. While conceptually very different from the conventional thermodynamic pressure, in all that follows I take that $P_B$ behaves in the same way as ordinary pressure such that Equation (2.1.36) is applicable. This can be justified rigorously starting from the Wigner distribution of the quantum statistical ensemble of particles, and, by taking moments of the Wigner-Boltzmann equation, deriving the corresponding hydrodynamic equations in which $P_B$ emerges, as shown in Ref.s [98, 99]. I follow a similar approach in Section 2.2.2, although I simplify the discussion to one-dimension where a scalar potential, $V_B$, rather than pressure tensor $P_B$, appears. As discussed in Ref.s [98, 100], if $P_B$ is restricted to a diagonal (isotropic) form, it is directly related to $V_B$ via

$$\nabla \cdot P_B = n \nabla V_B. \tag{2.1.38}$$

The exact forms of $V_B$ and $P_B$ are introduced in the following section.

Previous work in Ref. [101] has used the SPH construction to evolve the wave-function density according to the Bohm pressure tensor $P_B$, with the $P \equiv P_B$ approximation validated on a one-dimensional quantum harmonic oscillator, the non-linear Schrödinger equation in two-dimensions, and the Gross-Pitaevskii-Poisson equation in three-dimensions. As shown subsequently, the Bohm pressure tensor is a function of the density $\rho$ and its first and second order gradients. The density and its gradients are computed for SPH particles in the structure outlined above, purely as functions of their neighbour positions. This makes the SPH scheme suitable for solving in a molecular dynamics code.

## 2.2 Bohm Potential

In general, the discussion here focuses on the more familiar Bohm potential rather than pressure, although the concepts are the same. Furthermore, the aim of this thesis is not to make weighty contributions to the interpretation of quantum mechanics but rather to leverage the Bohm potential (or similarly, pressure) to simplify simulations of quantum plasmas. However, a brief discussion of the Bohmian approach is included here for historical colour. In 1952 David Bohm published two papers on 'A suggested interpretation of the Quantum Theory in Terms of "Hidden" Variables' [59, 102]. The overall argument of this work is that the orthodox interpretation of quantum mechanics as inherently probabilistic and indeterminate, is deficient, and that 'there must exist precisely definable elements or dynamical variables determining the actual behaviour of each individual system, and not merely its probable behaviour'; the "hidden" variables. This followed similar objections by Einstein [103] to the probabilistic interpretation

championed by Bohr [104] and others, later coined the Copenhagen interpretation. The 'quantum potential' derived by Bohm, which I will use interchangeably with 'Bohm potential', was previously derived by Madelung in fluid equations for the wavefunction [61], and by de Broglie [60] in his pilot-wave formulation. Given the obvious connection between de Broglie's work and Bohm's, evidenced by Equation (2.2.7), the approach outlined here is often referred to as the 'de Broglie-Bohm interpretation of quantum mechanics'.

Bohm compared quantum mechanics to the probabilistic predictions of classical statistical mechanics, which are underpinned by fully deterministic laws governing the individual members of the statistical ensemble. Indeed 'from the point of view of macroscopic [statistical] physics, the coordinates and momenta of individual atoms are hidden variables, which in a large scale system manifest themselves only as statistical averages' [59]. The Born rule of quantum mechanics, that configurations are distributed in space according to the probability $\rho = |\psi|^2$, then has a similar status to that of thermal equilibrium in statistical mechanics. Shortly after the 1952 papers Bohm submitted proofs [105, 106] that the density would naturally relax to an equilibrium state $\rho \to |\psi|^2$ in his causal interpretation. This has been followed by modern investigations [107, 108] with comparison of the process to Boltzmann's H theorem, as well as conjectures of astrophysical signatures of 'non-equilibrium' $\rho \neq |\psi|^2$ distributions [109]. The detection of non-equilibrium distributions would undermine the Copenhagen interpretation as being the most complete possible specification of the system.

To the author's knowledge such exact theories of motion on the quantum scale have not been determined and there have been no definitive contradictions of the Born rule. Hence the orthodox interpretation of quantum mechanics has not been superseded. However, Bohm's formalism leads to a computationally convenient structure for capturing quantum behaviour in many-body simulations of plasma at the relevant conditions, as I exploit in this thesis.

Connected with Bohm's work, particularly regarding the idea that the Born rule captures a statistical equilibrium of a quantum system, emerged the phase space approach to quantum mechanics, starting with Wigner's pseudo-probability function [110], and extended by Moyal [111] and Takabayasi [112] (see also Tatarskii [113]). This phase space approach enables construction of a quantum fluid model, with certain approximations, that yields a computationally convenient form of the many-body Bohm potential reduced to a function of only the global density, the quantum hydrodynamic (QHD) Bohm potential. QHD models have become popular when modelling metallic nano-objects in recent decades, where the reduction of the full phase space to a small number of equations in ordinary space enables a massive computational saving [114, 100]. In brief, the construction has close analogy with that of classical statistical mechanics for a weakly coupled electrostatic $N$ body system. Here, the $N$-particle Liouville equation is reduced to the single particle Vlasov equation via closure of a Bogolyubov-Born-Green-Kirkwood-Yvon (BBGKY) hierarchy; similarly a weakly coupled quantum $N$-particle system is reduced to a single particle Wigner-Poisson equation. Then, by taking velocity moments of the Wigner-Poisson equation and with appropriate closure, the fluid model emerges. This procedure is outlined in Section 2.2.2 with its deficiencies discussed, and the more accurate (and more computationally intensive) microscopic QHD equations introduced at the end of the section.

I will ultimately adopt the QHD-level Bohm pressure tensor (related in the diagonal case to the potential via Equation (2.1.38)), however it must be emphasised that the macroscopic equations of quantum hydrodynamics are not implemented in general (although this is viable with the SPH scheme). Instead, I will use the QHD Bohm pressure in microscopic equations of motion for the SPH particles, similar to the microscopic QHD (equivalent to TDDFT [115]) equations, where an individual SPH particle has at most the mass of a single electron, but in general will be a fraction of an electron as outlined in the next chapter. If an SPH particle has a mass and charge (significantly)

greater than that of a single electron, the full quantum hydrodynamic treatment is more appropriate.

The reader is directed to Robert Wyatt's comprehensive text on quantum trajectories [116], which includes greater discussion of the de Broglie-Bohm approach and quantum hydrodynamics.

### *2.2.1 Schrödinger Equation*

The Bohm potential [59] can be derived by using a polar (Madelung [61]) form of the wavefunction for a pure state, here demonstrated for a spinless non-relativistic single particle

$$\psi(\mathbf{r},t) = R(\mathbf{r},t)\,\exp\Big[\frac{iS(\mathbf{r},t)}{\hbar}\Big], \tag{2.2.1}$$

where $R$ and $S$ are real, and $\mathbf{r}$ is the position vector. The time dependent Schrödinger equation, for a particle of mass $m$ under a potential $V(\mathbf{r})$ and with $\hbar$ the reduced Planck's constant,

$$i\hbar\frac{\partial\psi}{\partial t} = -\frac{\hbar^2}{2m}\nabla^2\psi + V\psi, \tag{2.2.2}$$

yields with this polar form of $\psi$, by solving the real and imaginary parts of the Schrödinger equation, equations for $R$ and $S$

$$\frac{\partial R}{\partial t} = -\frac{1}{2m}[R\nabla^2 S + 2\nabla R\cdot\nabla S] \tag{2.2.3}$$

$$\frac{\partial S}{\partial t} = -\Big[\frac{(\nabla S)^2}{2m} + V - \frac{\hbar^2}{2m}\frac{\nabla^2 R}{R}\Big]. \tag{2.2.4}$$

Note that $R = n^{\frac{1}{2}}$ where here $n(\mathbf{r}, t)$ is the probability density of the single particle in phase space. Thus we write Equation (2.2.3) as

$$\frac{\partial n}{\partial t} + \nabla \cdot \left( n \frac{\nabla S}{m} \right) = 0, \tag{2.2.5}$$

which is a probability conservation equation where, if we associate $S$ with the classical action, $\frac{\nabla S}{m}$ gives the velocity. More importantly however, we recognise that (2.2.4) is the classical Hamilton Jacobi equation with an additional quantum potential, the Bohm potential

$$V_B(\mathbf{r}, t) = -\frac{\hbar^2}{2m} \frac{\nabla^2 R(\mathbf{r}, t)}{R(\mathbf{r}, t)}. \tag{2.2.6}$$

Takabayasi gave a succinct summary of the Hamilton-Jacobi like expression as the 'configuration space ensemble' (distinct to the phase space ensemble introduced in Section 2.2.2), stating that 'according to this expression we have the representation of quantum mechanical motion in terms of an ensemble of trajectories in configuration space subject to some additional force [Bohm potential], or equivalently in terms of an irrotational flow of perfect fluid with peculiar internal stress' [112]. As demonstrated later, this peculiar internal stress can be defined as the pressure tensor equivalent of the Bohm Potential.

Given that the Hamilton-Jacobi equation is equivalent to solving Newton's laws of motion with the correct boundary conditions, the equation of motion of the target particle is then expressed as

$$m \frac{d^2 \mathbf{r}}{dt^2} = -\nabla \Big[ V(\mathbf{r}) + V_B(\mathbf{r}) \Big]. \tag{2.2.7}$$

In this way Bohm considered the wavefunction to be the representation of an additional

field from which the particle samples the quantum force, the $\psi$ field, whose absolute value defines the Bohm potential and which obeys the Schrödinger equation in the same way as the electromagnetic field obeys Maxwell's laws. Similarly, de Broglie interpreted the wavefunction $\psi$ which determines $V_B$ as a pilot wave determining the particle's motion. The Bohm potential introduces all quantum effects, including non-locality.

The many-body form of the Bohm potential is similarly derived [59]. Starting with the full many-body wavefunction in polar form

$$\Psi = A(\mathbf{x}_1, \mathbf{x}_2, \ldots, \mathbf{x}_N) \exp\left[\frac{i\mathcal{S}(\mathbf{x}_1, \mathbf{x}_2, \ldots, \mathbf{x}_N)}{\hbar}\right], \tag{2.2.8}$$

and with the velocity of the $i$th particle also given by $\mathbf{v}_i = \nabla_i \mathcal{S}(\mathbf{x}_1, \mathbf{x}_2, \ldots, \mathbf{x}_N)/m$ where $\nabla_i$ refers to a derivative with respect to the $i$th coordinates and where I have assumed the particles have equal mass, we arrive at the many-body Bohm potential

$$V_B^N(\mathbf{x}_1, \mathbf{x}_2, \ldots, \mathbf{x}_N) = -\frac{\hbar^2}{2mA(\mathbf{x}_1, \mathbf{x}_2, \ldots, \mathbf{x}_N)} \sum_{i=1}^{N} \nabla_i^2 A(\mathbf{x}_1, \mathbf{x}_2, \ldots, \mathbf{x}_N). \tag{2.2.9}$$

Once again this expression encodes all the quantum behaviour of the system, which is now many-body. In this way, provided $\Psi$ is appropriately antisymmetrised for a fermionic system, this Bohm potential enforces the exclusion principle, preventing two particles from occupying the same state.

While conceptually neat, in the absence of an exact description of quantum behaviour in terms of "hidden variables" Bohm's reformulation of the Schrödinger equation does not actually simplify my ultimate task of simulating quantum plasmas. The exact many-body Bohm potential requires knowledge of the appropriate wavefunction which is clearly unfeasible, so I require some level of approximation.

### 2.2.2 Quantum Hydrodynamics

The Quantum Hydrodynamic equations are derived from the phase space approach. In this section I follow in particular the references [117, 118, 55], and Fernando Haas' textbook [119] which includes a complete discussion of these approaches.

For a single particle pure state quantum system, the Wigner function is defined, in one dimension for simplicity, as [110]

$$f(x,\nu,t) = \frac{m}{2\pi\hbar}\int ds \exp\left(\frac{im\nu s}{\hbar}\right)\psi^*\left(x+\frac{s}{2},t\right)\psi\left(x-\frac{s}{2},t\right), \tag{2.2.10}$$

with $x$ the position and $\nu$ the velocity. The phase space treatment can also readily describe a mixed state, defined by the set of $M$ single particle wavefunctions $\{\psi_a, p_a\}$, where each wavefunction $\psi_a$ occurs with probability $p_a > 0$ and sums to 1 $\sum_{a=1}^{M} p_a = 1$. Then the Wigner function can be written

$$f(x,\nu,t) = \frac{m}{2\pi\hbar}\sum_{a=1}^{M} p_a \int ds \exp\left(\frac{im\nu s}{\hbar}\right)\psi_a^*\left(x+\frac{s}{2},t\right)\psi_a\left(x-\frac{s}{2},t\right). \tag{2.2.11}$$

The Wigner function is not a true probability distribution since it can take negative values (nor is it unique [119]), however it reproduces both the correct quantum mechanical marginal distributions such as the spatial density

$$n(x,t) = \int_{-\infty}^{+\infty} f(x,\nu,t)dv = \sum_{a=1}^{N} p_a \left|\psi_a\right|^2, \tag{2.2.12}$$

and, as in classical statistical mechanics, is used to compute the expectation value of a given quantity $B(x,\nu)$

$$\langle B\rangle = \frac{\int f(x,\nu,t)B(x,\nu,t)dxd\nu}{\int f(x,\nu,t)dxd\nu}. \tag{2.2.13}$$

For a quantum many-body system with equal masses, the mixed state Wigner func-

tion is

$$
\begin{aligned}
f^N\left(x_1,\nu_1,\ldots,x_N,\nu_N,t\right) =& N\left(\frac{m}{2\pi\hbar}\right)^N \sum_{a=1}^{M} p_a \int ds_1,\ldots,ds_N \exp\left(\frac{im\sum_{i=1}^{N}\nu_i s_i}{\hbar}\right) \\
&\times \Psi_a^*\left(x_1+\frac{s_1}{2},\ldots,x_N+\frac{s_N}{2},t\right) \\
&\times \Psi_a\left(x_1-\frac{s_1}{2},\ldots,x_N-\frac{s_N}{2},t\right),
\end{aligned}
\tag{2.2.14}
$$

whose evolution is governed by the quantum Liouville equation (Wigner transform of the von Neumann equation for density matrices), and where fermionic statistics are enforced by having antisymmetrised forms for the wavefunctions $\Psi_a$. This is a complete description of the quantum many-body system and therefore unwieldy for analytic or numerical techniques. Instead, it is preferable to handle the reduced one-particle Wigner function, where the variables for particles $2,3\ldots N$ have been integrated out

$$
f(x_1,\nu_1,t) = \int dx_2 d\nu_2 \ldots dx_N d\nu_N f^N\left(x_1,v_1,\ldots,x_N,v_N,t\right). \tag{2.2.15}
$$

In deriving the equation of motion for the reduced one-particle Wigner function we are presented with the quantum equivalent of the BBGKY hierarchy. To close the hierarchy I assume the particles are weakly coupled ($\Gamma_q < 1$), or at least that the collisional timescale of the electrons is much slower than the collisionless, which is true for certain metallic systems via Pauli blocking [117–119] despite having large electronic couplings. This ignores correlations, as in the molecular chaos hypothesis. This mean field (Hartree) approximation ensures the many-body Wigner function factorises such that

$$
f^{(2)}\left(x_1,v_1,x_2,v_2,t\right) = f\left(x_1,v_1,t\right) f\left(x_2,v_2,t\right), \tag{2.2.16}
$$

although this simple factorisation also neglects antisymmetrisation so Pauli repulsion

is not captured. Exchange and correlation effects can be introduced in a phenomenological manner using the local density approximation, similar to the approach of DFT, such as in the QHD analysis of thin metal films in Ref. [120]. In Ref. [121] a QHD model is built from a Slater determinant of single particle plane wave states, yielding a variational derivative of the Dirac exchange energy in the hydrodynamical momentum equation, although this does not follow the phase space approach I am discussing here. More generally, correlations can be incorporated at the kinetic level via an appropriate collision integral, yielding the quantum Landau equation [122].

In the electrostatic case where the particles interact through a self-consistent Coulomb potential, the evolution equation for the reduced one-particle Wigner function is (derived in full in [119])

$$\begin{aligned} \frac{\partial f}{\partial t} + \nu \frac{\partial f}{\partial x} + \frac{iem}{2\pi\hbar^2} \iint ds d\nu' \exp\left(\frac{im\left(\nu - \nu'\right)s}{\hbar}\right) \\ \times \left[\phi\left(x + \frac{s\hbar}{2}\right) - \phi\left(x - \frac{s\hbar}{2}\right)\right] f\left(x, \nu', t\right) = 0 \end{aligned} \tag{2.2.17}$$

where the electrostatic potential obeys the Poisson equation

$$\frac{\partial^2 \phi}{\partial x^2} = \frac{e}{\varepsilon_0}\left(\int \mathrm{d}\nu f(x, \nu, t) - n_0\right), \tag{2.2.18}$$

with $\varepsilon_0$ the vacuum dielectric constant and $n_0$ the uniform background ion density. Equations (2.2.17) and (2.2.18) constitute the Wigner-Poisson model, this is the starting point from which we can derive the QHD equations. To do so we take moments of Equation (2.2.17) in velocity space, introducing the definitions for density, mean velocity and pressure

$$n(x,t) = \int f \ \mathrm{d}\nu, \quad u(x,t) = \frac{1}{n}\int f\nu \ \mathrm{d}\nu, \quad P(x,t) = m\left(\int f\nu^2 \ \mathrm{d}\nu - nu^2\right) \tag{2.2.19}$$

and taking the zeroth and first velocity moments of Equation (2.2.17) yields after lengthy algebra, respectively

$$\frac{\partial n}{\partial t} + \frac{\partial (nu)}{\partial x} = 0 \tag{2.2.20}$$

$$\frac{\partial u}{\partial t} + u\frac{\partial u}{\partial x} = \frac{e}{m}\frac{\partial \phi}{\partial x} + \frac{\hbar^2}{2m^2}\frac{\partial}{\partial x}\sum_{a=1}^{M} p_a \left( \frac{\partial_x^2 \sqrt{n_a}}{\sqrt{n_a}} \right) - \frac{1}{mn}\frac{\partial P}{\partial x}, \tag{2.2.21}$$

where the Bohm potential emerges, in this case as a summation over all states, which corresponds to the Hartree form of Equation (2.2.9) when the full many-body wavefunction is expressed as a product of single particle wavefunctions $\Psi(X,t) = \prod_{a=1}^{N_e} \psi_a(x_a,t)$ with $X = \{x_1, x_2, ..., x_{N_e}\}$. Other than the Bohm term, this is equivalent to the classical hydrodynamical equations for electrostatic plasmas, although for a quantum plasma one uses a different form for the pressure $P$.

In order to close the fluid system some equation of state is required, relating the classical pressure $P$ to the density $n$, and a simplified form of the Bohm potential. As an aside - I note that the macroscopic fluid equations are not applied in the Bohm SPH applications in the following chapters and this closure is not made - doing so would undermine the ability to determine EoS relations and transport coefficients. The closure is shown here for reference, and in Bohm SPH only a QHD-level Bohm force is applied, with the remaining force interactions described at the microscopic level. Returning to the full QHD model, typically $P$ is related to a local density approximation of the Fermi pressure [55] for a strongly degenerate fermion system

$$P(x) = P_F^D\left(n_0\right) \cdot \left( \frac{n(x)}{n_0} \right)^{5/3} \tag{2.2.22}$$

$$P_F^D\left(n_0\right) = \frac{2}{D+2} n_0 E_F\left(n_0\right) = n_0 \frac{m\nu_F^2}{D+2}, \tag{2.2.23}$$

where $\nu_F$ is the Fermi velocity associated with the Fermi energy $E_F$ and $D$ is the dimensionality. More interestingly for my purposes, the Bohm potential term is simplified via the substitution

$$\sum_{a=1}^{N} p_a \left( \frac{\partial_x^2 \sqrt{n_a}}{\sqrt{n_a}} \right) \Longrightarrow \frac{\partial_x^2 \sqrt{n}}{\sqrt{n}}. \tag{2.2.24}$$

Strictly this substitution applies if all wavefunction amplitudes of the mixture are equal, namely if $R_a(x,t) = R(x,t)$ for each $\psi_a(x,t) = R_a(x,t)\exp(iS_a(x,t)/\hbar)$. However, the substitution is also justified for length scales greater than the Fermi wavelength using linear theory [118]. Now the fluid equations are closed via an expression for a many-body Bohm potential as a function of only the global density $n$

$$V_B^{\mathrm{QHD}} = -\gamma \frac{\hbar^2}{2m} \frac{\nabla^2 \sqrt{n(\mathbf{r})}}{\sqrt{n(\mathbf{r})}}, \tag{2.2.25}$$

where $\gamma$ is a linearisation constant introduced via the substitution of Equation (2.2.24). In fact, this QHD Bohm potential also emerges in the first gradient correction to the kinetic energy in Thomas-Fermi theory [29, 121]. This also suggests that the substitution in Equation (2.2.24) is reasonable provided the density gradients are not too strong. Setting $\gamma = 1$ returns the von Weiszacker correction [123] which is exact for distinguishable particles or for bosons. For fermions in three dimensions, Kompaneets [124] and Kirzhnits [125] determined that $\gamma = 1/9$, as confirmed in Ref. [126] for the low temperature limit. More thorough analysis by Moldabekov through comparison with the limits of the Random Phase Approximation polarisation function shows that $\gamma$ differs according to wavenumber and frequency [30]. The low frequency and long wavelength limit in particular has additional temperature and density dependencies, with $\gamma$ ranging from $1/9$ at zero temperature increasing up to $1/3$ at $\theta > 1$. However at high frequencies $> \hbar k^2/2m_e$, setting $\gamma = 1$ yields the expected plasmon dispersion relation. In this work, where I am resolving the electron dynamics at sub-attosecond

resolution, I apply the high frequency limit of $\gamma = 1$.

This QHD Bohm potential can also be compared to the form of pairwise Bohm potential calculated via equilibrium pair distribution functions, as done in recent Bohmian work preceding this project [25, 127]. Here, the equilibrium pair distribution functions are calculated via a Metropolis Monte Carlo algorithm [128] with reference to an ion static structure calculation from an alternative scheme, such as DFT-MD. The pair distribution function $g_{ij}(\mathbf{x})$ [62] defines the expected density of species $j$ around a particle of species $i$ at a vector displacement $\mathbf{x}$ away, and is straightforwardly related to the actual density

$$\langle n_j(\mathbf{x})\rangle = n_j^0 g_{ij}(\mathbf{x}), \tag{2.2.26}$$

where $\langle n_j(\mathbf{x})\rangle$ in this context means the expected density of particle species $j$ at a vector displacement $\mathbf{x}$ away from a particle of species $i$, and $n_j^0$ is the average density of particle species $j$. As such, the equilibrium pairwise Bohm potential, for an isotropic system with $x$ the scalar separation, is expressed as

$$V_{B_{ij}}(x) = -\frac{\lambda_{ij}\hbar^2}{2}\left(\frac{1}{m_i} + \frac{1}{m_j}\right)\frac{\nabla^2\sqrt{g_{ij}(x)}}{\sqrt{g_{ij}(x)}}, \tag{2.2.27}$$

where the linearisation constant $\lambda_{ij}$ is determined self consistently in the Monte Carlo stage. This procedure yields a constant pairwise Bohm expression that is easily applied in a molecular dynamics simulation, and by construction, ensures that the equilibrium static structures are recovered when running dynamics. By distinction, the focus of this thesis is implementing the spatially dependent, instantaneous, QHD Bohm potential $V_B^{\mathrm{QHD}}(\mathbf{r}, t)$ for all particles in the simulation domain.

The QHD Equations ((2.2.18), (2.2.20), (2.2.21)) have been applied widely in the

quantum plasma regime in the preceding decades, particularly related to metallic nano-objects [100]. However, the limitations of the construction have not always been acknowledged and have led to unphsyical predictions, such as an attractive force between ions [129, 130]. These limitations are described in further detail in Ref.s [55, 115], but include weak electron coupling $\Gamma_q < 1$, resolvable length scales greater than the Thomas-Fermi screening length, and application of the correct linearisation constant to the QHD Bohm term.

A full derivation has been included here to both elucidate the QHD-level Bohm potential, whose full pressure tensor equivalent I will apply in the Bohm SPH model, and to recognise that the QHD equations can in general be solved using an SPH structure. As outlined in the following chapter, I will apply Bohm SPH with more SPH particles than electrons, and therefore evolve each particle according to a microscopic equation which does not require closure via an equation of state for the classical pressure. The preferable equations to solve at such a level are those of microscopic QHD, as discussed by Bonitz [115], which are equivalent in accuracy to TD-DFT with the correct occupancy.

Microscopic QHD equations follow by inserting the polar wavefunction form Equation (2.2.1) into the independent Schrödinger equations (again in one dimension) coupled via Poisson's equation and an additional exchange-correlation potential $V^{\mathrm{xc}}(n)$

$$\begin{aligned} i\hbar\frac{\partial\psi_a}{\partial t} &= -\frac{\hbar^2}{2m}\frac{\partial^2\psi_a}{\partial x^2} + [V^{\mathrm{xc}} - e\phi]\psi_a, a = 1\ldots N \\ \frac{\partial^2\phi}{\partial x^2} &= \frac{e}{\varepsilon_0}\left(\sum_{a=1}^{N} p_a\left|\psi_a\right|^2 - n_0\right). \end{aligned} \tag{2.2.28}$$

If $V^{\mathrm{xc}} \to 0$ these equations are known as the time-dependent Hartree equations. As before, solving each Schrödinger equation in real and imaginary space yields fluid equations for each wavefunction

$$\begin{aligned}
&\frac{\partial n_a}{\partial t} + \frac{\partial}{\partial x}\left(n_a u_a\right) = 0 \\
&\frac{\partial u_a}{\partial t} + u_a \frac{\partial u_a}{\partial x} = \frac{e}{m}\frac{\partial \phi}{\partial x} - \frac{\partial V^{\mathrm{xc}}}{\partial x} + \frac{\hbar^2}{2m^2}\frac{\partial}{\partial x}\left(\frac{\partial^2\left(\sqrt{n_a}\right)/\partial x^2}{\sqrt{n_a}}\right).
\end{aligned} \tag{2.2.29}$$

With $V^{\mathrm{xc}} \to 0$ this is the quantum multistream model discussed in Ref.s [131, 118].

Clearly an improvement to implementing the QHD-level Bohm potential would be to compute the Bohm potential on density distributions belonging to each individual electron in the system, as in the microscopic QHD equations. This 'Many-Fermion' Bohm potential, as also discussed in Ref. [132] was investigated but initial considerations, discussed in the following chapter, indicated that its computational cost was prohibitive, hence the reversion to QHD Bohm. Therefore 'semi-microscopic' might be an appropriate description of this first implementation of Bohm SPH.

### *2.2.3 SPH Bohm Force*

For generality, the quantum pressure tensor including non-diagonal entries as in Ref. [101], rather than a potential term, is used in the equation of motion for SPH particles (Equation (2.1.25))

$$P_B(\mathbf{r}) = -\frac{\hbar^2}{4m} n \, \nabla \otimes \nabla \ln n, \tag{2.2.30}$$

where $\otimes$ is the outer product. If $P_B$ is isotropic (setting non-diagonal terms to zero), it is related to the Bohm potential via [100]

$$\nabla \cdot P_B = n \nabla V_B. \tag{2.2.31}$$

The pressure tensor is symmetric. We can expand Equation (2.2.30) for the $xy$ value as an example

$$
\begin{aligned}
P_{B_{xy}} &= -\frac{\hbar^2}{4m} n\, \partial_x \Big[ \partial_y \ln(n) \Big] \\
&= -\frac{\hbar^2}{4m} n\, \partial_x \Big[ \frac{\partial_y n}{n} \Big] \\
&= \frac{\hbar^2}{4m} \Big[ \frac{\partial_x n\, \partial_y n}{n} - \partial_{xy} n \Big].
\end{aligned}
\tag{2.2.32}
$$

This expression is calculated in an SPH discretisation. I use the same discretisation as in Ref. [101], but with difference terms in both the first and second order density derivatives due to their improved accuracy as discussed in the previous section. The Bohm pressure for the $xy$ component of the $i$th SPH element is

$$
P_{B_{i,xy}} = \frac{\hbar^2}{4m} \sum_j \frac{m_j}{\rho_j} \Big[ \frac{\partial_x n_j\, \partial_y n_j}{n_j} - \partial_{xy} n_j \Big] W_{ij}(h_i),
\tag{2.2.33}
$$

where $W_{ij}(h_i) = W(|\mathbf{r}_i - \mathbf{r}_j|, h_i)$. The force term implemented (just the $x$ component for simplicity) is, using Equation (2.1.36),

$$
\begin{aligned}
&\frac{dv_i^x}{dt} \\
&= -\sum_j m_j \left[ \frac{\Big[ P_{B_{i,xx}}, P_{B_{i,xy}}, P_{B_{i,xz}} \Big]}{\rho_i^2 \Omega_i} \cdot \nabla_i W_{ij}(h_i) + \frac{\Big[ P_{B_{j,xx}}, P_{B_{j,xy}}, P_{B_{j,xz}} \Big]}{\rho_j^2 \Omega_j} \cdot \nabla_i W_{ij}(h_j) \right].
\end{aligned}
\tag{2.2.34}
$$

Finally, given that the Bohm pressure is not a scalar, Equation (2.1.37) for the evolution of the per-particle internal energy has to be modified. I use the following expression

$$
\frac{du_{B_a}}{dt} = \frac{1}{\Omega_a \rho_a^2} \sum_b m_b [P_{B_a} \cdot (\mathbf{v}_a - \mathbf{v}_b)] \cdot \nabla_a W_{ab}(h_a),
\tag{2.2.35}
$$

where $u_{B_a}$ is the internal energy due to the Bohm pressure for the $a$th particle. This implementation of the Bohm pressure tensor and its conservation with equation (2.2.35)

is validated in the following chapter.

# Chapter 3

# Bohm SPH Construction

Given the novelty of Bohm SPH in its approach to simulating quantum plasmas, the aim of this chapter is to provide a full overview of the model. This includes a physical description, algorithmic considerations and tests, and validation of the Bohmian and Coulomb parts of the model on analytical test problems, the quantum harmonic oscillator and hydrogen ground state.

## 3.1 Model Overview

I begin with a brief discussion of the model, and then proceed to discuss constituent parts individually, culminating in constructing the full Lagrangian of Bohm SPH. Having discussed the Bohm force and its calculation within an SPH scheme in the previous chapter, it is not repeated here, only referenced in the Lagrangian as the internal energy per unit mass.

Bohm SPH uses Gaussian particles to model the electron density. The density distribution of these SPH particles is taken to be the charge distribution and used to directly calculate the Coulomb potential which couples the electronic component with point ions. This smearing of the electrons prevents asymptotic ion-electron Coulomb attraction, similar to the wave packets in WPMD being the electron charge density,

and somewhat similar to the diffractive form of Quantum Statistical Potentials (QSP), such as the Kelbg Potential [22, 24]. Although the resolution of the SPH distribution is controlled numerically by the kernel scale lengths and not a global de Broglie type scale length as in QSP.

The lack of antisymmetry in the Hartree product used to construct the QHD Bohm potential is addressed by introduction of a repulsive symmetry potential borrowed from QSP. With access to the spatially resolved density in the SPH construction this could be changed to an approximate expression for exchange and correlation as in DFT in future implementations.

Consideration of the expected screening lengths of warm dense matter systems motivates running Bohm SPH simulations with more SPH particles than electrons $N_S > N_e$ in order to sufficiently resolve the electron density. When doing so, the overall mass and charge density of the system is kept consistent, as well as the charge to mass ratio of SPH particles. Having $N_S > N_e$ allows single electrons to have non-Gaussian shapes. Given the aim of modelling full ion-electron energy exchange (non-adiabatic), the thermal effects introduced by additional degrees of freedom must be considered. Two solutions to mitigate the effect of these additional degrees of freedom are suggested: running the system at separate ion and electron temperatures, and the introduction of confining potentials with a thermostat operating on the centre of mass velocity of each electron. Examples of both are given in the investigation of warm dense hydrogen in the following chapter. Furthermore, consideration of the average Coulomb coupling between SPH particles compared with bare electrons is relevant to the investigations of thermalisation of initially non-thermal electron distributions in Chapter 5.

As an aside, the viability of a Many-Fermion Bohm potential in an SPH scheme is also considered. With simple kernel length arguments it is demonstrated to be a factor of $N_e^2$ more expensive than an equivalent QHD treatment at the same spatial resolution.

### *3.1.1 Coulomb Forces*

A central and novel step in the hybrid SPH-MD modelling of the plasma comes in the treatment of the Coulomb interaction. The Gaussian kernel used to interpolate the electron density and Bohm pressure is taken as the real charge density distribution of each particle. While this treatment is generalisable to alternative kernel forms by following the approach of Ref. [133] for softened gravity in SPH, the Gaussian kernel is particularly useful for the Coulomb treatment due to its readily integrable form. This yields a charge density profile

$$\rho_{e_j}(\mathbf{r}) = n_j(\mathbf{r})q_j = \frac{q_j}{(\pi h_j^2)^{3/2}} \exp\Big( - \frac{|\mathbf{r} - \mathbf{r}_j|^2}{h_j^2}\Big), \tag{3.1.1}$$

with $q_j$, $\mathbf{r}_j$, and $h_j$ its fractional charge, centre of mass, and scale length (width) respectively. The Coulomb potential between an SPH particle and an ion is then calculated by the analytic integral

$$V_{ij} = \int d\mathbf{r} \frac{Ze}{4\pi\epsilon_0 |\mathbf{r} - \mathbf{r}_i|} \rho_{e_j}(\mathbf{r}), \tag{3.1.2}$$

where $\mathbf{r}_i$ is the position of the ion, and $Z$ its charge, yielding with $r_{ij} = |\mathbf{r}_i - \mathbf{r}_j|$,

$$V_{ij} = \frac{Zeq_j}{4\pi\epsilon_0 r_{ij}} \operatorname{erf}\Big(\frac{r_{ij}}{h_j}\Big). \tag{3.1.3}$$

The integral in (3.1.2) assumes a simple point ion with $1/r$ Coulomb interaction. This could also be changed to a pseudopotential to include the effect of core electrons, the form of which can be Gaussian-decomposed to enable analytical solutions.

Equation (3.1.3) which couples the electronic and ionic components through the elec-

trostatic Coulomb potential is what enables energy exchange between the components, and represents an important distinction to the usual jellium model for ions used in QHD equations. As shown in Section 2.2.2, the ion charge is generally included as a homogeneous neutralising background in the Poisson Equation (2.2.18) for Wigner-Poisson or QHD applications. Now instead the ion charge has spatial and time dependence, $n_i(\mathbf{r},t) = \sum_a^{N_i} \delta(\mathbf{r} - \mathbf{r}_a, t)$ for $N_i$ point ions.

The procedure for the pairwise SPH particle Coulomb potential is similar, integrating across both Gaussian charge clouds

$$V_{jk} = \int\int d\mathbf{r} d\mathbf{r}' \frac{\rho_{e_j}(\mathbf{r})\rho_{e_k}(\mathbf{r}')}{4\pi\epsilon_0|\mathbf{r}-\mathbf{r}'|}, \tag{3.1.4}$$

yielding for particles $j$ and $k$

$$V_{jk} = \frac{q_j q_k}{4\pi\epsilon_0 r_{jk}} \operatorname{erf}\left(\frac{r_{jk}}{\sqrt{h_j^2 + h_k^2}}\right). \tag{3.1.5}$$

In cases where the number of SPH particles exceeds the number of electrons, Coulomb potentials between SPH particles assigned to the same parent electron are removed. However if such 'same - electron' particles are spatially near one another in the simulation domain, such that their respective kernel scale lengths become functions of each other's position via Equation (2.1.13), there will be a dynamic-kernel force between the same-electron particles. This is immediately apparent when computing the derivative of Equation (3.1.5) with respect to position coordinate $\mathbf{r}_l$

$$\frac{\partial V_{jk}}{\partial \mathbf{r}_l} = \left.\frac{\partial V_{jk}}{\partial \mathbf{r}_l}\right|_{h_m} + \sum_m \left.\frac{\partial V_{jk}}{\partial h_m}\right|_{\mathbf{r}_l} \frac{\partial h_m}{\partial \mathbf{r}_l}, \tag{3.1.6}$$

where the forces in the second term on the RHS can be described as 'dynamic-kernel' forces.

It is instructive to expand this expression to the exact form implemented within Bohm SPH. Starting with the first term on the right hand side of Equation (3.1.6), which is non-zero only for $l = j$ or $l = k$, and defining $h_j^2 + h_k^2 = M_{jk}^2$

$$\left.\frac{\partial V_{jk}}{\partial \mathbf{r}_j}\right|_{\{h\}} = \frac{\xi_{jk}}{r_{jk}}\Big[\left(\frac{2}{\sqrt{\pi}M_{jk}}\right)\exp\left(-\frac{r_{jk}^2}{M_{jk}^2}\right) - \frac{1}{r_{jk}}\operatorname{erf}\left(\frac{r_{jk}}{M_{jk}}\right)\Big]\hat{\mathbf{r}}_{jk}, \tag{3.1.7}$$

where $\mathbf{r}_{jk} = \mathbf{r}_j - \mathbf{r}_k$ as before. The dynamic kernel forces term are expanded via the chain rule as

$$\sum_m \left.\frac{\partial V_{jk}}{\partial h_m}\right|_{\mathbf{r}_l} \frac{\partial h_m}{\partial \mathbf{r}_l} = \sum_m \left.\frac{\partial V_{jk}}{\partial h_m}\right|_{\mathbf{r}_l} \frac{\partial h_m}{\partial \rho_m}\frac{\partial \rho_m}{\partial \mathbf{r}_l}. \tag{3.1.8}$$

The derivative of the pairwise Coulomb potential with respect to kernel scale length $h_m$ is

$$\left.\frac{\partial V_{jk}}{\partial h_m}\right|_{\mathbf{r}_l} = -\frac{2\xi_{jm}h_m}{\sqrt{\pi}M_{mj}^3}\exp\left(-\frac{r_{mj}^2}{M_{mj}^2}\right). \tag{3.1.9}$$

Then, the remaining terms follow from the SPH treatment of dynamic kernel lengths and the definition of density, as in Equations (2.1.12) (2.1.13) and (2.1.35)

$$\frac{\partial h_m}{\partial \rho_m} = \frac{-h_m}{3\rho_m} \tag{3.1.10}$$

$$\frac{\partial \rho_m}{\partial \mathbf{r}_l} = \frac{1}{\Omega_m} \sum_o m_o \nabla_l W_{mo}(h_m)(\delta_{ml} - \delta_{ol}), \tag{3.1.11}$$

where $\nabla$ retains its meaning from the SPH section of taking the spatial derivative while keeping the scale length constant. I insert these expressions into an equation for the total electronic Coulomb force acting on an SPH particle

$$\mathbf{F}_a^{ee} = -\frac{\partial \mathrm{V}_C^{ee}}{\partial \mathbf{r}_a} = -\frac{\partial}{\partial \mathbf{r}_a} \sum_{j \neq k} \frac{\xi_{jk}}{r_{jk}} \operatorname{erf}\left(\frac{r_{jk}}{M_{jk}}\right), \tag{3.1.12}$$

where $\xi_{jk} = q_j q_k / 4\pi\epsilon_0$. This expression is the electronic Coulomb force acting on the $a$th SPH particle. Implementing equations (3.1.9) to (3.1.11) and after some lengthy algebra, this electronic force is expressed in compressed form as

$$\mathbf{F}_a^{ee} = \Gamma_a - \theta_a \nabla_a \rho_a - \sum_{k \neq a} \theta_k m_a \nabla_a W_{ak}(h_k) \tag{3.1.13}$$

where the full expressions are

$$\begin{aligned} \Gamma_b = \sum_{k \neq b} \frac{\xi_{bk}}{r_{bk}} \Big[ & \frac{1}{r_{bk}} \operatorname{erf}\left(\frac{r_{bk}}{M_{bk}}\right) \\ & - \left(\frac{2}{\sqrt{\pi} M_{bk}}\right) \exp\left(-\frac{r_{bk}^2}{M_{bk}}\right) \Big] \hat{\mathbf{r}}_{bk}, \end{aligned} \tag{3.1.14}$$

$$\theta_b = \sum_{k \neq b} \frac{2 h_b^2 \xi_{bk}}{3 \rho_b \Omega_b \sqrt{\pi} M_{bk}^3} \exp\left(-\frac{r_{bk}^2}{M_{bk}^2}\right). \tag{3.1.15}$$

The full Coulomb force term for an electronic SPH particle interacting with ions, starting from the potential Equation (3.1.3), is almost exactly equivalent, but with

$M_{bk}$ being replaced by $h_b$ and one of the SPH charges replaced by the ion charge $Z_i e$. Notably however, the Coulomb force acting on the ion is only given by the $\Gamma$ term above, since the ion coordinates do not determine the dynamic SPH scale lengths.

Given that the Coulomb interaction is long range, being proportional to $1/r$, and that I will be simulating systems with periodic boundary conditions, I desire an efficient scheme for computing the electrostatic interactions of particles in the simulation domain with their infinite projections. This is provided by the Ewald decomposition [134–136] which splits the very slowly converging sum over the Coulomb potential into two sums which converge exponentially fast via application of the error function

$$\frac{1}{r} = \frac{\mathrm{erf}(\alpha r)}{r} + \frac{\mathrm{erfc}(\alpha r)}{r} \tag{3.1.16}$$

where erfc() is the complementary error function $= 1 - \mathrm{erf}()$. The erfc term has asymptotic behaviour at $r = 0$ and vanishes exponentially as $r$ gets large, whereas the erf term has a finite value at $r = 0$ and a long range tail. The erfc term is, with appropriate choice of $\alpha$ computed efficiently in real space, whereas the erf term requires computation in reciprocal space, with computational expense reduced via use of a fast Fourier transformation. As a well established method, details of computing such a scheme are omitted but can be found in Ref.s [135, 136].

The Ewald decomposition is compatible with the use of Gaussian charge clouds provided the real space computation has a cutoff radius sufficiently larger than the charge cloud overlap. Implementation is subtly different to standard Ewald decomposition, with the entire electron-ion and electron-electron Coulomb interactions computed in real space via Equations (3.1.3) and (3.1.5) out to a cutoff $r_C$, and then for $r > r_C$ treated as point particle Coulomb interactions when the long range part is computed in reciprocal space via the erf term. This treatment works since the charge clouds appear as point particles at sufficient distance. Note that $\alpha$ is tuned to ensure the erf term dominates after the cutoff $r_C$. The condition I apply in this work is that the real space

Coulomb cutoff exceeds twice the full width half maximum of the average Gaussian charge cloud $r_C > 4\sqrt{\ln(2)}\,\overline{h}$, typically by a factor of 1.2.

### *3.1.2 Symmetry Effects*

When dealing with a many-fermion system indistinguishable particles cannot exist in the same state. Construction of the QHD Bohm potential is ignorant of this requirement so we must include symmetry effects via an additional potential. Having focused on implementation of the Bohm term in the first iteration of this model rather than highly accurate exchange effects, I make a practical approximation to include exchange effects by borrowing a spin-averaged symmetry potential from QSP, denoted $V_P$ for Pauli exclusion. Such local pair-potentials are generally derived for weakly coupled electrons [137]. Precisely I employ the temperature dependent equation derived in Ref. [23] by Minoo *et al.* and subsequently applied in MD simulations of thermal relaxation such as Ref.s [138, 139]

$$V_P = k_B T \ln(2)\, \exp\left[-\frac{1}{\ln(2)}\left(\frac{r}{\lambda_{ee}}\right)^2\right], \tag{3.1.17}$$

where $\lambda_{ee} = \hbar\,(k_B T m_e)^{-1/2}$. Taking the derivative of the Pauli potential between the $i$th and $j$th particle, where $\mathbf{r}_{ij} = \mathbf{r}_i - \mathbf{r}_j$ yields the force

$$\mathbf{F}_{P_i} = -\nabla_i V_P = 2k_B T \left(\frac{\mathbf{r}_{ij}}{\lambda_{ee}^2}\right) \exp\left[-\frac{1}{\ln(2)}\left(\frac{r}{\lambda_{ee}}\right)^2\right]. \tag{3.1.18}$$

The target temperature is used in Equation (3.1.18) rather than the instantaneous temperature. When using sub-electron resolution in the model, with $N_{ppe}$ SPH particles per electron, the interaction is scaled by $1/N_{ppe}^2$, and interactions between 'same-electron' particles are removed to prevent self-interaction. This conserves the total

Pauli potential in the system and, if same-electron particles are on top of one another, replicates the pairwise electron interaction ($N_{ppe} = 1$). This factor naturally appears in the SPH discretisation of the Pauli potential, as shown later.

It is noteworthy that inclusion of the repulsive Minoo potential in the model helps protect against the tensile instability of SPH [140, 141, 97], which can otherwise result in an unphysical clustering of SPH particles. Indeed, I have not observed the tensile instability in applications of Bohm SPH thus far.

Beyond the spin averaged term of Ref. [23], pairwise symmetry potentials can be derived corresponding to singlet and triplet states, as in work by Filinov *et al.* [137]. While not used in this work, they are described here as a possible improvement to the spin averaged term (with $S$ singlet (+) and $T$ triplet (-))

$$V_{S/T} = -k_B T \ln\left[1 \pm \exp\left(-\left(\frac{r}{\lambda_{ee}}\right)^2\right)\right]. \tag{3.1.19}$$

To capture the right proportion of singlet and triplet interactions the SPH particles must be subdivided into four spin groups such as $\uparrow_a \downarrow_a \uparrow_b \downarrow_b$, where only the combinations $\uparrow_a\downarrow_b$ and $\uparrow_b\downarrow_a$ interact through the singlet potential, and the rest through the triplet. The spin averaged symmetry term from Minoo is compared with the singlet and triplet forms of Filinov in Figure 3.1; clearly all the potential interactions quickly terminate at distances greater than $2\lambda_{ee}$.

Furthermore, given that the SPH construction gives access to the continuous density profile $n(\mathbf{r})$ and gradients thereof, forms for exchange and correlation commonly used in DFT are implementable. This has been done in QHD studies on thin metal films in Ref. [120], where a functional from Ref.s [142, 143] was applied. A simple form for the exchange potential at zero temperature is provided by the variational derivative of Dirac's exchange functional [144] to which the local density approximation (LDA) is

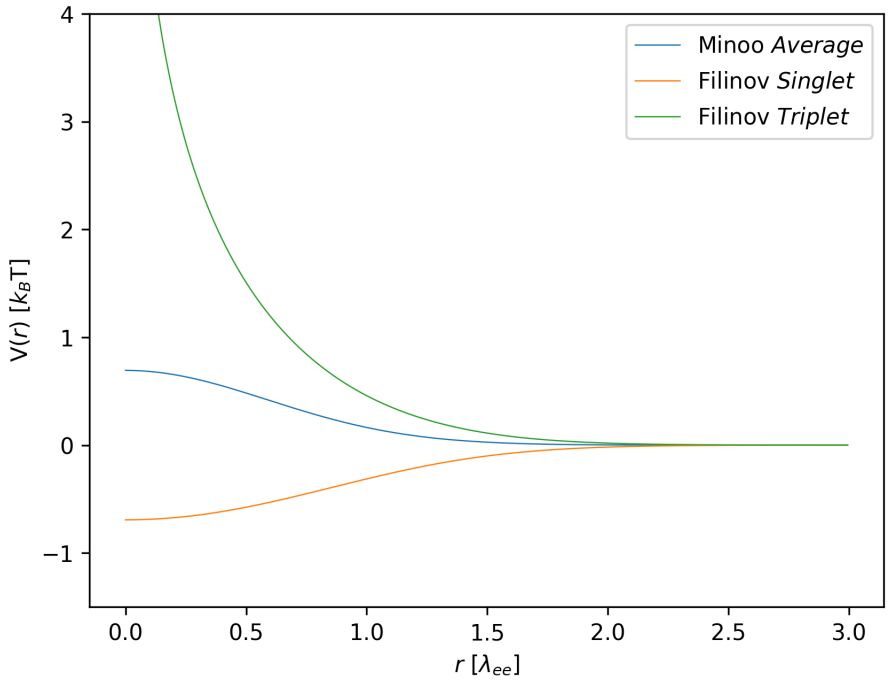


Figure 3.1: Pairwise symmetry potentials from QSP: Minoo spin averaged symmetry potential and Filinov singlet and triplet potentials, as in equations (3.1.18) and (3.1.19).

applied, as recovered in the QHD model of Ref. [121] starting from an antisymmetrised total wavefunction

$$V_D = -\frac{e^2}{4\pi\epsilon_0}\left(\frac{3n(\mathbf{r})}{\pi}\right)^{1/3}. \tag{3.1.20}$$

Various approximations of the exchange-correlation functional exist in the DFT literature - see Ref.s [145, 146].

### *3.1.3 SPH Resolution*

A feature of Bohm SPH is the ability to resolve the electrons with arbitrary resolution, dependent only on the number of SPH particles used. Having made Gaussian SPH kernels real charge clouds, at typical WDM density and temperatures, I must use more SPH particles than electrons to ensure that the electron charge density is well resolved.

A useful metric for determining whether the charge density is well resolved is comparison of the average kernel scale length $\overline{h}$ to the expected screening length of the plasma $\lambda_S$, I desire $\overline{h} < \lambda_S$. In the classical and quantum limits the relevant screening lengths are the Debye $\lambda_D$ and Thomas Fermi $\lambda_{TF}$ lengths respectively. The screening length $\lambda_S$ is given by equation 6 of Ref. [46], valid for any degeneracy, returning $\lambda_D$ and $\lambda_{TF}$ in the appropriate limits

$$\lambda_S^{-2} = \kappa_e^2 = \frac{n_e e^2}{\epsilon_0 k_B T_e} \frac{F_{-1/2}(\eta_e)}{F_{1/2}(\eta_e)}, \tag{3.1.21}$$

where $\eta_e$ is the dimensionless chemical potential $\mu_e / k_B T_e$, and $F_\nu$ denotes a Fermi integral of order $\nu$.

The requirement of good neighbour support for SPH schemes [89], in particular the condition of scale length being greater than neighbour separation $h > \Delta$, means that the kernel scale lengths of the particles cannot be reduced arbitrarily. This condition must be enforced in Bohm SPH to ensure the Bohmian interactions are properly communicated. Instead, I increase the number of particles. For the remainder of this thesis, when discussing systems with $N_{ppe}$ SPH particles per electron, I have scaled all SPH particle masses and charges by $1/N_{ppe}$ to ensure the correct mass and charge density. Via Equation (2.1.13), the average kernel scale length $\overline{h}$ for a system with electron density $n_e$ is defined as

$$\overline{h} = \zeta (N_{ppe} n_e)^{-1/3}. \tag{3.1.22}$$

Figure 3.2 demonstrates that we require $N_{ppe} = 32$ when setting $\zeta = 1.3$ to resolve the warm dense hydrogen system investigated in Chapter 4 with Wigner Seitz radius $r_s = (3/4\pi n_e)^{1/3} = 1.75\,\mathrm{a_B}$ and degeneracy parameter $\theta = k_B T / E_F = 1.32$, with $\mathrm{a_B}$

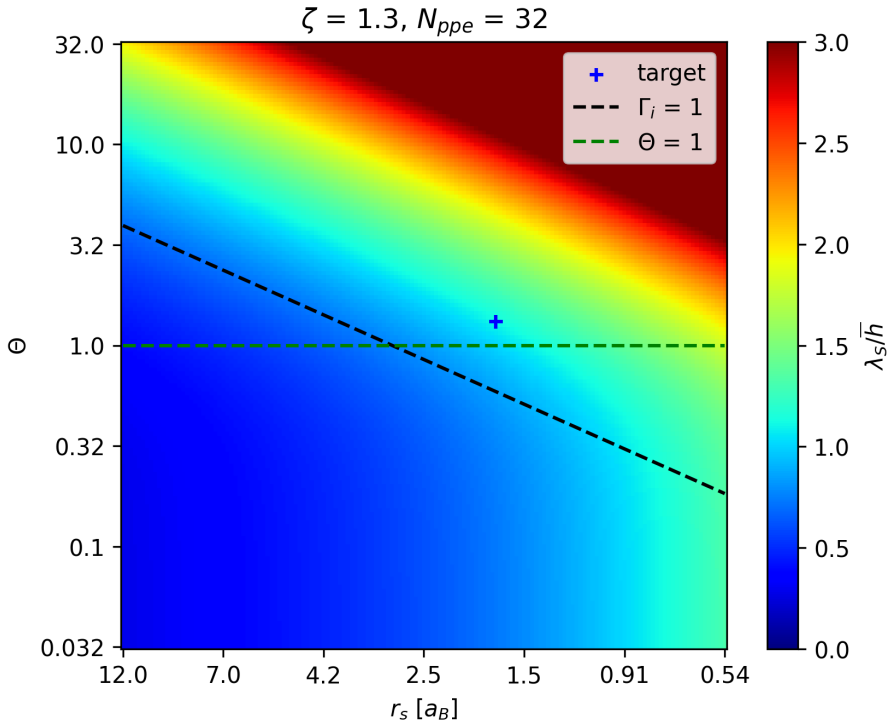


Figure 3.2: Ratio of the screening length $\lambda_S$ to the average SPH kernel scale length $\overline{h}$ for ionised hydrogen with $N_{ppe} = 32$. The 'target' system is investigated in Chapter 4.

the Bohr radius and $E_F$ the Fermi energy.

### *3.1.4 Thermal Effects*

When introducing more SPH particles to better resolve the electron density, I must consider the implication of the ion and electron systems having the same temperature since I am not employing the Born-Oppenheimer approximation. Additional SPH particles are additional degrees of freedom, which increase the amount of translational thermal energy in the electron system, as demonstrated by equipartition

$$\sum_i^N \frac{1}{2} m_i \langle \mathbf{v}_i^2 \rangle = \frac{3}{2} N k_B T, \tag{3.1.23}$$

where $T$ is the target temperature of the system. To demonstrate a simple scaling we assume all $N_S = N_e N_{ppe}$ SPH particles (with $N_e$ the number of electrons) have

identical masses $m_s$ and move at an average speed $\overline{v}$

$$\frac{N_S m_s \overline{v}^2}{2} = \frac{3}{2} N_S k_B T. \tag{3.1.24}$$

When we have $N_{ppe}$ SPH particles per electron, the SPH particle mass $m_s = m_e/N_{ppe}$ to ensure the correct mass density, giving

$$\frac{m_e \overline{v}^2}{2N_{ppe}} = \frac{3}{2} k_B T. \tag{3.1.25}$$

Rearrangement of Equation(3.1.25) yields

$$\overline{v} = \sqrt{\frac{3N_{ppe} k_B T}{m_e}}, \tag{3.1.26}$$

demonstrating how the average, and indeed the thermal, speed of the SPH particles scales proportionally to $\sqrt{N_{ppe}}$, causing unphysical Bohm-Gross dispersion in the plasmon feature and spurious ion screening. This effect is demonstrated in Section 4.1, where Bohm SPH is run for a system of warm dense hydrogen scanning the resolution $N_{ppe}$ while keeping the temperature fixed.

We notice that Particle in Cell (PIC) simulations have a similar consideration. There the base unit of charge also does not correspond to a single electron, but is a macroparticle (rather than a micro SPH particle) representing a large number of electrons. The temperatures of these macroparticles are typically scaled by the macroparticle weight to address unphysical velocities [147, 148]. In my case I cannot apply a general scaling as the ions in our model are not treated identically to the electrons, but as point-particles whose temperature must be fixed at $T$. One approach for addressing this problem is to

model the ions and electrons under separate thermostats, with ions at $T$ and electrons at $T/N_{ppe}$. This is done in Section 4.2, which yields compelling results for the ion static and dynamic structure, but not for the electronic structure. When running a two temperature system with large values of $N_{ppe}$, a strong ion thermostat is required to prevent the ions equilibriating with the SPH bulk.

An alternative approach is to introduce a quadratic confining potential to localise individual electrons and to apply a thermostat to their centres of mass (CoM) which are subsequently released into an NVE (microcanonical) ensemble. After equilibriating these centres of mass at the target temperature, plasmon data computed from their trajectories then avoids the numerical Bohm-Gross dispersion mentioned above. Furthermore, the trajectory data is collected while the whole system is in NVE rather than the ionic and electronic components being maintained at separate temperatures. This approach is applied in Section 4.3, and, contingent on the strength of confinement applied and subsequent electron size achieved, produces good results for both the ionic and electronic structure when compared to an anisotropic WPMD calculation [58].

SPH particles are allocated a parent electron and forced toward their centre of mass via the potential

$$V_c(\mathbf{r}) = g|\mathbf{r} - \mathbf{R}|^2, \tag{3.1.27}$$

where $g$ is varied to adjust the size of the parent electron $\mathbf{r}$ is the position of a target particle and the centre of mass $\mathbf{R} = \sum_j \mathbf{r}_j / N_{ppe}$ for equal mass particles. In a system with periodic boundary conditions, the centre of mass is calculated according to the formulation of Ref. [149] discussed later. The confinement force on a particle is given by

$$\mathbf{F_{C_i}} = -\frac{\partial \sum_j V_{C_j}(\mathbf{r_j})}{\partial \mathbf{r}_i}, \tag{3.1.28}$$

where the sum is over the $N_{ppe}$ SPH particles which belong to the same centre of mass. This is expanded as

$$\mathbf{F_{C_i}} = -\frac{2g}{N_{ppe}} \left[ (\mathbf{r}_i - \mathbf{R}) \left( N_{ppe} - 1 \right) - \sum_{j \neq i} (\mathbf{r}_j - \mathbf{R}) \right]. \tag{3.1.29}$$

In a box without periodic boundary conditions, this simply reduces to

$$\mathbf{F_{C_i}} = 2g(\mathbf{R} - \mathbf{r}_i), \tag{3.1.30}$$

but with periodic boundary conditions, the vectors $\mathbf{r}_a - \mathbf{R}$ need to be computed using the correct (closest) projection of $\mathbf{R}$, which can be the overall centre of mass plus or minus a box length in all principal directions $\mathbf{R} \pm L\hat{\mathbf{i}}$. This does not necessarily reduce to Equation (3.1.30).

As stated earlier, the repulsive Coulomb and Pauli potentials between particles belonging to the same electron are removed, while retaining the Bohm interaction. I perform a scan of $g$ values when comparing outputs from Bohm SPH to anisotropic WPMD in Section 4.3.

A final consideration is the average Coulomb coupling of the SPH particles compared to real electrons. This is pertinent when considering the thermalisation of an initially non-thermal electron kinetic energy distribution, as performed in Chapter 5. There are further parallels with PIC where the incorrect coupling between charge macroparticles introduces a numerical heating in atmospheric pressure plasmas [148]. The SPH particle coupling is given, for an electronic distribution at density $n_e$ and temperature $T_e$, with $a_S$ the Wigner Seitz radius and $h_S$ the average scale length

$$\begin{aligned}\Gamma_S &= \frac{q_S^2}{4\pi\epsilon_0 a_S k_B T_e}\,\mathrm{erf}\left(\frac{a_S}{\sqrt{2}h_S}\right) \\ &= \frac{(e/N_{ppe})^2}{4\pi\epsilon_0 k_B T_e}\left(\frac{4\pi N_{ppe} n_e}{3}\right)^{1/3}\mathrm{erf}\left(\frac{(N_{ppe}n_e)^{1/3}}{\sqrt{2}\zeta}\left(\frac{3}{4\pi N_{ppe}n_e}\right)^{1/3}\right) \\ &= \Gamma_e N_{ppe}^{-5/3}\,\mathrm{erf}\left(\frac{1}{\sqrt{2}\zeta}\left(\frac{3}{4\pi}\right)^{1/3}\right).\end{aligned} \tag{3.1.31}$$

Here clearly the average SPH particle coupling differs from that of bare (classical) electrons at the same conditions by a scaling of $N_{ppe}^{-5/3}$ and an error function term associated with the Gaussian charge clouds.

### *3.1.5 Many Fermion Bohm Potential*

I now examine the more accurate Many-Fermion (MF) Bohm potential [132], with the Bohm potential calculated on the density distribution of each individual electron $n_a = |\psi_a|^2$ rather than the global density $n = \sum_{a=1}^{N} p_a|\psi_a|^2$ as in the QHD Bohm potential. As discussed in Section 2.2.2, the MF Bohm potential appears in the unclosed quantum fluid model derived from the Wigner-Poisson model and emerges naturally in the microscopic QHD equations which are equivalent in accuracy to the TD-DFT equations.

With individual electron densities now appearing in the equations of motion, the density and dynamic scale length calculations have to be adapted accordingly; for the $i$th SPH particle of the $a$th electron

$$\rho_i^a = \sum_j^{N_{ppe}} m_j^a W(\mathbf{r}_i^a - \mathbf{r}_j^a, h_i^a) \tag{3.1.32}$$

$$h_i^a = \zeta\left(\frac{m_i^a}{\rho_i^a}\right)^{1/d}. \tag{3.1.33}$$

The difficulty of this approach is that each electron is now an individual fluid according to the SPH fixed-point dynamic kernel solver, hence one requires sufficient particles $N_{ppe}$ to resolve it across the entire simulation domain. Moreover, to treat realistic quantum plasmas the same screening arguments of Section 3.1.3 apply. Comparing the average kernel scale lengths, via Equation (3.1.22), of QHD and MF kernels quickly indicates the prohibitive cost of the latter. The average density of a single electron $n_a$ in the box is $m_e/L^3$ rather than $N_e m_e/L^3$ for the global density $n$, so the ratio is

$$\frac{\overline{h}^{MF}}{\overline{h}^{QHD}} = N_e^{1/3}. \tag{3.1.34}$$

Therefore to meet the same spatial resolution requirements of $\overline{h} < \lambda_S$ the electron must be further subdivided by a factor of $N_e$ in the MF approach. Unfortunately, given that practical cutoff radii for SPH are determined by such average scale lengths and must then be the same in both cases, the computational cost of the Coulomb interaction in MF SPH would be $N_e^2$ times greater than QHD (caused by the additional pairwise interactions). Such an MF Bohm scheme has been implemented but initial tests confirmed the substantial cost.

Given this severe $N_e^2$ scaling, the QHD Bohm potential and associated density and scale lengths are the focus of this work. Furthermore, when running MF Bohm non-adiabatically with ions the additional factor of $N_e$ degrees of freedom amplifies the problematic thermal effects discussed in Section 3.1.4. While a confining potential could also be used in the MF approach to address this, the MF approach is then likely obsolete as I expect it to yield similar density distributions as the QHD approach with confining potentials.

### *3.1.6 Full Lagrangian*

It is instructive to consider the full Lagrangian of the Bohm SPH model. Using the interactions listed above, I define a Lagrangian for a quantum plasma system with electron density $n(\mathbf{r})$ and $N_I$ point ions. To start, I include self interactions and omit the confining potential

$$\begin{aligned}\mathfrak{L} = &\sum_{i=1}^{N_I}\left[\frac{1}{2}M_i\mathbf{v}_i^2 - \sum_{j>i}^{N_I}\frac{(Ze)^2}{4\pi\epsilon_0|\mathbf{r}_i-\mathbf{r}_j|}\right] \\ &+\int d\mathbf{r}\, n(\mathbf{r})\Big\{\frac{1}{2}m_e\mathbf{v}(\mathbf{r})^2 - m_e u_B(\mathbf{r}) - \sum_i^{N_i}\frac{Ze^2}{4\pi\epsilon_0|\mathbf{r}_i-\mathbf{r}|} \\ &-\int d\mathbf{r}'\,\frac{n(\mathbf{r}')}{2}\left[\frac{e^2}{4\pi\epsilon_0|\mathbf{r}'-\mathbf{r}|} + V_P(|\mathbf{r}'-\mathbf{r}|)\right]\Big\}\end{aligned} \tag{3.1.35}$$

where $M_I$ is the ion mass, $Z$ its ionisation, $u_B$ the internal QHD Bohm energy per unit mass associated with the pressure tensor, and $n$ the number density of electrons, with a factor of 1/2 included in the second integral to prevent double counting. Now, for the electron kinetic, Bohm, and Pauli terms, I apply the SPH discretisation, while for the Coulomb interactions I integrate exactly using the charge density distribution given by the SPH Gaussian kernels. This procedure eliminates all the integral terms, replacing them with summations that can be implemented into a molecular dynamics structure. Furthermore, I remove the Coulomb and Pauli interactions between SPH particles belonging to the same parent electron and, if enabled, introduce confining potentials for each electron. With $N_S$ SPH particles I have

$$
\begin{aligned}
\mathfrak{L} = & \sum_{i=1}^{N_I} \Big( \frac{1}{2} M_i \mathbf{v}_i^2 - \sum_{j>i}^{N_I} \frac{(Ze)^2}{4\pi\epsilon_0 r_{ij}} \Big) \\
& + \sum_{a=1}^{N_S} \Big\{ \frac{1}{2} m_a \mathbf{v}_a^2 - m_a u_{B_a} - \sum_{i=1}^{N_I} \Big[ \frac{Z e q_a}{4\pi\epsilon_0 r_{ia}} \operatorname{erf}\Big( \frac{r_{ia}}{h_a} \Big) \Big] \\
& - \sum_{b=1}^{N_S'} \frac{1}{2} \Big[ \frac{q_a q_b}{4\pi\epsilon_0 r_{ab}} \operatorname{erf}\Big( \frac{r_{ab}}{\sqrt{h_a^2 + h_b^2}} \Big) + \frac{1}{N_{ppe}^2} V_P(r_{ab}) \Big] \Big\} \\
& - \sum_{c=1}^{N_e} \sum_{d=1}^{N_{ppe}} \Big[ g |\mathbf{r}_d - \mathbf{R}_c|^2 \Big].
\end{aligned}
\tag{3.1.36}
$$

Here the SPH variables have subscript $a$ and $b$, with $m_a$ the SPH particle mass, $q_a$ its fractional charge, $h_a = h_a(\rho_a)$ its dynamic kernel width, and $r_{ab} = |\mathbf{r}_a - \mathbf{r}_b|$. $N_S'$ indicates that particles $b$ belonging to the same electron as particle $a$ are excluded, and where the index $c$ runs over $N_e$ whole electrons and $d$ over $N_{ppe}$ members of each electron.

As discussed at the end of Section 2.2.2, this Lagrangian, with more SPH particles than electrons $N_S \geq N_e$, yields 'semi-microscopic' equations of motion for the quantum plasma. The 'semi' term is added due to use of the QHD-level Bohm pressure as standard in the first implementation of Bohm SPH, rather than a Many-Fermion Bohm pressure.

## 3.2 Implementation into LAMMPS

Bohm SPH has been implemented via modification of LAMMPS, an open source classical molecular dynamics code with a focus on modeling materials [150]. Specifically, the LAMMPS version of 3 March 2020 has been edited and extended. This includes routines for the Bohm, Pauli, real-space Coulomb interactions (compatible with the Ewald decomposition), a fixed point iterator for computing kernel scale lengths from local densities, confining potentials compatible with Periodic Boundary Conditions [149], as well

as a Nosé-Hoover thermostat [151] that operates on the electron centres of mass rather than the SPH particles. Simulations are performed using a velocity-Verlet integrator.

### *3.2.1 Dynamic Kernel Fixed Point Iterator*

To calculate the Gaussian kernel scale lengths according to their local density a fixed-point iterator is implemented

$$h_b^{m+1} = \zeta \left( \frac{m_b}{\rho_b(h_b^m)} \right)^{\frac{1}{d}}, \tag{3.2.1}$$

where the superscript refers to the $m$th iteration. Other root finding algorithms can be employed for this task, often Newton-Raphson [97].

The convergence of a fixed-point iterator was tested for the target warm dense hydrogen system investigated in the following chapter: a density of $n_e = 3.006\,\mathrm{g/cm^3}$, with 512 protons and 16384 SPH electron particles ($N_{ppe} = 32$). The SPH particles were initialised in a particular random spatial distribution and all assigned the average kernel scale length (3.1.22). The scale lengths were then updated for this arrangement, scanning the number of iterations until convergence was achieved at $m = 11$ . The final scale lengths after m iterations of the fixed point calculation above were compared to the scale lengths at $m = 11$. The average fractional difference in scale lengths for the $m$th iteration, $\Delta^m_{\{h\}}$, was computed according to

$$\Delta^m_{\{h\}} = \sum_a^{N_S} |1 - \frac{h_a^m}{h_a^{11}}| \,/\, N_S \tag{3.2.2}$$

where $N_S$ is the number of SPH particles. This is plotted in Figure 3.3. Note that even for a random initial arrangement, just one iteration of the calculator yields scale lengths that are on average only 0.2% different from the converged values.

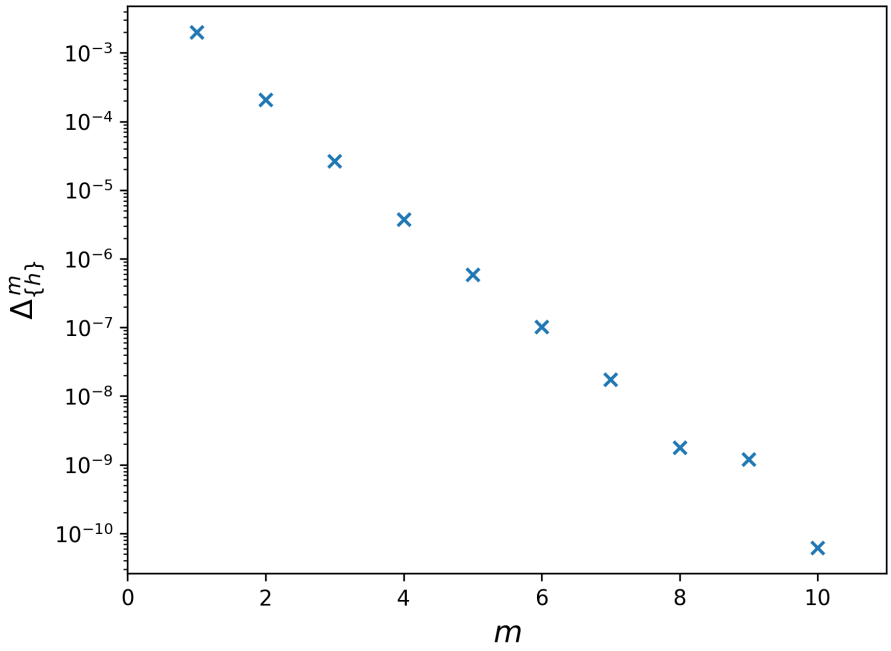


Figure 3.3: Convergence of fixed point calculation of local densities and kernel scale lengths $\{h\}$ according to Equation (3.2.1). Computed for a random initial SPH particle arrangement at the density of the target warm dense hydrogen system ($n_e = 3.006\,\mathrm{g/cm^3}$). The average fractional difference in scale lengths for the $m$th iteration from the $m = 11$ (converged) values are plotted according to Equation (3.2.2).

Once the fixed-point calculator for the SPH scale lengths terminates, the $\Omega$ values, in Equation (2.1.32), are computed for each particle. As described in Section 2.1.3, these values are required for density derivatives when using dynamic kernel scale lengths. The exact calculation of $\Omega$ values for Gaussian kernels is included here for reference:

$$\begin{aligned}\Omega_a &= 1 + \frac{h_a}{3\rho_a}\frac{\partial \rho_a}{\partial h_a} \\ &= 1 + \frac{h_a}{3\rho_a}\sum_b m_b \frac{\partial W_{ab}(h_a)}{\partial h_a},\end{aligned} \tag{3.2.3}$$

where for a Gaussian kernel $W_{ab}$ the derivative with respect to scale length is

$$\begin{aligned}\frac{\partial W_{ab}(h_a)}{\partial h_a} &= \frac{\partial}{\partial h_a}\left[\frac{1}{(2\pi h_a^2)^{3/2}}\exp\left(-\frac{|\mathbf{r}_a-\mathbf{r}_b|^2}{2h_a^2}\right)\right] \\ &= \left[\frac{1}{(2\pi h_a^2)^{3/2}}\left(-\frac{|\mathbf{r}_{ab}|^2}{2}(-2h_a^{-3})\right)+\left(-\frac{3}{h_a^4(2\pi)^{3/2}}\right)\right]\exp\left(-\frac{|\mathbf{r}_{ab}|^2}{2h_a^2}\right) \\ &= \left[\frac{|\mathbf{r}_{ab}|^2}{h_a^3}-\frac{3}{h_a}\right]W_{ab}(h_a).\end{aligned} \tag{3.2.4}$$

### *3.2.2 Centre of Mass Considerations*

Posed as a possible solution to numerical Bohm-Gross dispersion in the plasmon and spurious ion screening previously in Section 3.1.4, a confining potential to localise SPH particles belonging to the same electron is implemented; importantly it must be compatible with the use of periodic boundary conditions (PBC). This requires identifying the centre of mass (COM) of same-electron SPH particles in PBC, which differs from the case of no-interaction across simulation boundaries. To compute the correct COM with PBC I follow the procedure of Ref. [149], which is outlined in Figure 3.4. Each dimension's (of length $L$) coordinate is expressed as an angle

$$\theta_i = 2\pi x_i/L. \tag{3.2.5}$$

Using Figure 3.4 as a guide, this angle generates two new coordinates for each position, which projects the position of the coordinate $x_i$ onto a circle of radius 1

$$\begin{aligned}\sigma_i &= \cos(\theta_i) \\ \tau_i &= \sin(\theta_i),\end{aligned} \tag{3.2.6}$$

from which averages are calculated

$$\begin{aligned} \overline{\sigma} &= \frac{\sum_i^{N_{ppe}} m_i \sigma_i}{M} \\ \overline{\tau} &= \frac{\sum_i^{N_{ppe}} m_i \tau_i}{M}, \end{aligned} \tag{3.2.7}$$

where $M$ is the total mass of the $N_{ppe}$ particles belonging to the target electron. These average coordinates give the COM within the circle (see Figure 3.4 b). Then the coordinate COM is extracted by computing the angle $\overline{\theta}$ and projecting it back onto the line

$$\begin{aligned} \overline{\theta} &= \text{atan2}\left(\overline{\sigma}, \overline{\tau}\right) + \pi \\ x_{\text{COM}} &= L\frac{\overline{\theta}}{2\pi}. \end{aligned} \tag{3.2.8}$$

The improbable case of exactly evenly spaced particles along a dimension results in $(\overline{\sigma}, \overline{\tau})$ sitting at the centre of the circle and $\text{atan2}\left(\overline{\sigma}, \overline{\tau}\right)$ being undefined.

A further subtlety is that using neighbour lists of particles within cutoff radii, as is routinely done in MD to calculate potentials and forces, cannot be applied for computation of the COM. All positions of the same-electron particles must be known simultaneously, not just those within the cutoff radius, which is memory intensive. The same applies to computing the COM velocity.

The COM velocity of the $a$th electron for $N_{ppe}$ SPH particles of the same mass is simply $\mathbf{V}_a = \sum_i^{N_{ppe}} \mathbf{v}_i^a / N_{ppe}$. Omitting the exact description, a Nosé-Hoover style thermostat [151] can then be applied to the centre of mass velocities $\{\mathbf{V}_a\}$ to achieve a target distribution. The required velocity scaling $\eta_a$ for each electron COM velocity is applied via a uniform scaling to SPH members of each electron

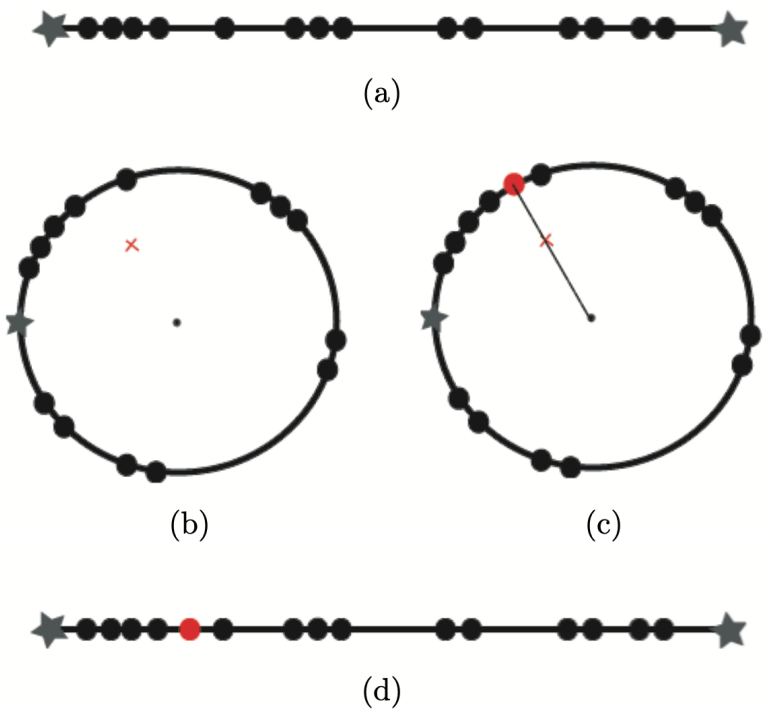


Figure 3.4: Reproduced from [149]. Coordinates along a single dimension of length $L$ (a) are projected onto a circle (b) using the angle $\theta_i = 2\pi x_i/L$, with each point on the circle defined by two new coordinates $\sigma_i = \cos(\theta_i)$ and $\tau_i = \sin(\theta_i)$. The average of the $\sigma$ and $\tau$ values then defines the COM of the circle (red cross in b), which is then used to compute the angle of the COM (c) and project it back onto the line (d).

$$\eta_a \mathbf{V}_a = \sum_i^{N_{ppe}} \eta_a \cdot \frac{\mathbf{v}_i^a}{N_{ppe}}. \tag{3.2.9}$$

In LAMMPS, same-electron SPH particles are defined by assigning their continuous `id` values into blocks of length $N_{ppe}$.

### *3.2.3 Conservation*

Following the equations of motion for SPH particles described in the previous sections, I demonstrate their conservative properties. First, I begin by comparing various forms for the density derivatives used in the Bohm pressure tensor on a simple periodic box interacting only through the Bohm pressure force. I list the mass densities here, but

note that number densities are required in the Bohm expressions, simply related by $n = \rho/m_e$ with $m_e$ the electron mass in the appropriate unit. It is well established in the SPH method that naïve derivatives of Equation (2.1.3), as in Equation (2.1.4), are not the most accurate [88, 94, 95], in fact various alternative expressions exist for SPH derivatives. The forms and associated names investigated here are, for the first derivative

$$\text{basic: } \partial_x \rho_i = \sum_j m_j \, \partial_x W_{ij}(h_i) \tag{3.2.10}$$

$$\text{F2: } \partial_x \rho_i = \sum_j m_j \left(1 - \frac{\rho_i}{\rho_j}\right) \partial_x W_{ij}(h_i), \tag{3.2.11}$$

where 'F2' is borrowed as a label from Ref. [88], and for the second derivative

$$\text{basic: } \partial_{xy} \rho_i = \sum_j m_j \, \partial_{xy} W_{ij}(h_i) \tag{3.2.12}$$

$$\text{Mocz: } \partial_{xy} \rho_i = \sum_j m_j \left(1 - \frac{\rho_i}{\rho_j}\right) \partial_{xy} W_{ij}(h_i) \tag{3.2.13}$$

$$\text{D1: } \partial_{xy} \rho_i = \sum_j \frac{m_j}{\rho_j} \, \partial_y \rho_j \, \partial_x W_{ij}(h_i) \tag{3.2.14}$$

$$\text{D2: } \partial_{xy} \rho_i = \sum_j \frac{m_j}{\rho_j} \left(\partial_y \rho_j - \partial_y \rho_i\right) \partial_x W_{ij}(h_i), \tag{3.2.15}$$

where 'Mocz' corresponds to the form used in Ref. [101]. It is worth noting that the second derivatives D1 and D2 are not symmetric $\partial_{xy} \neq \partial_{yx}$, meaning the Bohm pressure tensor is no longer symmetric. They also require an additional loop over neighbours to compute the first derivative terms.

The eight combinations of derivatives are used on an 1024 SPH particle system, with total mass equivalent to 16 electrons in a cubic box of length $7.11\,\mathrm{a_B}$, the same

Table 3.1: Energy conservation of derivative combinations for a test Bohm-only simulation with periodic boundary conditions, sorted from best to worst, all to 3sf.

| $\nabla\rho$ | $\nabla^2\rho$ | $\int \Delta E_{tot}^2 dt$ [Ha$^2$ fs] |
|---|---|---|
| **F2** | **Mocz** | $\mathbf{1.01 \cdot 10^{-11}}$ |
| basic | Mocz | $2.05 \cdot 10^{-11}$ |
| F2 | basic | $9.62 \cdot 10^{-11}$ |
| basic | basic | $1.29 \cdot 10^{-10}$ |
| F2 | D2 | $1.13 \cdot 10^{-6}$ |
| F2 | D1 | $2.89 \cdot 10^{-6}$ |
| basic | D2 | 0.000136 |
| basic | D1 | 0.000191 |

density as the electrons in the warm dense hydrogen system in the following chapter. All simulations are initialised identically from rest with timestep 0.1 as, $\zeta = 1.3$ and cutoff $3\,\overline{h}$. The energy outputs are plotted in Figure 3.5. All combinations of derivatives conserve momentum to machine precision, as shown in Figure 3.6. The drift of the total energy $\Delta E_{tot}$ is less uniform. The change in total energy for the Bohm-only system is calculated according to

$$\Delta E_{tot}(t+\delta t) = E_K(t+\delta t) + \Delta U_B - E_K(t), \tag{3.2.16}$$

where $E_K =$ is the total kinetic energy of the SPH particles and where the total change in Bohm energy $\Delta U_B$ is computed via

$$\Delta U_B = \sum_a m_a \delta t \, \frac{du_{B_a}}{dt} \tag{3.2.17}$$

with $\frac{du_{B_a}}{dt}$ calculated according to equation (2.2.35) using velocity and position data at $t + \delta t$.

A summary of the energy conservation is given in Table 3.1, where the drift of the total energy is squared and summed over the 5 fs duration of the simulation as an indicator of energy conservation.

The combination of F2 for the first and Mocz for the second derivative is optimal for

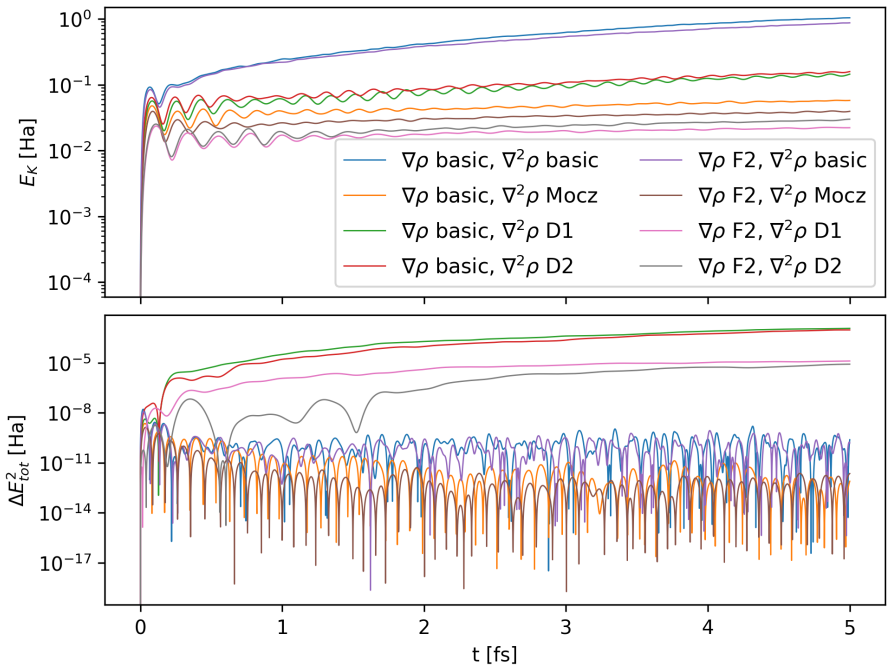


Figure 3.5: Kinetic energy and the square of the total energy drift of a Bohm-only system with different derivative combinations.

computing the Bohm pressure tensor in a system with periodic boundary conditions, having the best energy conservation. This combination is adopted for all simulations performed in Chapters 4 and 5. Derivatives D1 and D2 have surprisingly poor conservation, which I expect is related to the breaking of symmetry in the second derivatives.

Next I investigate the conservation of the Coulomb SPH force expressions on a one-component-plasma (OCP) system. The periodic box has 5248 particles, corresponding to 82 electrons, with length 12.261 $a_B$, once again at the same density of electrons in the warm dense hydrogen system of the following chapter. All particles interact with one another via long-range Coulomb potentials. For comparison, both the SPH Coulomb interaction and the standard point Coulomb interaction are examined, with identical initialisations of a random particle arrangement. Specifically, the standard LAMMPS interaction coul/long is used for the points. The simulations are run with a timestep of 0.5 as, $\zeta = 1.3$, a real-space cutoff of $r_c = 5.5\,a_B$, and a Ewald parameter equal to $3/r_c$. The energy outputs are shown in Figure 3.7. SPH Coulomb conserves momentum to

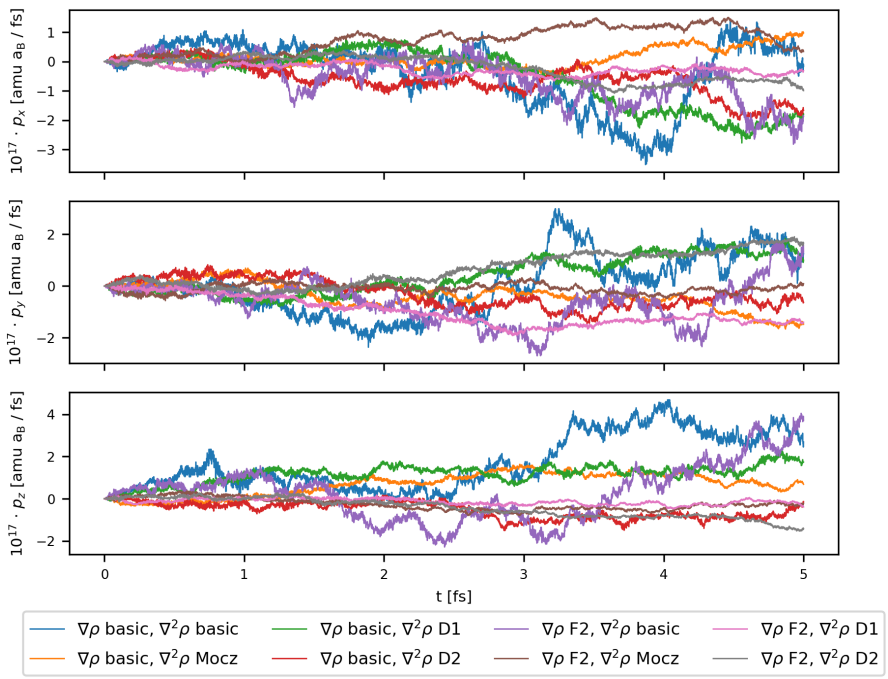


Figure 3.6: Total momentum components of a Bohm-only system with different derivative combinations. Y axes multiplied by a factor of $10^{17}$ for ease of labelling (very small fluctuations).

machine precision as shown in Figure 3.8. After an initial jump, the total energy of the SPH Coulomb system oscillates with similar amplitude to that of the point Coulomb (with the oscillation likely due to a sparsity of k vectors in the Ewald computation), and the kinetic energy of the SPH Coulomb system equilibrates at a lower value than the point Coulomb as expected. This validates the conservation of the novel SPH Coulomb interaction.

Finally, I examine the conservation of the warm dense hydrogen system with all force interactions enabled, as investigated in the following chapter with 512 protons and 16384 SPH electron particles (spin unpolarised hydrogen at a density of $n_e = 3.006\,\mathrm{g/cm^3}$ and temperature $T = 21.54\,\mathrm{eV}$). I select the strongest confinement potential ($g = 8.16\,\mathrm{Ha/a_B^2}$) as the limiting conservation case, since weaker confinement potentials have better energy conservation. In contrast to the previous test systems, this system includes ions and is initialised at finite temperature. The simulations are run with a timestep of 0.25 as, $\zeta = 1.3$, a Coulomb real-space cutoff of $r_c = 4.81\,\mathrm{a_B}$, a

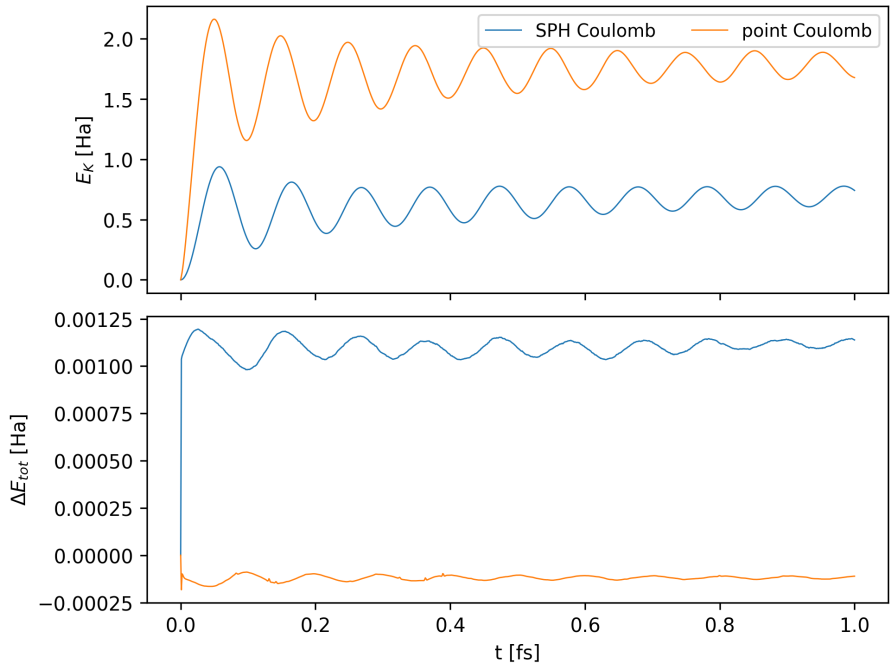


Figure 3.7: Kinetic energy and change in the total energy of a test OCP Coulomb system comparing standard point and SPH Coulomb interactions.

Ewald parameter equal to $3/r_c$, a Bohm cutoff of 3.47 $a_B$, and a Pauli (Minoo) potential cutoff of 3.37 $a_B$. Following the Bohm-only analysis above, F2 is used for computation of the first derivative of the density in the Bohm pressure tensor, and Mocz the second.

To check the exact energy conservation, the Bohm internal energy must be calculated according to Equation (2.2.35) with the position and velocity data at the same point in the timestep and not with the half-timestep separation of leapfrog integrators. In the current implementation, this requires an additional computation of the Bohm pressure tensor per timestep, slowing the simulation by approximately 25 %. The simulation includes three stages: a first of 50 fs in which the protons are placed into an NVT ensemble by a thermostat and the SPH particles are in an NVE ensemble to allow them to converge on their centres of mass. A second of 250 fs in which the protons remain in NVT and the SPH particles are acted upon by a centre of mass thermostat to bring their centre of mass velocities into the appropriate distribution, and then a release of both protons and SPH particles into an overall NVE ensemble at 300 fs,

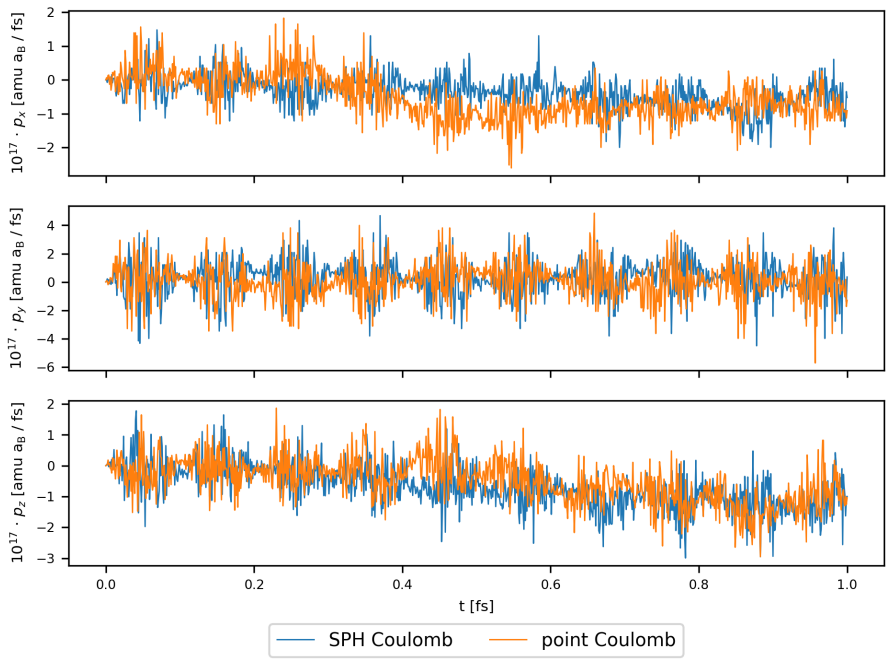


Figure 3.8: Total momentum components of a test OCP Coulomb system comparing standard point and SPH Coulomb interactions. Y axes multiplied by a factor of $10^{17}$ for ease of labelling (very small fluctuations).

persisting for roughly 160 fs in this case, sufficient to observe drift in the total energy. The energy and momentum outputs are plotted in Figures 3.9 and 3.10 respectively. The total energy has a marginal drift of 1.34 Ha/fs, which for the collection time of 700 fs used in the next chapter to compute dynamics, corresponds to 938 Ha, less than 5 % of the total kinetic energy at release into full NVE (18819.735 Ha). This drift is trivially suppressed with a smaller timestep, but this incurs further computation and I deemed $< 5\,\%$ tolerable for accurate dynamics without further computational expense.

The total momentum of the warm dense hydrogen system is plotted after release into NVE at approximately 300 fs, whereupon the components oscillate with amplitudes of order $10^{-12}$ amu $a_B$/fs about the finite values caused by the thermostats. While significantly larger than the oscillations observed for the test Bohm and Coulomb systems, I note that this system has far more mass and is initialised at a finite temperature. Indeed, taking the thermal velocity of a proton at these conditions, I calculate that the thermal momentum in its direction of travel is (to 3sf)

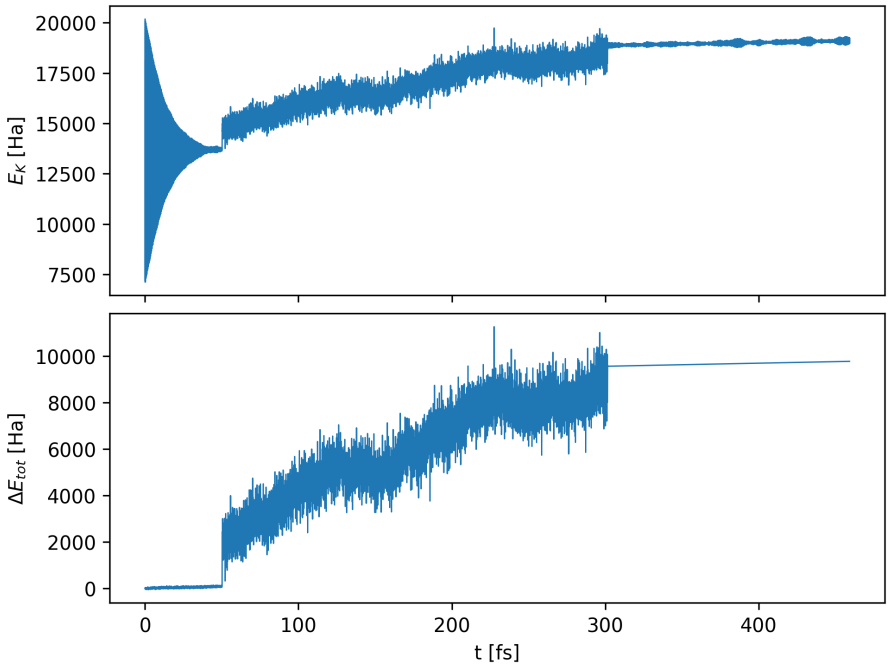


Figure 3.9: Kinetic energy and change in the total energy of the warm dense hydrogen system with confinement $g = 8.16\,\mathrm{Ha/a_B^2}$.

$$p_{th} = mv_{th} = \sqrt{3k_B T m} = 1.50\,\mathrm{amu\,a_B/fs}. \tag{3.2.18}$$

This is $10^{12}$ times greater than the scale of oscillation, so the momentum is well conserved when all force interactions are enabled.

### *3.2.4 Parallel Scaling*

The bespoke SPH module, utilising the LAMMPS framework, has excellent parallel scaling. My module is separate to a previous implementation in LAMMPS (see Ref. [152]). The scaling tests are conducted for the warm dense hydrogen system investigated in Chapter 4, at a density of $n_e = 3.006\,\mathrm{g/cm^3}$ and temperature $T = 21.54\,\mathrm{eV}$, with 512 protons and 16384 SPH electron particles ($N_{ppe} = 32$). All interactions are computed (Coulomb, Bohm, Pauli and Confinement). The strong parallel scaling is demonstrated

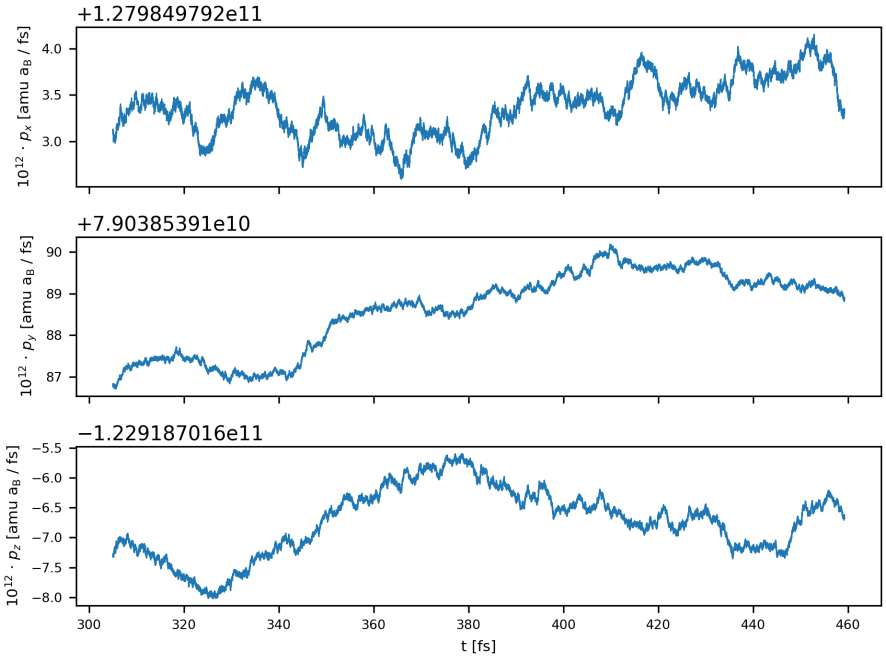


Figure 3.10: Total momentum components of the warm dense hydrogen system with confinement $g = 8.16\,\mathrm{Ha/a_B^2}$ after release into NVE. Y axes multiplied by a factor of $10^{12}$ for ease of labelling.

in the top inset of Figure 3.11. The scaling contributions from modules within LAMMPS are also plotted alongside the total time. Perfect scaling is given by the relation

$$t_N = t_1/N, \tag{3.2.19}$$

where $t_N$ is the wall time per timestep for a simulation running on $N$ processors. Figure 3.11 shows that in the example warm dense hydrogen system, the compute time only begins to notably diverge from perfect scaling at around 100 CPU. This divergence is also dependent on the system size and cutoff radii values for the various force interactions, and hence can be tuned with variation of these parameters.

The weak scaling of Bohm SPH is presented in the bottom inset of Figure 3.11, with very consistent compute times observed across the number of processors. The weak scaling is computed with the resolution kept constant and the box size increased. The SPH Bohm pressure force and Coulomb forces comprise the majority of the 'Pair'

compute time, while the calculation of the densities, dynamic kernel scale lengths and centres of mass comprise almost all the 'Modify' compute time. Using an alternative kernel with better compact support and therefore smaller neighbour cutoffs, such as the cubic spline [82], would speed up future implementations.

## 3.3 Validation

In the ground state tests in this section and the following, a finite difference term in the first order density derivative, Equation (3.2.11), was not used because it was found to cause greater instability than a naïve derivative, as in Equation (3.2.10), in these particular cases that have a free boundary. SPH schemes can require special care to handle free boundaries [72]. In general I am interested in continuous plasmas simulated with periodic boundary conditions, which do not have a free boundary, so have not made such adjustments. A larger value of $\zeta = 1.3 \cdot \sqrt{2}$ has instead been used in both to promote stability as it comfortably ensures the relation $h > \Delta$. Overall, Bohm SPH demonstrates good agreement on two single particle problems which have analytical solutions: the ground states of the 3d quantum harmonic oscillator and the hydrogen atom.

### *3.3.1 Quantum Harmonic Oscillator*

To validate the Bohm expressions used, I first investigate a reduced system interacting only via the Bohm pressure force and a quadratic confining potential, the quantum harmonic oscillator. Unlike in many-electron simulations the confining potential here is centred on a fixed coordinate rather than the centre of mass of the SPH distribution. Running simulations with $N_S = 256$ SPH particles and dynamic kernel scale lengths I damp the system to zero temperature to achieve the ground state. In this single wave-function example, the Bohm equations are exact. Taking a Gaussian probability density

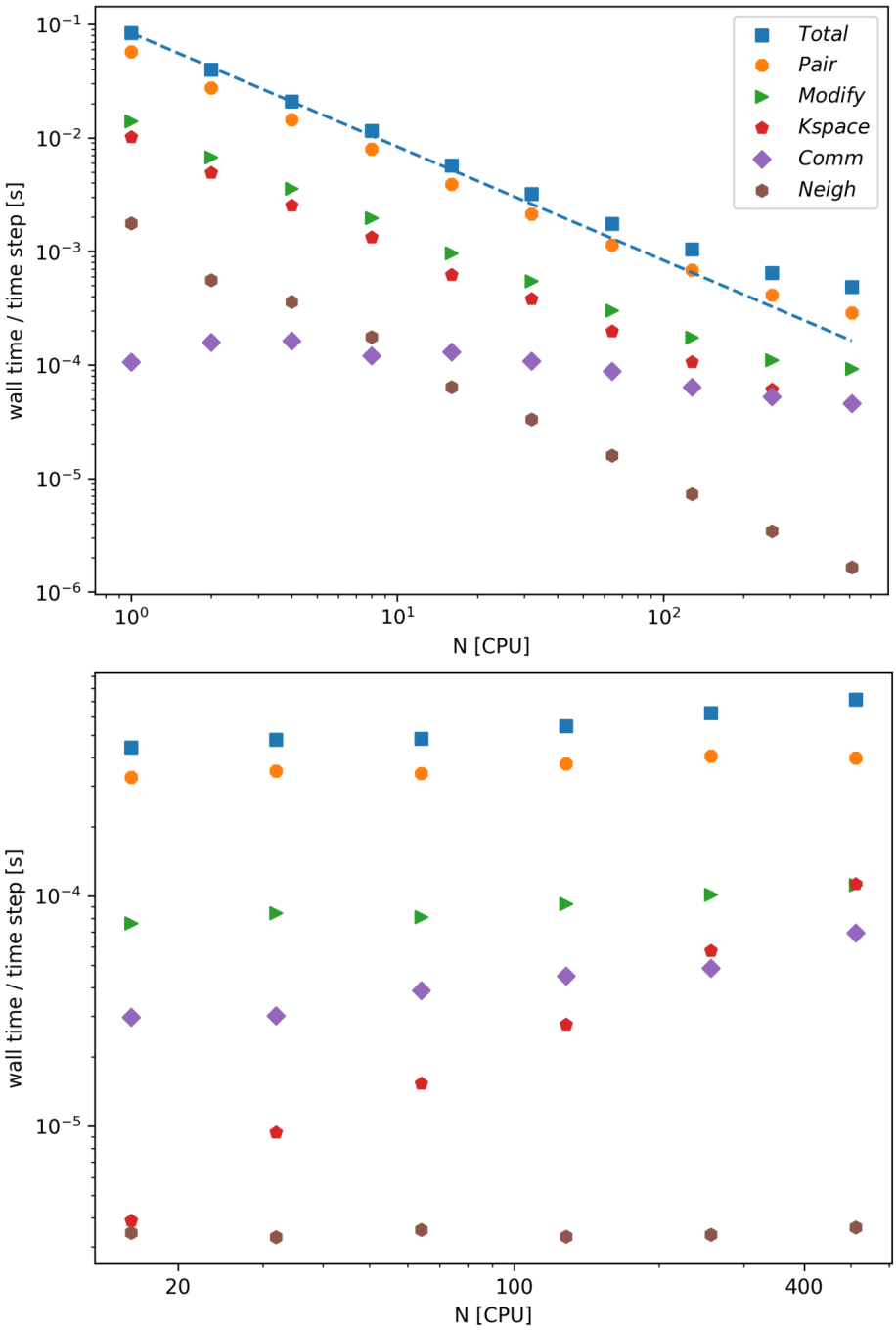


Figure 3.11: Strong (top) scaling of a warm dense hydrogen system with 512 protons and 16384 SPH particles, and weak (bottom) scaling of the same warm dense hydrogen system with a resolution of $N_{ppe} = 32$ SPH particles per electron. Includes runtime statistics for individual LAMMPS modules. Perfect scaling is indicated by the dashed blue line. The individual module contributions are: the real space force computation in 'Pair', the dynamic electron width and centre of mass computation within 'Modify', Ewald Coulomb calculation in 'Kspace', neighbour list construction in 'Neigh', and communication times between MPI processors in 'Comm'.

profile as shown below, equating the expectation energies of the confining potential and the Bohm potential gives a simple relation between the confining potential strength $g$ and the wavefunction width $H$. The Gaussian ground state density distribution is

$$n(\mathbf{r}) = |\psi(\mathbf{r})|^2 = \frac{1}{(\pi H^2)^{3/2}} \exp\Big( - \frac{|\mathbf{r}|^2}{H^2} \Big) = G(\mathbf{r}, H), \tag{3.3.1}$$

where $H$ is the overall width of the wavefunction and $G$ refers to the Gaussian function. Here the confining potential is centred on the origin, and has expectation energy

$$\begin{aligned} \langle V_c \rangle &= \int d\mathbf{r}\, g r^2 |\psi(\mathbf{r})|^2 \\ &= \int 4\pi r^2 dr \frac{g r^2}{\left(\pi H^2\right)^{3/2}} \exp\left( -\frac{r^2}{H^2} \right) \\ &= \left( \frac{4\pi g}{\left(\pi H^2\right)^{3/2}} \right) \frac{3H^5}{8} (\pi)^{1/2} \\ &= \frac{3H^2 g}{2}. \end{aligned} \tag{3.3.2}$$

The expectation of the Bohm potential for a Gaussian wavefunction is straightforward but lengthier to compute

$$\langle V_B \rangle = \int d\mathbf{r} \left( -\frac{\hbar^2}{2m} \frac{\nabla^2 \sqrt{n(\mathbf{r})}}{\sqrt{n(\mathbf{r})}} \right) |\psi(\mathbf{r})|^2. \tag{3.3.3}$$

Expanding the Bohm potential as

$$-\frac{\hbar^2}{2m} \frac{\nabla^2 \sqrt{n}}{\sqrt{n}} = -\frac{\hbar^2}{8m} \left[ \frac{2\nabla^2 n}{n} - \left( \frac{\nabla n}{n} \right)^2 \right], \tag{3.3.4}$$

and computing the gradients of the Gaussian density

$$\begin{aligned}\nabla n &= -\frac{2\mathbf{r}}{H^2}\,G \\ \nabla^2 n &= \left[\frac{4|\mathbf{r}|^2}{H^4} - \frac{6}{H^2}\right] G,\end{aligned} \tag{3.3.5}$$

then

$$-\frac{\hbar^2}{2m}\frac{\nabla^2\sqrt{n}}{\sqrt{n}} = \frac{\hbar^2}{2mH^2}\left(3 - \frac{r^2}{H^2}\right). \tag{3.3.6}$$

Computing the integral in Equation (3.3.3) with this expression for the Bohm potential then yields after some algebra

$$\langle V_B \rangle = \frac{3\hbar^2}{4mH^2}. \tag{3.3.7}$$

Now we have two simple expressions for the expectation of the confinement and Bohm potentials, equating them gives the relation

$$H = \left(\frac{\hbar^2}{2mg}\right)^{1/4}. \tag{3.3.8}$$

After damping, the particles are released into an NVE ensemble to check the stability of the solution and the density distributions are fitted to a Gaussian. The fitted Gaussian widths from four simulations sampling different confining strengths $g$ are summarised in Figure 3.12, and show excellent agreement with the expected relation Equation (3.3.8), validating the implementation of the Bohm pressure tensor.

The stability of the dynamic kernel relation Equation (2.1.13) with respect to $\zeta$ is tested on the QHO. The results plotted in Figure 3.12 are all for $\zeta = 1.3 \cdot \sqrt{2}$ and with one iteration of the fixed point calculator. Now, the final width of QHO ground states achieved when reducing $\zeta$ are shown (also with one iteration of fixed point calculator) in

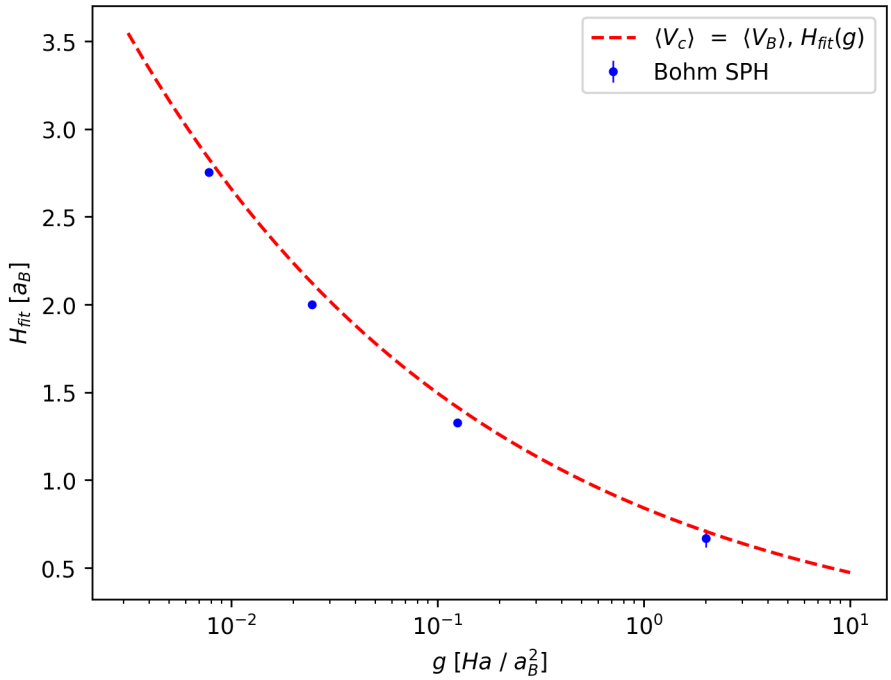


Figure 3.12: Fitted Gaussian width outputs from reduced Bohm SPH simulations of a damped quantum harmonic oscillator compared to expected relation (Equation (3.3.8)). Plotted error is the standard deviation of the width calculations of the final 200 time steps (50 as) of each run, only visible in the strongest confinement point.

Figure 3.13. We can see that the final fitted ground state width only begins to diverge from the target value when $\zeta \leq 0.8$. While only a static analysis, this indicates that smaller values than the typical $\zeta = 1.3$ requirement may be tolerable in future Bohm SPH work, which is desirable given resolution requirements (see Section 3.1.3 above) and also for computational cost. Smaller kernel scale lengths have more compact support meaning cutoff radii are reduced.

### *3.3.2 Hydrogen Ground State*

Now to further test the implementation of the Bohm and the Coulomb forces on the ground state of hydrogen. For this single electron system, I do not include the Pauli interaction, Coulomb interactions between particles (other than dynamic kernel interactions via the electron - ion interaction), and the confining potential. While the ground state of the harmonic oscillator is straightforward to solve in Bohm SPH, be-

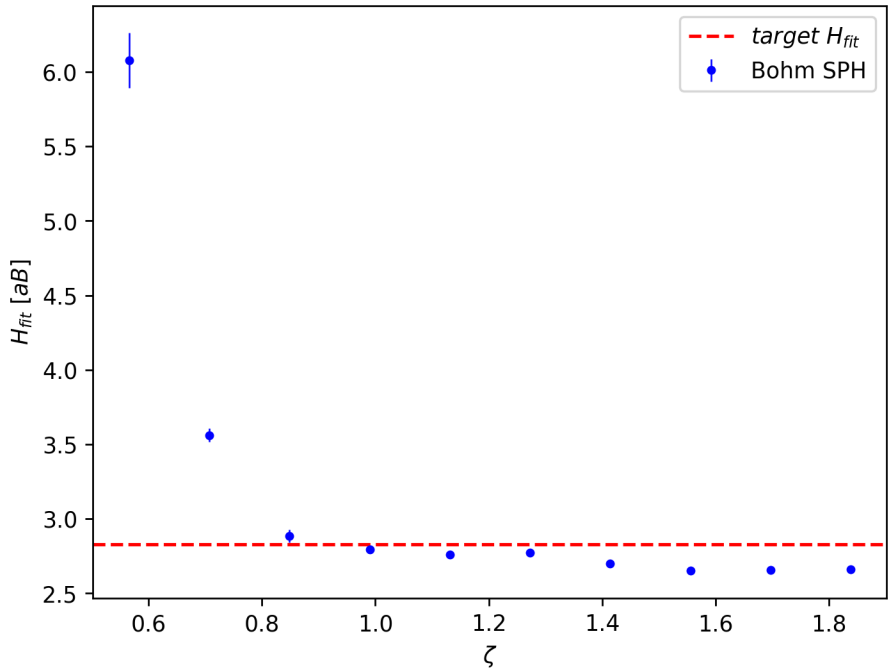


Figure 3.13: Fitted Gaussian width outputs from reduced Bohm SPH simulations of a damped quantum harmonic oscillator with $g = 0.00781\,\mathrm{Ha/a_B^2}$ scanning the $\zeta$ value of the dynamic kernel scale length Equation (2.1.13). Plotted error is the standard deviation of the width calculations of the final 200 time steps (50 as) of each run.

ing relatively insensitive to initial distribution and damping strength, the ground state of hydrogen is more challenging. It is difficult to fully suppress the kinetic energy of the SPH particles. I attribute this to the strength of attraction between electron SPH particles and the central ion, written in Equation (3.1.3), being not only a function of radial separation, but also of the dynamic kernel scale lengths which are dependent on the many-body distribution.

SPH particles were first initialised on a simple cubic grid around the proton. In the following $N_S = 1237$ SPH particles were used. Comparisons of different starting grids used $N_S = 1237$ SPH particles. The cubic grid terminates within spherical limits to give the system rough initial spherical symmetry. Three initial cutoffs were investigated, $r_0 = 2.0\,\mathrm{a_B}$, $2.5\,\mathrm{a_B}$, and $3.0\,\mathrm{a_B}$, with lattice parameters of $0.3\,\mathrm{a_B}$, $0.375\,\mathrm{a_B}$, and $0.45\,\mathrm{a_B}$ respectively. The particles were randomly displaced off the grid points prior to running by $0.005\,\mathrm{a_B}$ to break the exact symmetry. The simulations were all then run with a time

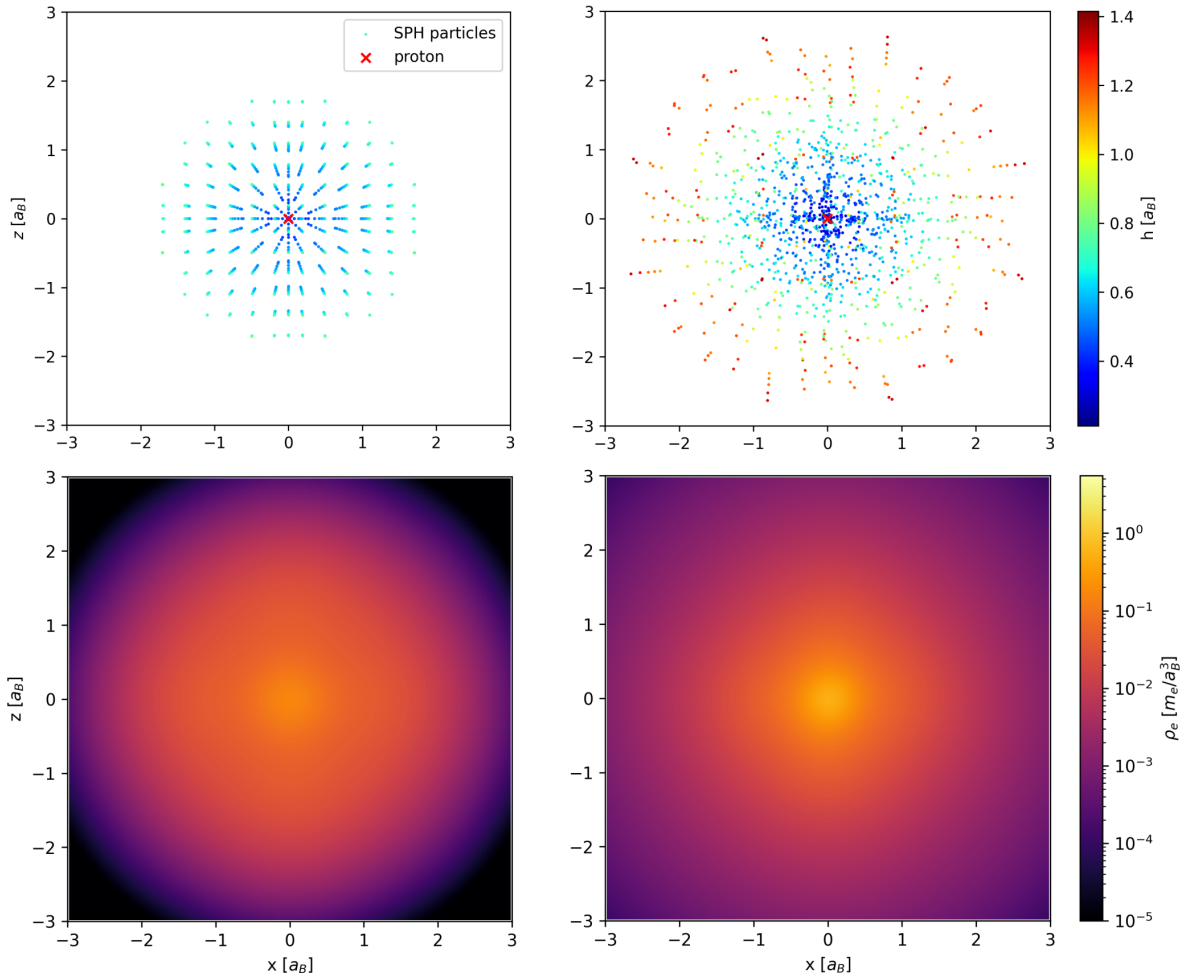


Figure 3.14: Initial (left) and final ($t = 1.44\,\mathrm{fs}$, right) SPH particle distributions for damped Bohm SPH simulation of the hydrogen ground state with particles initialised within a spherical cutoff $r_0 = 2.0\,\mathrm{a_B}$ of the proton. SPH particle position and width ($h$) information (top) and continuous density profile of cross section at $y = 0$ (bottom).

step of $5\times10^{-4}$ as with a frictional damping term applied, of strength $1\times10^{-4}\,\mathrm{Ha{\cdot}fs/a_B^2}$. The initial and final distribution of SPH particles (projected in two dimensions) is shown in Figure 3.14 for initial cutoff radius $r_0 = 2.0\,\mathrm{a_B}$. An additional simulation with $N_S = 2469$ on a grid with lattice parameter of $0.3\,\mathrm{a_B}$ which terminated within a radius of $r = 2.5\,\mathrm{a_B}$ was also run to demonstrate convergence of the density and overall energy toward the exact wavefunction solution.

The evolution of the separate Bohm SPH runs ($r_0 = 2.0, 2.5, 3.0\,\mathrm{a_B}$) is shown in Figure 3.15 which plots the instantaneous Bohm and Coulomb energies from the SPH

particle distributions over time. This figure compellingly shows the separate runs all converging on similar Bohm and Coulomb energies close to the true values. The average distribution of SPH particles across all three runs in the final 5 snapshots, from $t = 1.36$ to 1.44 fs at 0.02 fs intervals, is plotted in Figure 3.16. There is reasonable agreement with the exact distribution, although the SPH distribution is slightly overdense close to the proton and underdense further away. The energy averages and errors are given in Table 3.2. For reference, the best fit (energy) of a single Gaussian to the hydrogen 1s density distribution, of width $H = 1.33\,a_B$, is also included in the table. Neglecting for simplicity the non-diagonal terms in the Bohm pressure tensor, the Bohm potential is calculated for each SPH particle via the equation

$$V_{B_a} = -\frac{\hbar^2}{8m_e}\left[\frac{2\nabla^2 n_a}{n_a} - \frac{(\nabla n_a)^2}{n_a^2}\right] \tag{3.3.9}$$

where as discussed the first derivatives of the density are computed without the finite difference term as in Equation (3.2.10), and the second as in Equation (3.2.13). The total Bohm energy of the system is then $\langle V_{\text{Bohm}}\rangle = \sum_a V_{B_a}/N_S$.

Bohm SPH returns return a total energy value closer to the exact 1s expectation of -0.5 Hartree than the best fit single Gaussian, with the Coulomb contribution notably more accurate. The convergence of the separate Bohm SPH runs toward a shared ground state, with a more accurate overall energy than the best fit single Gaussian case, validates the treatment of the Coulomb interaction which applies the SPH kernels as real charge distributions.

## 3.4 Conclusions

The complete Bohm SPH model has been introduced. This includes the electrostatic Coulomb interaction and a symmetry potential from QSP to capture Pauli repulsion, as

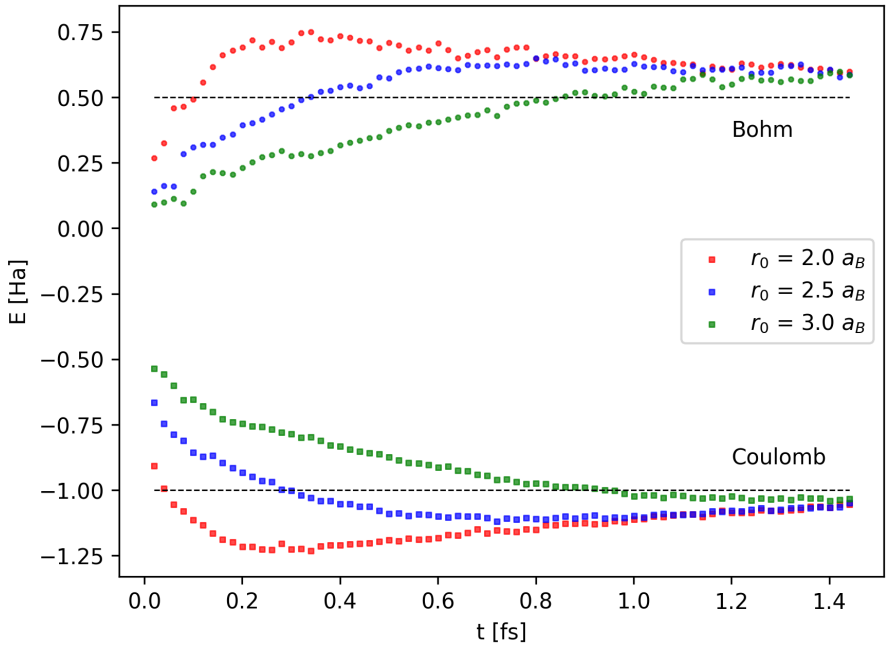


Figure 3.15: Energy evolution of damped Bohm SPH simulations of hydrogen ground state with initial radii $r_0 = 2.0$ (red), 2.5 (blue), and 3.0 (green) $a_B$, computed from single snapshots of the SPH particle distributions at 0.02 fs intervals. Squares indicate Coulomb energy, and circles the Bohm potential, computed and summed over all particles according to Equation (3.3.9). Horizontal lines are the exact 1s wavefunction energies, which all simulations tend toward over time.

well as a confinement potential invoked to mitigate the problem of additional translational degrees of freedom. The practicalities of implementing the Many-Fermion Bohm potential were also assessed, and while there is no semantic problem with its implementation into SPH, the requirement of achieving equivalent spatial resolution to the QHD Bohm treatment costs a factor $N_e^2$ more compute time, which I have deemed prohibitive for this project.

Two computational details were also explored, the dynamic kernel scale-length iterator and calculation of the centre of mass compatible with PBC. The entire code, utilising the well-distributed LAMMPS structure, has excellent parallel scaling. Conservative properties of the individual Bohm and Coulomb SPH implementations were demonstrated. Particular comparison of the energy conservation of the Bohm-only system with different density derivative forms suggests that the optimal pairing is 'F2'

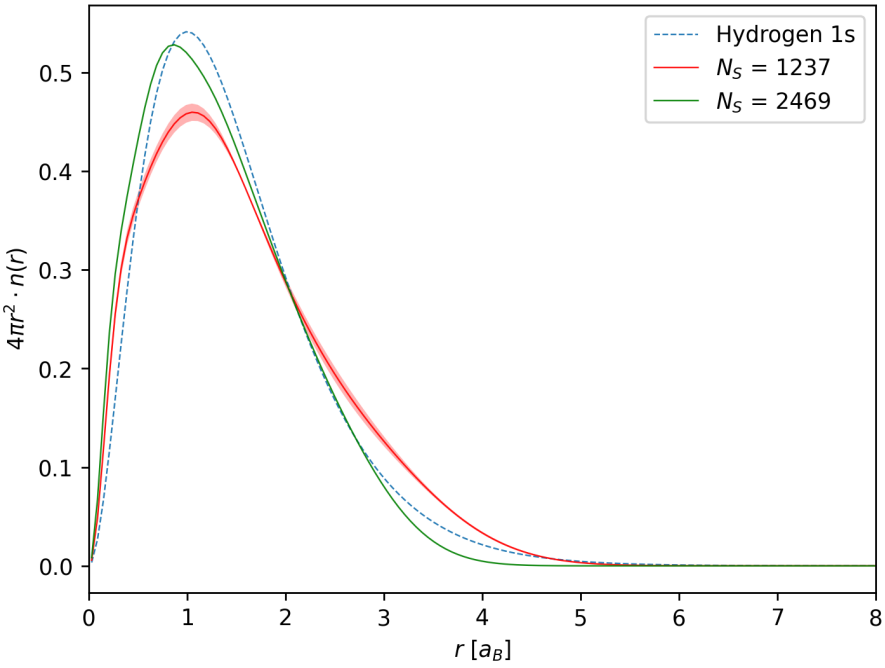


Figure 3.16: Density distribution from average of final five snapshots of damped $N_S = 1237$ and $N_S = 2469$ particle Bohm SPH simulations of the hydrogen ground state, compared to exact hydrogen 1s distribution. $N_S = 1237$ average includes values from all three different initial radii, whereas $N_S = 2469$ from a single run with initial radius $2.5\,\mathrm{a_B}$. The average total energy of the $N_S = 1237$ results is $\langle V_{\mathrm{Total}} \rangle = -0.46 \pm 0.01\,\mathrm{Ha}$, and for $N_S = 2469$ $\langle V_{\mathrm{Total}} \rangle = -0.513 \pm 0.003\,\mathrm{Ha}$. Central solid line is mean, with error bar $\pm$ the standard deviation.

for the first and 'Mocz' for the second. The conservation of the full model as used to simulate warm dense hydrogen was also shown. Subsequently, the correct operation of the SPH and Bohm modules were demonstrated in analysis of the three dimensional quantum harmonic oscillator ground state, recovering the relation of the confinement strength and width computed by equating the expectation energies of the Bohm and confinement potentials. A further investigation varying $\zeta$ when computing the ground state indicates that smaller values than $\zeta = 1.3$ could be applied in future work, reducing cutoff radii lengths and hence computational cost, as well as improving the screening length requirements $\overline{h} < \lambda_S$.

The treatment of the Coulomb interaction that uses the SPH density distribution as the real charge distribution is novel, and the exact Coulomb force on SPH particles with dynamic lengths was derived. While its validity is proved with compelling re-

Table 3.2: Comparison of potential energies of the hydrogen ground state computed via damped Bohm SPH simulations with $N_S = 1237$, to the best fit single Gaussian (SG) with width H = 1.33 $a_B$ and to the exact energy contributions of a 1s wavefunction. Average values of Bohm SPH potentials are calculated from all three runs over 5 snapshots from $t = 1.36$ to 1.44 fs at 0.02 fs intervals, error given is the standard deviation. All energy values in Hartree units, SG values given to 3 significant figures.

| Type | $\langle V_{\text{Coul}} \rangle$ | $\langle V_{\text{Bohm}} \rangle$ | $\langle V_{\text{Total}} \rangle$ |
|---|---|---|---|
| Bohm SPH | -1.05 ± 0.01 | 0.59 ± 0.01 | -0.46 ± 0.01 |
| SG 1.33 $a_B$ | -0.849 | 0.424 | -0.424 |
| 1s | -1.0 | 0.5 | -0.5 |

sults for the hydrogen ground state, in the context of non-adiabatic plasma simulations it introduces additional degrees of freedom whose thermal affect must be addressed. Two solutions were suggested, namely maintaining separate ionic and electronic temperatures, or introducing a confining potential and operating on the electron centres of mass. These approaches are both investigated in the following chapter for a warm dense hydrogen system. The effective Coulomb coupling between SPH particles was also considered, particularly relevant to the thermalisation investigations of Chapter 5.

# Chapter 4

# Investigations of Warm Dense Hydrogen

Now Bohm SPH is applied on a physical system of interest, warm dense hydrogen, yielding various static and dynamic structural properties. The system investigated is spin unpolarised hydrogen at a density of $n_e = 3.006\,\mathrm{g/cm^3}$ and temperature $T = 21.54\,\mathrm{eV}$, corresponding to $\theta = 1.32$ and $r_s = 1.75\,\mathrm{a_B}$. For these parameters the ion coupling is $\Gamma_i = (Ze)^2/(4\pi\epsilon_0 a_i k_B T) = 0.72$ with $a_i = r_s$, the electron plasma period is $0.203\,\mathrm{fs}$, and the expected screening length of the plasma is $\lambda_S = 1.29\,\mathrm{a_B}$. With $\theta$, $\Gamma_i \approx 1$, this system is firmly in the warm dense regime. Bohm SPH is benchmarked against anisotropic WPMD (see Ref. [58]) at these conditions. Further warm dense hydrogen structure data at similar, though not identical, conditions can be found in Ref.s [71, 18].

Three iterations of the model are presented, 'simple', 'two-temperature', and 'confinement'. In the first 'simple' case, the resolution of the SPH density is scanned by increasing the SPH particles per electron $N_{ppe}$, while keeping the overall temperature fixed. I see how the ion static structure results converge to $\lim_{k\to 0} S_{ii}(k) = 0$, as occurs in one-component-plasmas, but not in ordinary fluids [153] where one expects a finite

value, and how the ion acoustic dispersion flattens as $N_{ppe}$ increases. Furthermore, the plasmon does not converge as $N_{ppe}$ increases, instead dispersing. For any systems where one models ions as point particles while allowing them to exchange energy with the SPH particles, these problems are unavoidable. Instead - considering the thermal effect of the additional SPH particles (as discussed in 3.1.4) motivates use of either the two-temperature or confinement approaches.

The two-temperature approach yields much more compelling ion structure results. Here, separate Nosé-Hoover thermostats are applied to the ions and to the SPH particles, maintaining the ions at $T_i = T$, and SPH particles at $T_i = T/N_{ppe}$. To constrain the effect of the thermostats, the respective thermostat damping parameters are scanned. The ion static structure corresponds well with the WPMD calculation, as does the dispersion of the ion acoustic wave (IAW). A disadvantage of this two-temperature approach is that isolating the free-electron motion is made impractical by the separate thermostats.

Finally, as well as ionic structure, the confinement approach enables calculation of free electron dynamics by computing the trajectories of the electron centres of mass, avoiding the problems above. Here, the strength of confinement potential determines the length scales that can be reliably investigated. The plasmon data from the strongest confinement case corresponds well with WPMD in the collective regime.

The simple and two-temperature data originates from an earlier simulation campaign which used a larger value of $\zeta = 1.3 \cdot \sqrt{2}$. While a smaller value of $\zeta = 1.3$ (applied in the confinement approach) improves the resolution of the electronic component, it does not address either the fundamental problems of unphysical screening and dispersion in the simple approach, nor the inability to isolate free-electron dynamics in the two-temperature approach.

## 4.1 Simple Bohm SPH

Here the resolution of the electronic density is increased by sequentially increasing the SPH particles per electron $N_{ppe}$, while keeping the overall temperature fixed. Although the confinement potential is not enabled, there are no Coulomb or Pauli potentials defined between SPH particles assigned to the same electron. Simulations were run with $N_{ppe} = 1, 2, 4, 8, 16, 32$, corresponding to average kernel lengths $\overline{h} =$ 5.19, 4.12, 3.27, 2.59, 2.06, 1.63 $\mathrm{a_B}$ (all to 3sf). While none of these satisfy the desirable $\overline{h} < \lambda_S$ condition, their outputs are instructive for understanding the thermal problem of the additional degrees of freedom and how it might be addressed.

Simulations were all run with a timestep of 0.2 as and 1024 protons in a periodic box. The density was determined using $m_{iter} = 1$ iteration of the density-width solver (as described in Section 3.2.1). Both the protons and the SPH particles were thermalised under a global Nosé-Hoover thermostat for the first 150 fs, then released into a microcanonical ensemble for 600 fs in which the trajectories were recorded. The Pauli potential cutoff was fixed at 3.743 $\mathrm{a_B}$ for all $N_{ppe}$ values, while the Coulomb cutoff scaled as $r_c = 1.2 \cdot 2\,\mathrm{FWHM}(\overline{h})$ (and Ewald parameter $3/r_c$), and Bohm cutoff of $3.18\,\overline{h}$.

In the following results I assumed isotropic systems such that the structure factors depend only on the magnitude of the wavenumber $k = |\mathbf{k}|$. The ion static structures are plotted in Figure 4.1. In the cases with $N_{ppe} = 1, 2$, an unphysical minimum is observable in $S_{ii}(k)$. This has also been observed in cases with an unphysical attractive part in the ion-ion interaction, such as when applying the Singwi-Tosi-Land-Sjölander approximation for electronic screening at large ion couplings and low temperature in Ref. [154]. One might hope that by increasing $N_{ppe}$ the electronic screening of the ions becomes more accurate and that $\lim_{k\to 0} S_{ii}(k)$ converges on a finite value, as in the compelling output provided by WPMD. Instead for $N_{ppe} > 2$, the ion static structure tends to $\lim_{k\to 0} S_{ii}(k) = 0$, as expected for an OCP, but not for a plasma with the electronic component modelled explicitly. It is apparent that the SPH particles are

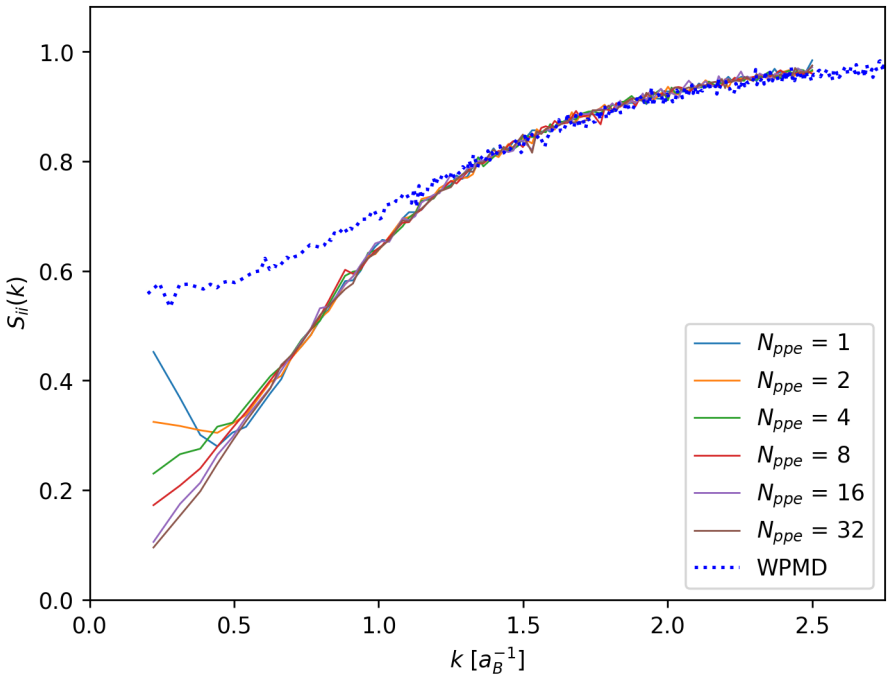


Figure 4.1: Ionic structure factors from simple Bohm SPH model scanning resolutions $N_{ppe}$ while keeping the temperature fixed, compared to reference calculation from WPMD.

not screening the protons correctly in this simple Bohm SPH approach, but provide a homogeneous background at high resolution. The electronic static structure factors are computed from the individual SPH particles trajectories and are plotted in Figure 4.2. They confirm the homogeneity, with $S_{ee}(k)$ becoming flattened as $N_{ppe}$ increases, and $\lim_{k\to 0} S_{ee}(k) = 1$.

The dispersion of the IAW is plotted in Figure 4.3. The dispersion flattens as $N_{ppe}$ increases, with the agreement between simple Bohm SPH and WPMD poor once again.

Finally, the free electron dynamic structure factor is plotted in Figure 4.4 for the first $k = 0.3125\,\mathrm{a_B^{-1}}$ mode, corresponding to $\alpha = 3.512$, where $\alpha = 1/k\lambda_S$. Here the dispersion and broadening of the plasmon with increasing resolution is very pronounced. This is a manifestation of the thermal velocity of the SPH particles scaling as $v_{th} \propto \sqrt{N_{ppe}}$, as discussed in Section 3.1.4. Clearly, keeping the SPH temperature fixed across different $N_{ppe}$ values and not applying confinement potentials is not a satisfactory approach.

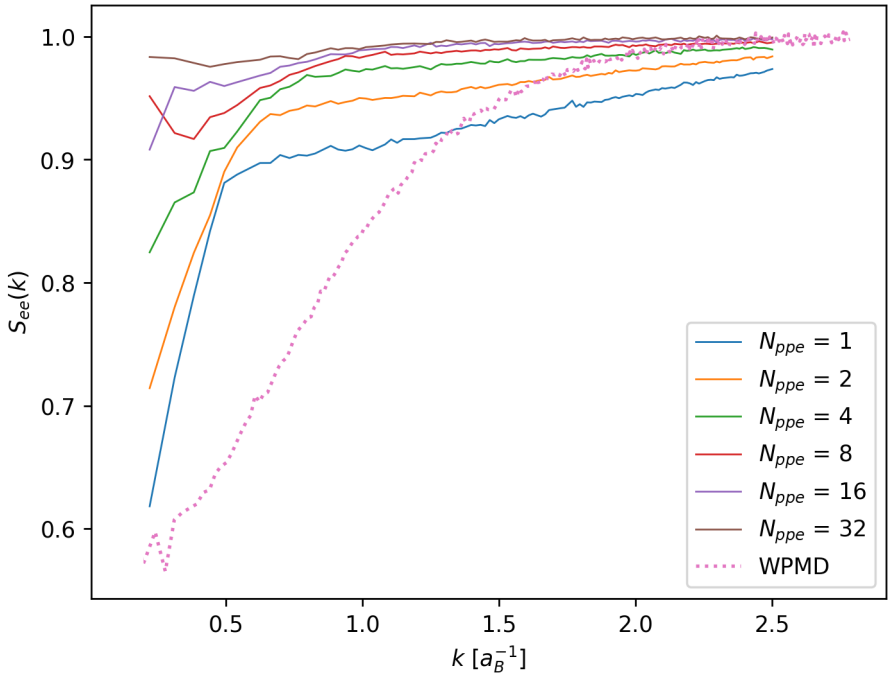


Figure 4.2: Simple Bohm SPH: electronic structure factors from scanning resolutions $N_{ppe}$ while keeping the temperature fixed, compared to reference calculation from WPMD.

## 4.2 Two-Temperature Bohm SPH

To ensure the SPH particles move at the thermal velocity of whole electrons, the protons and the SPH particles were kept at separate temperatures $T$ and $T/N_{ppe}$ respectively. This is equivalent to keeping the total amount of thermal energy in the system constant with $N_{ppe}$. Simulations using this approach had 512 protons with $N_{ppe} = 32$ in a periodic box. All had a timestep of 0.25 as, a Coulomb cutoff of $r_c = 6.3\,\mathrm{a_B}$ (and Ewald parameter $3/r_c$), Bohm cutoff of $4.62\,\mathrm{a_B}$, Pauli cutoff of $3.743\,\mathrm{a_B}$, and $m_{iter} = 1$. The damping parameters, corresponding to the timescales over which the thermostats relax the temperature to the target value (as per the LAMMPS documentation [150]), were scanned for the separate proton and SPH thermostats. Fixing the proton damping parameter at 25 as, the SPH damping parameter sampled values 6.25, 12.5, 25, 50, 100 as. Another scan was performed fixing the SPH damping parameter to 25 as, and scanning the proton damping across the same values.

The ion static structures are plotted in Figure 4.5, which all have excellent agreement

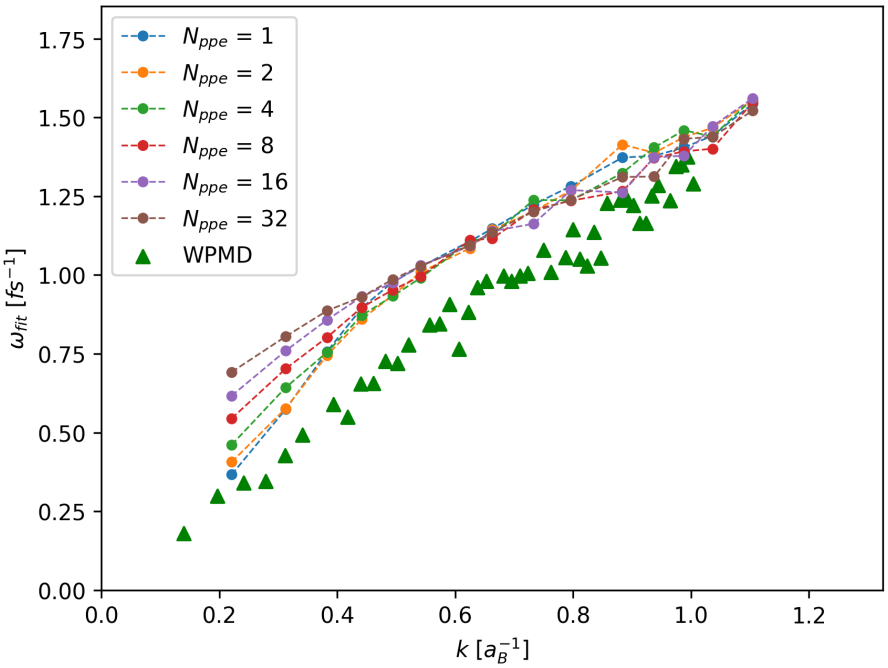


Figure 4.3: Simple Bohm SPH: frequencies of fitted progressive modes for the ion dynamic structure factors scanning resolutions $N_{ppe}$ while keeping the temperature fixed, compared to reference calculation from WPMD.

with the WPMD result regardless of thermostat parameters. The dispersion of the IAW is plotted in Figure 4.6, also showing strong agreement with the WPMD result with no clear dependence on thermostat parameter. Electronic structure in this two-temperature approach is much poorer and not included here. In particular, extraction of the free electron motion, as discussed in Section 1.5, is very difficult. With $N_{ppe} = 32$ the protons and SPH particles are strongly out of equilibrium at temperatures $T$ and $T/N_{ppe}$ respectively. This undermines isolation of the free electron motion. Extracting the free electron dynamic structure factor $S^0_{ee}(\mathbf{k}, \omega)$, as in Figure 1.2, relies on the total electron intermediate scattering function having a clear slow mode corresponding to the screening clouds following the protons. This slow mode is disrupted when there are strong thermostats keeping the protons and SPH particles at separate temperatures. In general, extraction of $S^0_{ee}(\mathbf{k}, \omega)$ requires both protons and SPH particles to be in the same NVE ensemble, which is done in the simple and confinement approaches when collecting trajectory data.

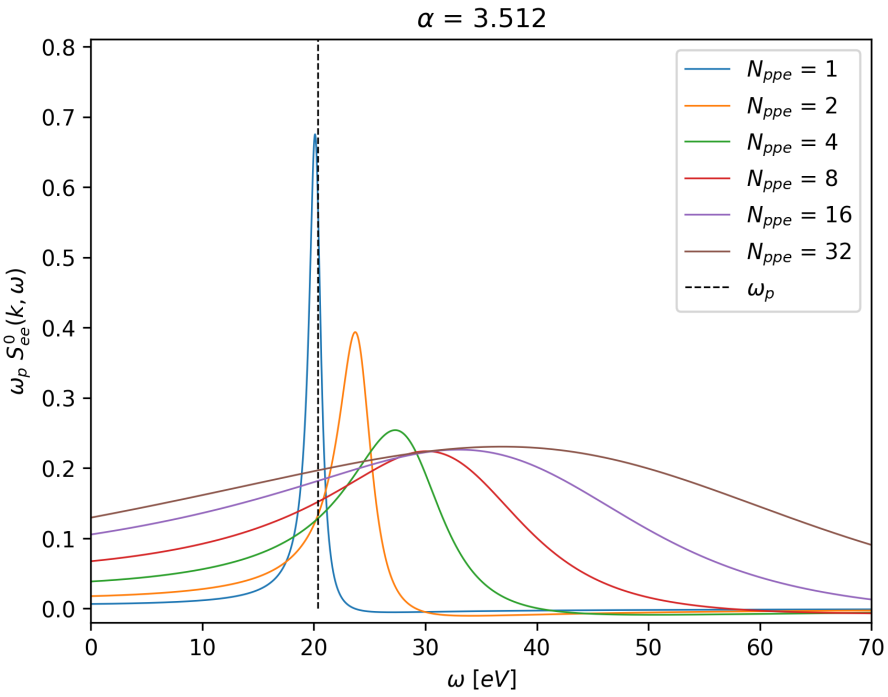


Figure 4.4: Simple Bohm SPH: free electron dynamic structure factors scanning resolutions $N_{ppe}$ while keeping the temperature fixed.

The strong agreement of the ion results with WPMD in the two-temperature scheme is encouraging. It suggests that by forcing the system to have the correct total translational thermal energy (with 'correct' meaning the amount expected for a system of whole ions and electrons), the ion motion and structure becomes accurate. Although in this two-temperature approach the electronic data was essentially unusable.

## 4.3 Confinement Bohm SPH

Finally, I applied a confinement potential to SPH particles assigned to the same electron, and operated on their well defined centre of mass with an appropriate thermostat to bring their centre of mass velocities into equilibrium with the point ions. This enabled the simultaneous extraction of ionic and electronic structure data. Considering this approach the best for non-adiabatic investigation of warm dense matter with Bohm SPH, I will examine its outputs in more detail. The system was evolved with a time

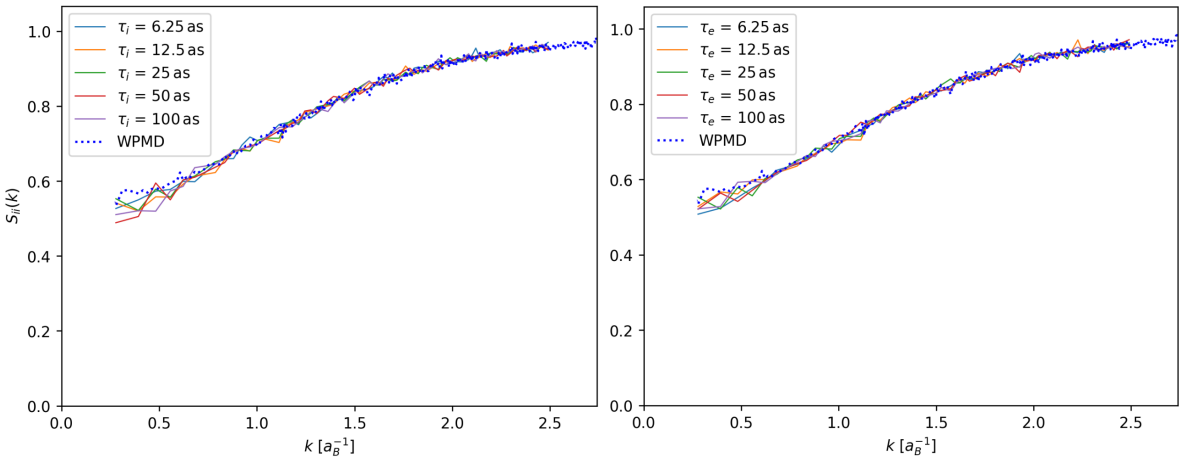


Figure 4.5: Two-Temperature Bohm SPH: Ionic structure factors scanning thermostat damping parameters $\tau$, compared to reference calculation from WPMD. When scanning different values of ion (proton) damping $\tau_i$, the SPH (electron) damping is set to $\tau_e = 25\,\text{as}$, and vice versa.

step of 0.25 as in all simulations and contains 512 protons and 16384 SPH particles ($N_{ppe} = 32$). The Coulomb real-space cutoff was $r_c = 4.81\,\text{a}_\text{B}$, with Ewald parameter equal to $3/r_c$, the Bohm cutoff $3.47\,\text{a}_\text{B}$, and the Pauli (Minoo) potential cutoff $3.37\,\text{a}_\text{B}$, and $m_{iter} = 2$. Importantly, with the kernel widths dynamically updated according to Equation (2.1.13) with $\zeta = 1.3$, the average SPH kernel width $\overline{h} = 1.16\,\text{a}_\text{B}$ is less than the expected screening length $\lambda_S = 1.29\,\text{a}_\text{B}$.

The following outputs have three stages. A first stage of 50 fs when a thermostat was applied to the ions and the SPH particles remained in NVE to allow them to converge on their centres of mass. A second stage of 250 fs when a thermostat was also applied to the electron centres of mass to bring them to the same temperature as the ions. Finally the third stage of 0.7 ps where both the ions and the SPH particles were released into a microcanonical ensemble in which trajectory data is collected. I note that for my target density and temperature the exact Fermi-Dirac kinetic energy distribution differs only mildly from a Maxwellian, so I have allowed the electrons to relax into a Maxwellian distribution for the collection of trajectory data. For more strongly degenerate systems, a bespoke thermostat can be used to push the electronic

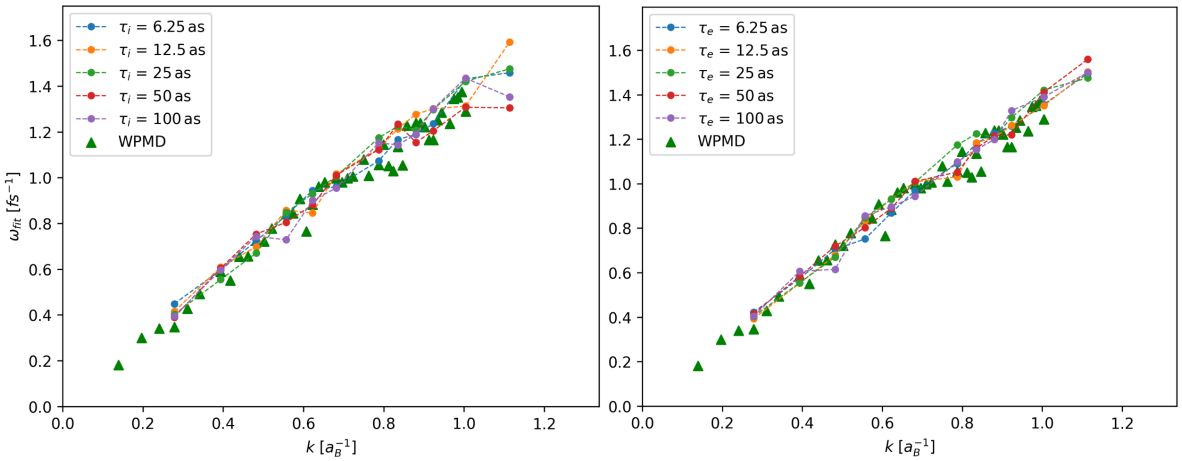


Figure 4.6: Two-Temperature Bohm SPH: Frequencies of fitted progressive modes for the ion dynamic structure factors scanning thermostat damping parameters $\tau$, compared to reference calculation from WPMD. When scanning different values of ion (proton) damping $\tau_i$, the SPH (electron) damping is set to $\tau_e = 25\,\text{as}$, and vice versa.

component into an appropriate Fermi-Dirac distribution, as in [25].

An example of the thermalisation of the system is shown in Figure 4.7, with the ion temperature $T_i$ and the electron temperature $T_e$ plotted. For free SPH particles the electronic temperature is simply given by Equation (3.1.23). This temperature does not apply when using confining potentials. In this case, the temperature must be defined with respect to the centre of mass velocities of the electrons $\mathbf{V}_i = \sum_j^{N_{ppe}} \mathbf{v}_j / N_{ppe}$

$$\sum_i^{N_e} \frac{1}{2} m_e \langle \mathbf{V}_i^2 \rangle = \frac{3}{2} N_e k_B T_e. \tag{4.3.1}$$

Once equilibriated, the trajectories of the electron centres of mass were then collected to compute the electronic structure.

Values of $g$ were scanned producing electron sizes between roughly 3.0 and 2.0 $a_B$ (as shown in Figure 4.10), calculated by fitting a single Gaussian to the density distribution of SPH particles belonging to the same electron. An example of this fitting procedure is in Figure 4.8. This demonstrates that while localised, the electron shape itself is not exactly Gaussian.

At each confinement strength two runs were performed with different initial condi-

tions to average the results. The drift in total energy over the 0.7 ps of data collection when under the strongest confinement is less than 5% of the total kinetic energy at release into NVE, as shown previously in Section 3.2.3. Distributions of the fitted electron sizes across the confinement strengths are given in Figure 4.9, plotted alongside the kernel length distributions recorded at the same time. The plateauing trend of mean fitted widths in Figure 4.10 suggests substantial further contraction of the electron width may not be feasible with my selected SPH parameters. A larger value of $N_{ppe}$ may allow investigation of smaller electron widths by decreasing the average particle kernel length.

Histograms of the SPH kernel lengths and fitted electron widths, recorded at the end of the simulations, are plotted in Figure 4.9. They show how as the confinement strength increases, the SPH kernel length distribution slightly broadens, creating denser and sparser regions in the electron density. Figure 4.10 also shows how the fitted electron width distributions narrow, and their means shift to smaller sizes.

The results are benchmarked against outputs from anisotropic WPMD, in which the root mean square width of the Gaussian wavepackets was $H_W = 1.44\,\mathrm{a_B}$. Figure 4.11 demonstrates that the Bohm SPH static structure calculations have improved agreement with the WPMD calculation as the strength of confinement is increased. Unsurprisingly, the ion-electron and electron-electron structure factors are more sensitive to the strength of confinement. Even in the case of the weakest confinement however, the ion structure agrees reasonably well with WPMD, and the extrapolated electron and ion structure values at $S(k = 0)$, related to the compressibility [155, 156], are similar to the WPMD estimates. I ascribe the difference in static structure observed between Bohm SPH and WPMD to be primarily due to different electron sizes, which strongly affect the screening of the plasma. The strongest confinement case of Bohm SPH achieves an average electron Gaussian width of $H_{fit} = 2.02\,\mathrm{a_B}$, still larger than the root mean squared width of the WPMD output of $H_W = 1.44\,\mathrm{a_B}$.

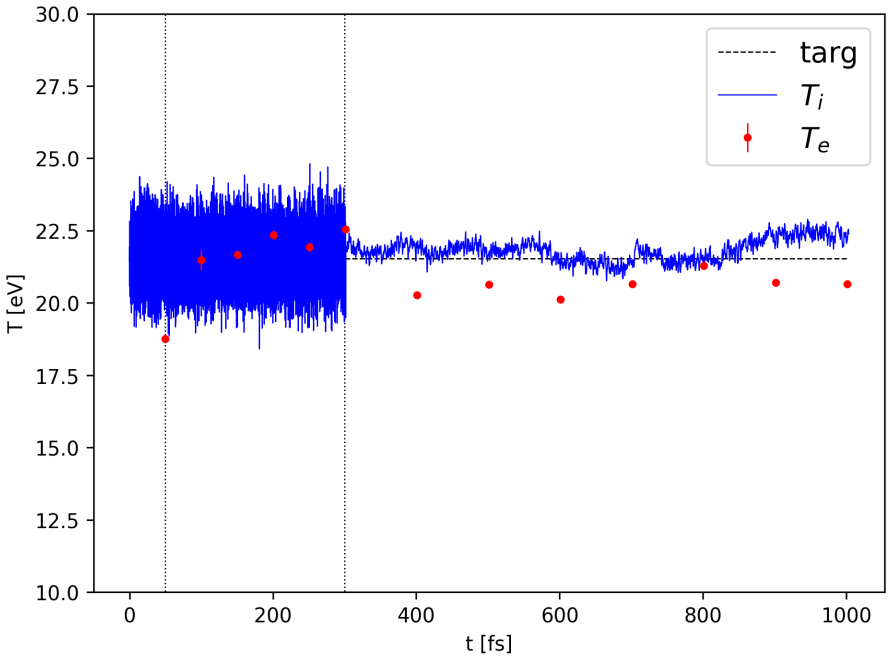


Figure 4.7: Temperature data for run of strongest confinement ($g = 8.16\,\mathrm{Ha/a_B^2}$) of Bohm SPH. 'targ' corresponds to the target temperature, $T_i$ the ion temperature, and $T_e$ the electron temperature as defined by Equation (4.3.1). Error bars on $T_e$ are the standard deviation of the temperature computed at 25 individual timesteps separated by 1.0 as each (centre point is mean). The simulation stage boundaries are indicated by the vertical dotted lines.

The ion dispersion is relatively insensitive to the confinement strength, as shown in Figure 4.12. Figure 4.13 examines the ion dynamic structure factor, with comparison of the strongest and weakest confinement Bohm SPH simulations. This shows good agreement between Bohm SPH and WPMD, with some differences in the strength of the diffusive mode. The strength of the confinement potential and subsequently the electron size seemingly controls the strength of ion diffusive mode, with the strongest confinement potential having notably larger values of $S_{ii}(k, \omega = 0)$ than the weakest confinement potential.

For reference, the ionic acoustic dispersion $\omega = c_{S_i} k$ is also included in Figure 4.13 using an expression for $c_{S_i}$ derived for classical, low density plasmas

$$c_{S_i} = \sqrt{\frac{\gamma_e Z k_\mathrm{B} T_e + \gamma_i k_\mathrm{B} T_i}{m_i}}, \tag{4.3.2}$$

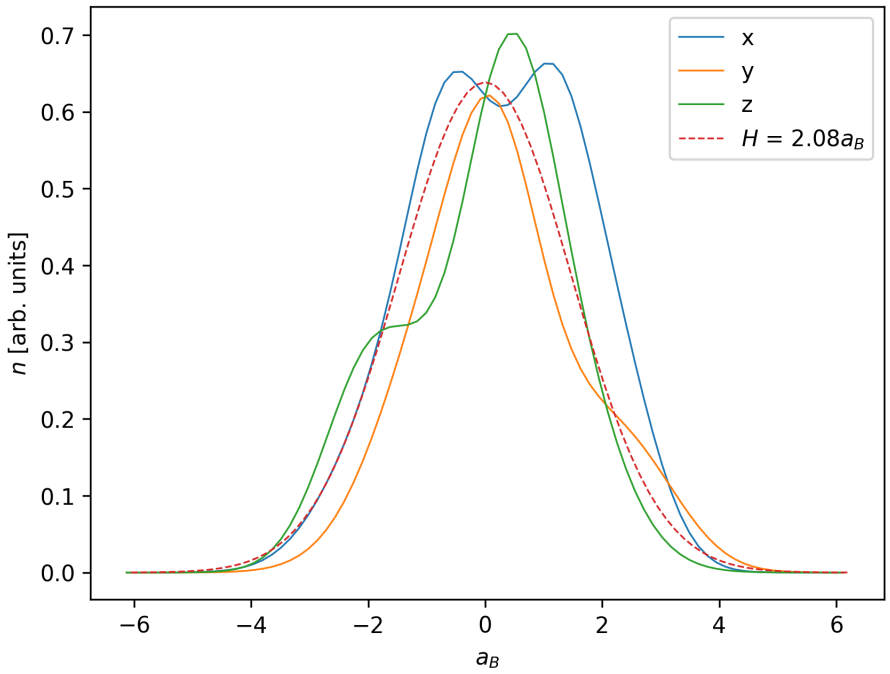


Figure 4.8: Single Gaussian best fit to the density profile of an example electron under the strongest confinement ($g = 8.16\,\mathrm{Ha/a_B^2}$). Fitted by minimising against the electron density profiles along the principal x, y, and z directions.

where I set $T_e = T_i$, and $\gamma_{e,i}$ represent the ratio of specific heat capacities for the electrons and ions respectively: $\gamma_i = 3$ for one dimensional propagation, and $\gamma_e = 1$ assuming the electrons are isothermal on the time scale of the ion acoustic waves. This yields a sound speed of $c_{S_i} = 1.49\,\mathrm{a_B/fs}$. The computed ionic dispersion for the warm dense hydrogen data agrees well at small k with this classical expression.

The electron dynamic structure was computed using the centre of mass coordinates of each electron recorded over the simulation, and treating them as point particles. The outputs are plotted in Figure 4.14, and they compare favourably with outputs from WPMD, computed via direct Fourier transform of the truncated intermediate scattering function and which apply the same detailed balance correction. In the electron dynamic structure factors the effect of confinement is more prominent. Both the position of the plasmon peak and the value of $S^0_{ee}(k, \omega = 0)$ agree more closely with WPMD in the strongest confined case than weakest. The weakest confined case consistently underpredicts the plasmon frequency and overestimates $S^0_{ee}(k, \omega = 0)$, associated with

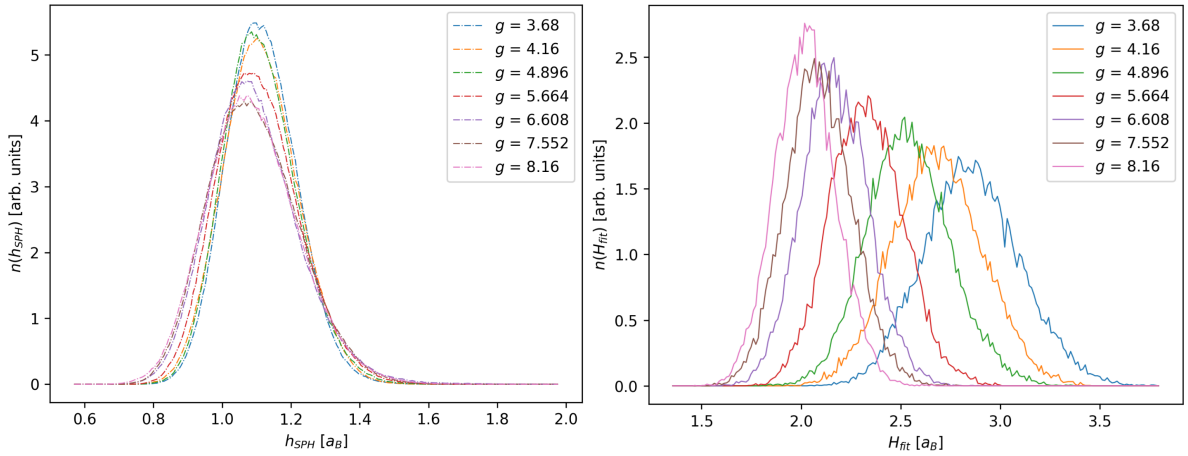


Figure 4.9: SPH kernel length (left) and fitted electron width (right) distributions for all confinement strengths of target hydrogen system ($\theta = 1.32$ and $r_s = 1.75\,\mathrm{a_B}$). Histogram data collected over 25 separate timesteps (separated by 1 as each) at end of simulations. Data averaged over two simulations for each confinement. Confinement strength $g$ units are $\mathrm{Ha/a_B^2}$. Electron fitted width mean and standard deviation data plotted in Figure 4.10.

the electron diffusivity, when comparing to WPMD. Figure 4.15 shows how the plasmon frequency and its width trend with increasing confinement strength. In the collective $\alpha > 1$ regime, the values reasonably converge by the strongest confinement case. The more pronounced dependence on confinement strength at shorter length scales (smaller $\alpha$) shows how the achieved electron size determines the resolvable electron dynamics.

The electron dynamic structure outputs are also compared to the predictions of the Random Phase Approximation [157, 156] which neglects exchange and correlation effects, strictly applying when the interparticle interactions are weak. I note that the numerical outputs for the plasmon (strong confinement Bohm SPH and WPMD) at the investigated k modes predict a lower peak frequency and a slightly broader plasmon. A similar effect has been reported in previous work investigating the impact of exchange-correlation as well as ion collisions on plasmon dispersion [158, 159]. Improvements to the RPA prediction can of course be made by including local field corrections [160, 161], omitted here.

An explicit visualisation of the electron density provides an instructive comparison of the three Bohm SPH approaches explored here. From the example cross sections

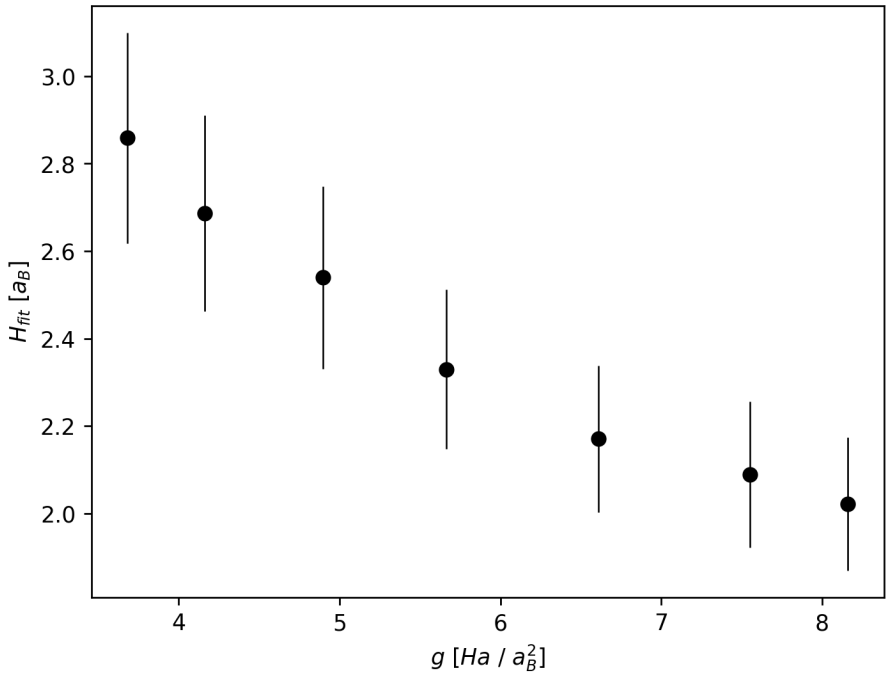


Figure 4.10: Mean fitted electron widths (± standard deviation) for all confinement strengths of target hydrogen system ($\theta = 1.32$ and $r_s = 1.75\,\mathrm{a_B}$). Histogram data collected over 25 separate timesteps (separated by 1 as each) at end of simulations. Data averaged over two simulations for each confinement.

plotted in Figure 4.19 at the end of this chapter, the simple approach is clearly the most homogeneous, with increasing contrast in the two-temperature and confinement approaches.

### *4.3.1 Scaling the Bohm Potential*

An additional interesting analysis is to adjust the strength of the Bohm interaction via the $\gamma$ parameter discussed in the QHD derivation of Section 2.2.2. For all the data thus far, I have applied a value of $\gamma = 1$. Now I repeat the strongest confinement Bohm SPH simulations with a value of $\gamma = 1/9$ and examine the difference in output. In Figure 4.16 the static structure factors are compared and there is a small discrepancy for values of $k$ between roughly 0.5 and 1.0, with the $\gamma = 1/9$ structure factors slightly larger than the $\gamma = 1$ for all species. This implies greater correlation at these separations when the Bohm interaction is reduced in strength. For reference, the inverse screening

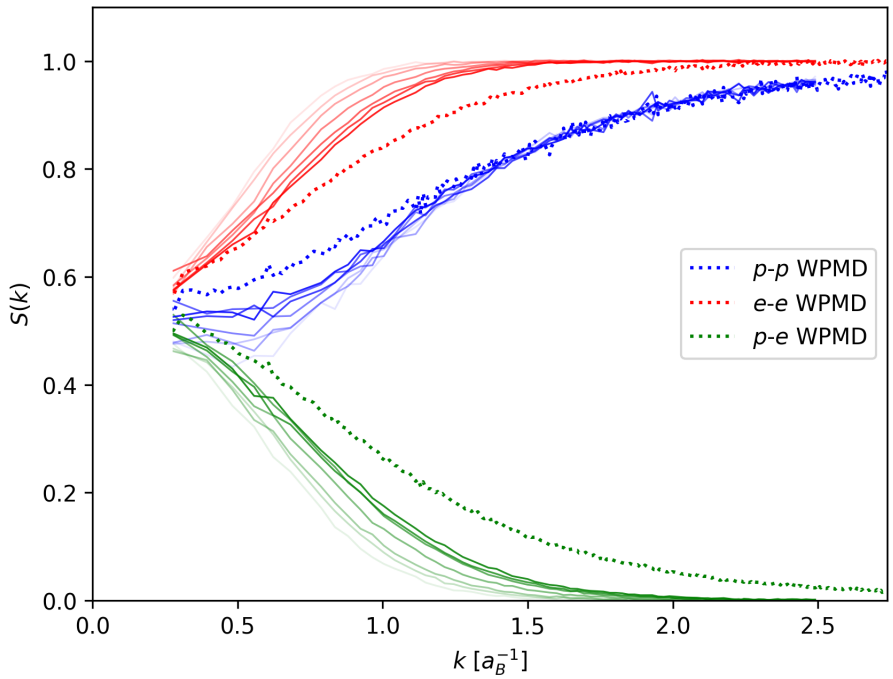


Figure 4.11: Confinement Bohm SPH: proton - proton and electron - electron static structure factors compared to reference calculation from WPMD. Values of $g$ as in Figure 4.10 with smallest confinement in lightest shade to strongest confinement in darkest.

length is $k = 1/\lambda_S = 0.78\,\mathrm{a_B^{-1}}$ for this system. To make a thorough comparison at smaller $k$ values would require larger simulation boxes and better convergence, although the current data suggests that both $\gamma$ cases approach the same $S(k = 0)$ limit. The IAW dispersion, plotted in Figure 4.17, is relatively unaffected by varying the Bohm interaction strength.

The fitted frequencies of the progressive mode in the free electron intermediate scattering function are plotted in Figure 4.18 out to approximately $\alpha = 1$. The frequencies of the $\gamma = 1$ case are larger than the $\gamma = 1/9$, with the difference generally growing with the value of $k$. The outputs are compared to the 'improved dispersion relation' (IDR) derived in [162] for a weakly degenerate plasma ($\theta \approx 1$)

$$\omega_{IDR}^2 = \omega_p^2 + \frac{3k_B T_e}{m_e} k^2 (1 + 0.088 n_e \Lambda_e^3) + \left(\frac{\hbar k^2}{2m_e}\right)^2, \tag{4.3.3}$$

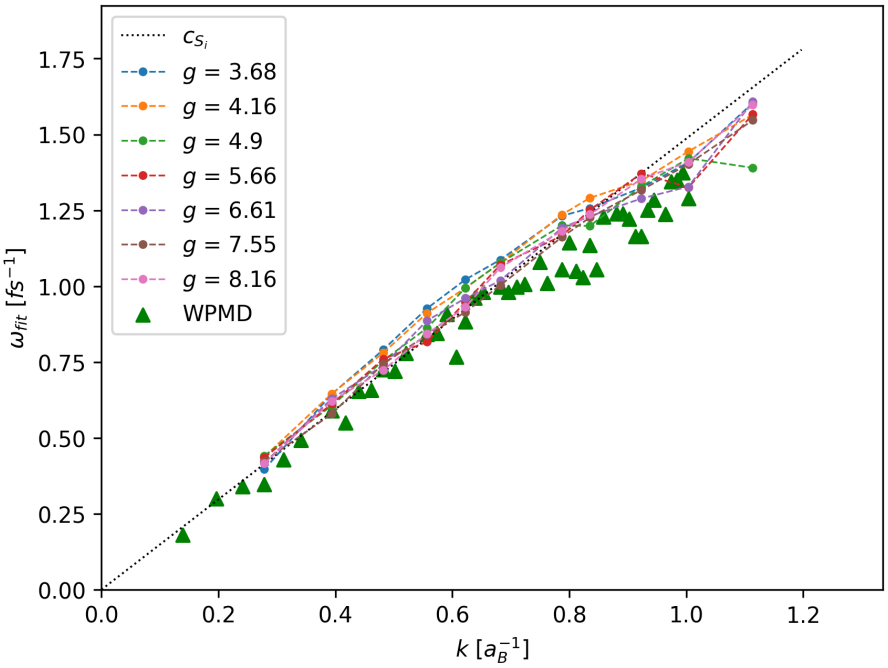


Figure 4.12: Confinement Bohm SPH: frequencies of fitted progressive modes for the ion dynamic structure factors from scan of confinement strengths. Confinement strength unit is $\mathrm{Ha/a_B^2}$, $c_{S_i}$ is the dispersion computed according to equation (4.3.2) for the ion sound speed.

where $\Lambda_e = h/\sqrt{2\pi m_e k_B T_e}$. The increase of plasmon frequency with a stronger Bohm interaction is broadly in agreement with analytical dispersion relations for quantum plasmas, with an $\hbar$ dependent term emerging at $k^4$ as above (although quantum statistical effects can determine the thermal velocity $k^2$ term if $\theta < 1$). Beyond this, I note the general suppression of the plasmon frequency from Bohm SPH relative to the IDR relation, which has also been observed in WPMD computation of electron dynamics [71] in a similar hydrogen system. As mentioned previously and shown explicitly in [71], this suppression occurs when collisions (both electron-electron and ion-electron) and exchange effects are included. To further investigate the free electron dispersion at larger $k$ values a smaller electron size is desirable.

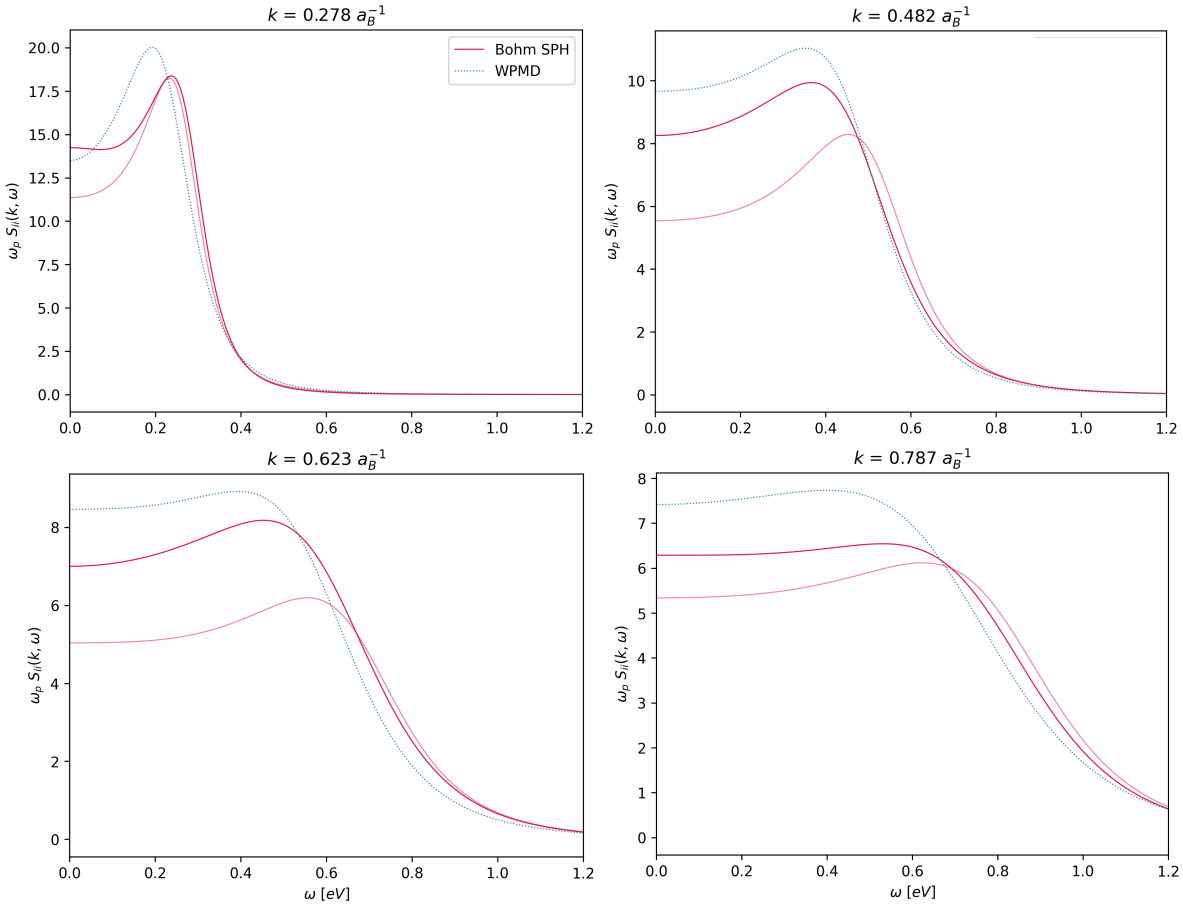


Figure 4.13: Confinement Bohm SPH: ion dynamic structure factors for selected $k$ modes for strongest ($g = 8.16\,\mathrm{Ha/a_B^2}$, dark red) and weakest ($g = 3.68\,\mathrm{Ha/a_B^2}$, light red) confinement. Compared to WPMD outputs (dotted blue).

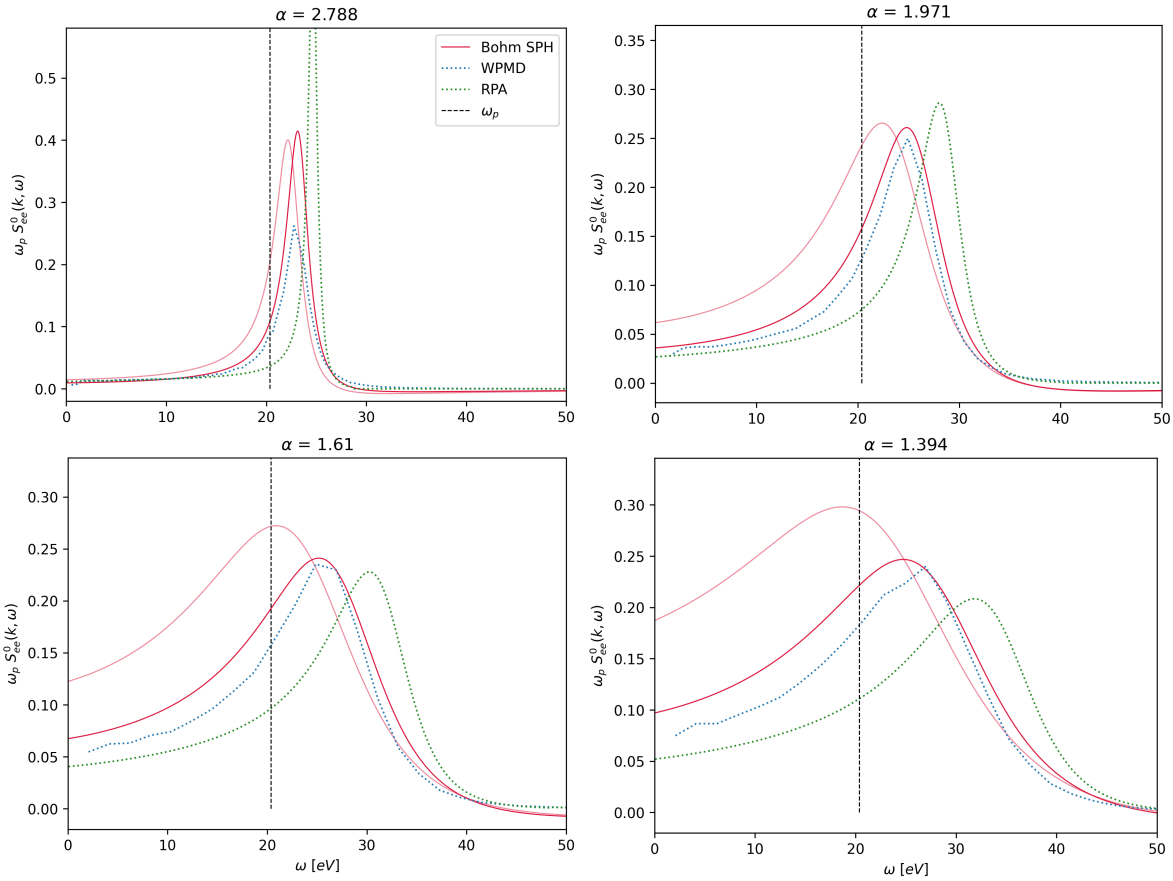


Figure 4.14: Confinement Bohm SPH: free electron dynamic structure factors for collective scattering k values $\alpha > 1/(k\lambda_S)$ for strongest ($g = 8.16\,\mathrm{Ha/a_B^2}$, dark red) and weakest ($g = 3.68\,\mathrm{Ha/a_B^2}$, light red) confinement. Compared to WPMD (dotted blue) and RPA (dotted green) outputs.

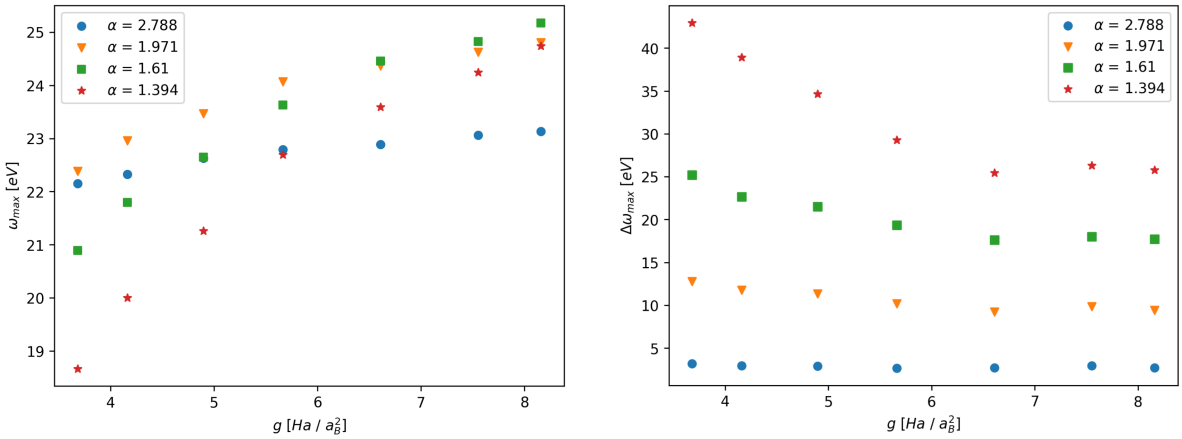


Figure 4.15: Confinement Bohm SPH: maximum value (left) and FWHM of plasmon (right). Computed for collective scattering k values $\alpha > 1/(k\lambda_S)$ across all confinement strengths $g$ sampled.

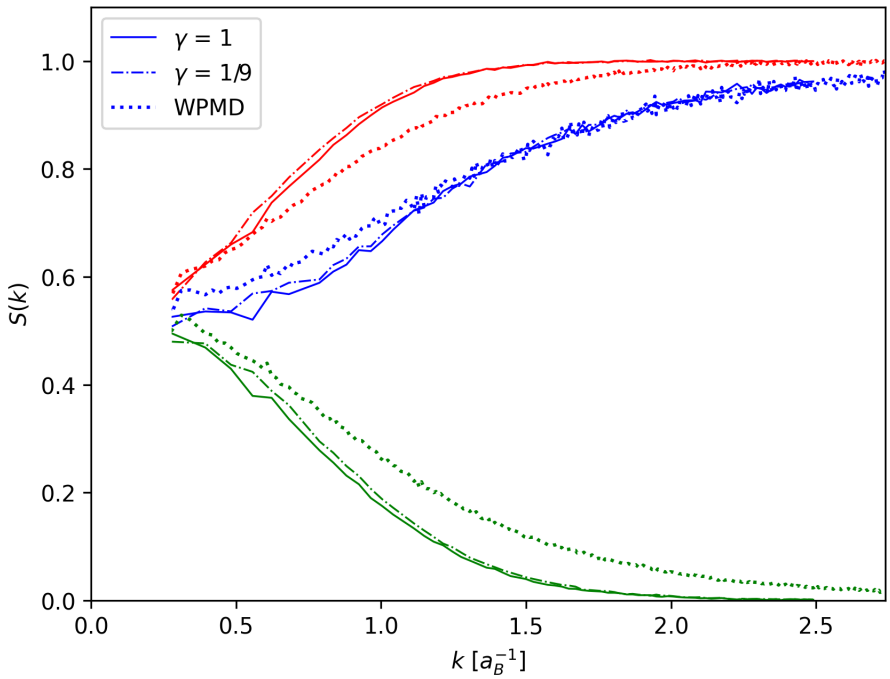


Figure 4.16: Confinement Bohm SPH: Proton - proton (blue), electron - electron (red), and proton - electron (green) static structure factors for the strongest confinement $g = 8.16\,\mathrm{Ha/a_B^2}$ case, comparing different Bohm interaction strengths $\gamma$.

## 4.4 Conclusions

The non-adiabatic simulation of warm dense hydrogen with Bohm SPH has been investigated in this chapter. Having full energy exchange between the point ions and SPH particles is a thermodynamic challenge, with a surplus of translational degrees of freedom compared to the real system, and with no general temperature scaling possible as in PIC. This challenge is made abundantly clear by the poor structure results produced with the simple approach of keeping the SPH temperature constant while varying the electronic resolution via $N_{ppe}$. An improvement, at least for the ionic outputs which agreed well with WPMD, is provided by the two-temperature approach. However this suffers from a lack of electronic information.

Given that confinement Bohm SPH can extract electronic trajectories, I consider it the most useful approach for systems where we have simultaneous interest in ion and electron dynamics. However, there is now a free parameter in the model, the

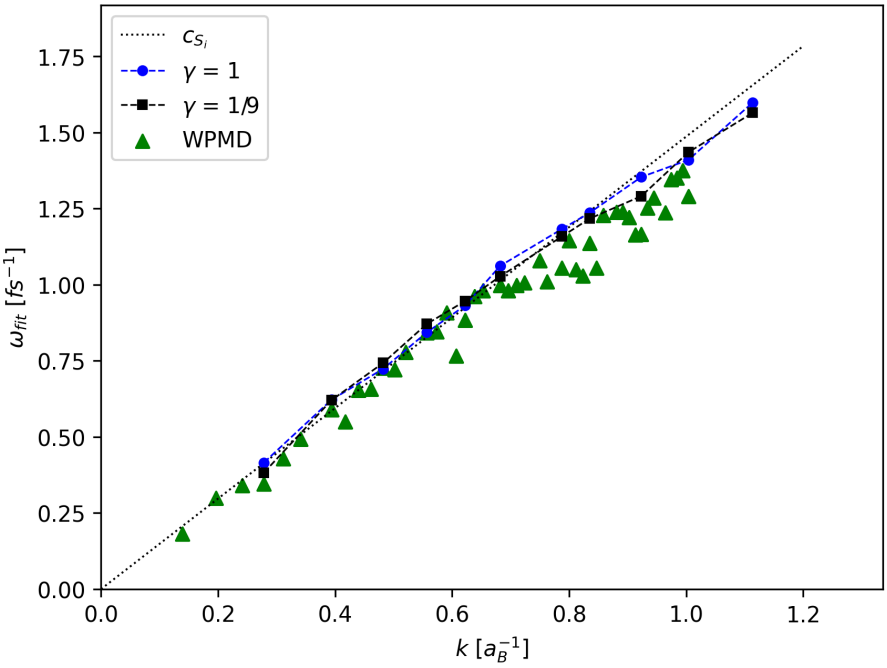


Figure 4.17: Confinement Bohm SPH: frequencies of fitted progressive modes for the ion dynamic structure factors in the strongest confinement $g = 8.16\,\mathrm{Ha/a_B^2}$ case, comparing different Bohm interaction strengths $\gamma$; $c_{S_i}$ is the dispersion computed according to equation (4.3.2) for the ion sound speed.

confinement potential strength, which needs to be well understood and controlled when interpreting results. Hence a scan of confinement strengths was conducted, revealing how the confinement strength affects the overall electron sizes, and subsequently the dynamic screening of the plasma. With the selected SPH parameters, it seems that considerable further contraction of the electrons beyond approximately $H \approx 2\,\mathrm{a_B}$ is not feasible for this density of hydrogen (with $H$ the Gaussian width). In contrast the reference WPMD simulations had a mean size of $H_W = 1.44\,\mathrm{a_B}$, to which I ascribe the major differences in structure outputs between the simulation schemes, particularly in the electronic static structure. The IAW dispersion and the collective ($\alpha > 1$) free electronic dynamic structure factors (plasmons) agree very well with the WPMD output.

The specific effect of the Bohm interaction was investigated by reducing $\gamma$ from 1 to 1/9. There were some marginal differences in the $S(k)$ profiles, with the $\gamma = 1/9$ outputs

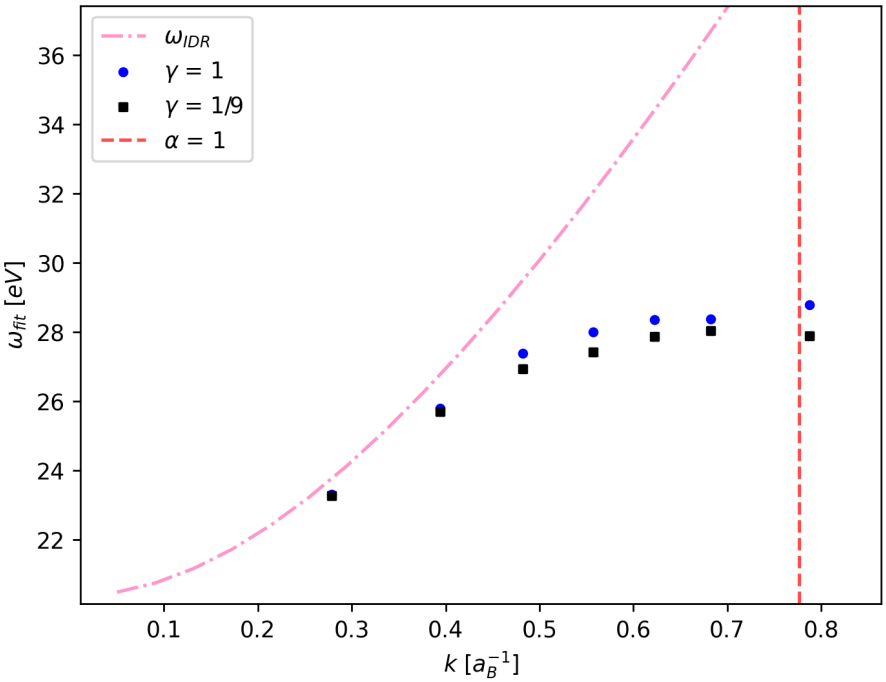


Figure 4.18: Confinement Bohm SPH: frequencies of fitted progressive modes for the free electron dynamic structure factors for the strongest confinement $g = 8.16\,\mathrm{Ha/a_B^2}$ case, comparing different Bohm interaction strengths $\gamma$. Plotted alongside $\omega_{IDR}$ expression (4.3.3).

larger for scattering vectors around the expected screening length $\kappa = 1/\lambda_S = 0.78\,\mathrm{a_B^{-1}}$. Furthermore, $\gamma = 1$ has a slightly different (higher frequency) plasmon dispersion, as expected from analytical relations. Although the differences between the two $\gamma$ values are not enormous, they are still observable and I expect them to be more pronounced in a strongly degenerate ($\theta < 1$) system.

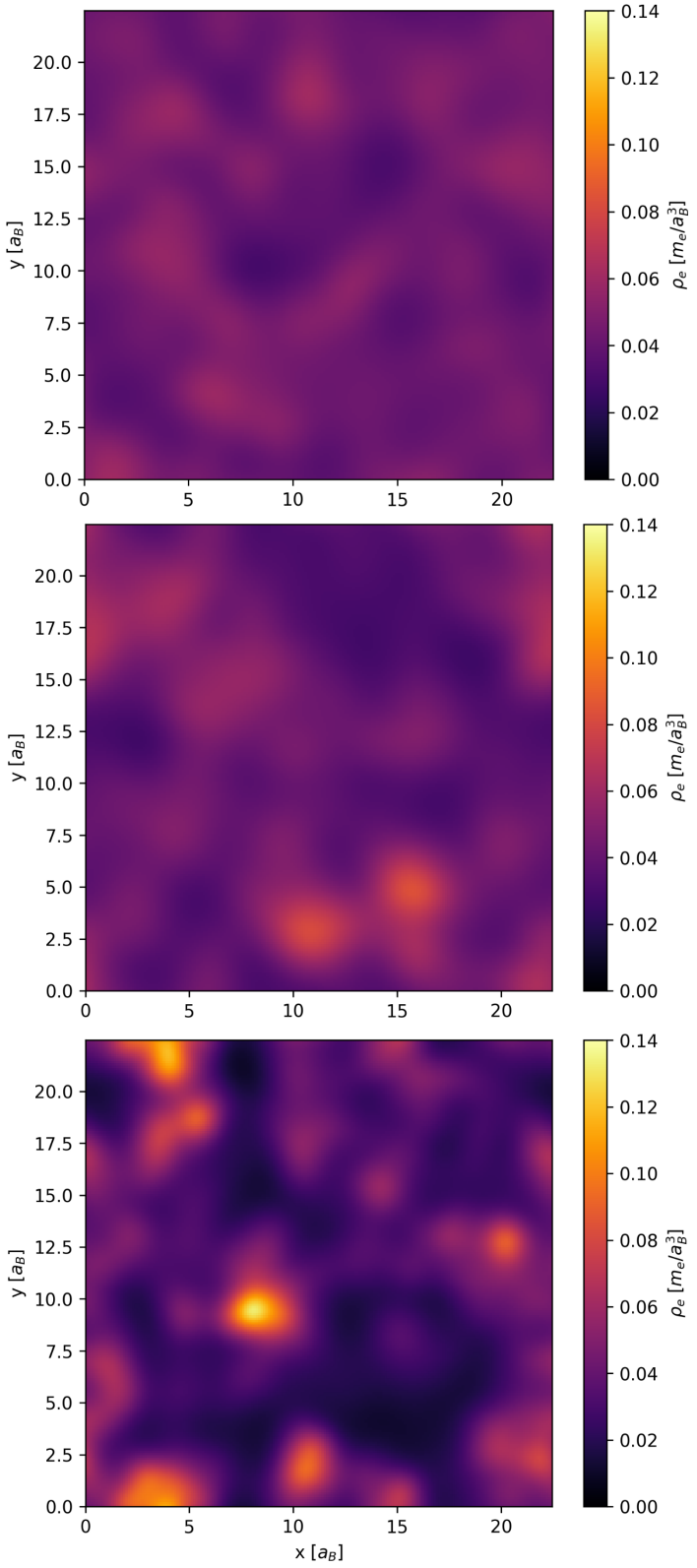


Figure 4.19: Example electron density cross sections visualised from 'simple' (top) 'two-temperature' (middle) and 'confinement' (bottom) Bohm SPH simulations. All computed with $N_{ppe} = 32$.

# Chapter 5

# Non-Thermal Electron Relaxation

In this chapter I shall apply Bohm SPH to an additional problem, the relaxation of non-thermal electronic distributions in warm and hot dense plasma. This is an ideal testbed for Bohm SPH, where its explicit evolution of the electron density can contribute to a better understanding of WDM transport properties. Specifically, a plausible non-thermal electron distribution for aluminium under X-ray free electron laser (XFEL) drive is calculated using CCLFY (introduced below), and sampled for the starting velocities of Bohm SPH simulations. Once again however, the thermal effect of additional degrees of freedom in our model, introduced to better the resolve the electron density, must be considered. As such, the methods and data presented here are a feasibility study of using Bohm SPH in this space, with the dependence on resolution thoroughly investigated.

First, XFELs are briefly introduced, followed by atomic kinetic software that models plasmas generated at such facilities. A leading atomic kinetic code CCFLY employs a Fokker-Planck collisional operator that evolves non-thermal electronic distributions. However, this operator includes a Coulomb logarithm term which becomes ill-defined at solid (and higher) densities. This motivates comparing the Fokker-Planck evolution of non-thermal electron distributions with explicit simulation techniques such as Bohm

SPH. Subsequently the Bohm SPH setup and outputs are discussed.

This analysis is particularly relevant to a novel scheme suggested for investigation of electron thermal relaxation timescales at XFEL facilities in Ref. [163] through variation of the duration of the ultra-short driving pulse (several fs down to ideally sub fs). Here the experimental observables are (time-integrated) emission spectra from the dense plasma. For CCFLY to attempt to reproduce these spectra, the validity of the Coulomb logarithm expression (and associated relaxation timescales) used in its Fokker-Planck operator must be probed at high densities. In this analysis, XFEL parameters are selected that produce a highly non-thermal electron distribution in CCFLY, used as a starting point for a direct comparison between Bohm SPH, and, after dependencies on $N_{ppe}$ and the average Coulomb coupling between SPH particles are understood, the isolated Fokker-Planck operator. In this way I emphasise that the comparison is between codes, but with ramifications for the full CCFLY software in its reproduction of experiment. The hierarchy can be understood as Bohm SPH $\rightarrow$ Fokker-Planck $\rightarrow$ CCFLY $\rightarrow$ experiment.

## 5.1 Typical Modelling of XFEL Experiments

In recent years, XFELs such as LCLS [164], have been used to routinely create and diagnose warm and hot dense plasma states. They can deliver short (down to roughly a fs) and intense pulses (up to $10^{19}\mathrm{Wcm}^{-2}$) of tunable, multi keV x-ray photons in a narrow bandwith. The isochoric heating of a metallic target with such pulses, where the target has no time to expand, creates solid-density plasma with temperatures up to 100s of eV. Highly non-thermal electron energy distributions are often generated in XFEL experiments, driven by photoionisation and Auger processes. Thorough discussion of XFEL theory, performance and selected experimental studies can be found in Ref.s [165–168].

Accompanying XFEL experiments has been a raft of atomic kinetic software, built

to predict and reproduce the emission spectra of the generated plasmas, and thus determine the validity of the physical models used in the software. The term atomic kinetics refers to the population dynamics of ions. These dynamics are governed by processes such as collisions, photoionisation and photoexcitation, radiative processes, and Auger processes, with their respectively likelihoods affected by plasma conditions.

CCFLY is a code at the forefront of such software. CCFLY is a non-thermal, non-LTE collisional radiative code designed to model the time-dependent evolution of both electron distributions and ion states interacting with intense x-ray fields on ultra-short time-scales [169]. This includes a large extent of super-configurations to describe the precise atomic physics of the system. CCFLY was developed as an upgrade to the SCFLY [170, 171] suite which was itself modelled on the FLYCHK code [172]. Beyond previous models which always assume a Maxwellian electron distribution, CCFLY includes modelling of arbitrary, non-thermal distributions which are evolved with a Fokker-Planck [173] numerical framework which accounts for collisional processes in the plasma. Ref. [169] demonstrated the importance of including non-thermal electron distributions alongside atomic kinetics when modelling plasmas generated by experimentally achievable XFEL beam parameters, with clear effects on the ion population and emission spectrum.

The overall structure of the Fokker-Planck framework in CCFLY is described in Ref.s [169, 163], with terms accounting for elastic electron collisions and inelastic electron collisions (such as collisional excitation of an ion), and a source term (accounting for ionisation/recombination). The term of interest for our analysis is the elastic collisional operator, against which we can make a direct comparison with Bohm SPH simulations. The isotropic, non-relativistic, elastic collision operator used in CCFLY is described in Ref.s [174, 175], given in integro-differential form as

$$\left(\frac{\partial f_v(v)}{\partial t}\right)_{ee} = \frac{4\pi\chi_{ee}}{3}\frac{1}{v^2}\frac{\partial}{\partial v}\left[\frac{1}{v}\frac{\partial W(v)}{\partial v}\right], \tag{5.1.1}$$

where $f_v(v)$ is the velocity (speed) distribution of the electrons, with the function $W(v)$ defined as

$$W(v) = f_v \int_0^v f_u u^4 \, \mathrm{d}u + v^3 f_v \int_v^\infty f_u u \, \mathrm{d}u - 3 \int_v^\infty f_u u \, \mathrm{d}u \int_0^v f_u u^2 \, \mathrm{d}u, \tag{5.1.2}$$

and finally with $\chi_{ee}$ defined

$$\chi_{ee} = \frac{e^4 \ln(\Lambda)}{4\pi\varepsilon_0^2 m_e^2}. \tag{5.1.3}$$

$\ln(\Lambda)$ is the Coulomb logarithm, which is therefore crucial in determining the evolution of the electronic energy distribution. Typically the Coulomb logarithm is defined in terms of impact parameters

$$\ln(\Lambda) = \ln\left(\frac{b_{\max}}{b_{\min}}\right) \tag{5.1.4}$$

which can be equated to appropriate plasma length scales, such as the Debye or Thomas-Fermi wavelength for $b_{\max}$. A semi-empirical form for the Coulomb logarithm, adopted thus far in CCFLY, is

$$\ln(\Lambda_{ee}) = 23.5 - \ln\left(n_e^{1/2} T_e^{-5/4}\right) - \left[10^{-5} + \left(\ln T_e - 2\right)^2 / 16\right]^{1/2}, \tag{5.1.5}$$

where $n_e$ is in $\mathrm{cm}^{-3}$ and $T_e$ in eV, as written in the NRL plasma formulary [176]. Coulomb logarithms have an associated relaxation time for electron collisions, which can be derived from the Spitzer and Härm model [177]

$$\tau_{S_{\mathrm{ee}}} = 16\sqrt{\frac{2}{\pi}} \frac{m_{\mathrm{e}}^{1/2} \epsilon_0^2 \left(k_{\mathrm{B}} T_{\mathrm{e}}\right)^{3/2}}{n_{\mathrm{e}} q_{\mathrm{e}}^4 \ln\left(\Lambda_{\mathrm{ee}}\right)}. \tag{5.1.6}$$

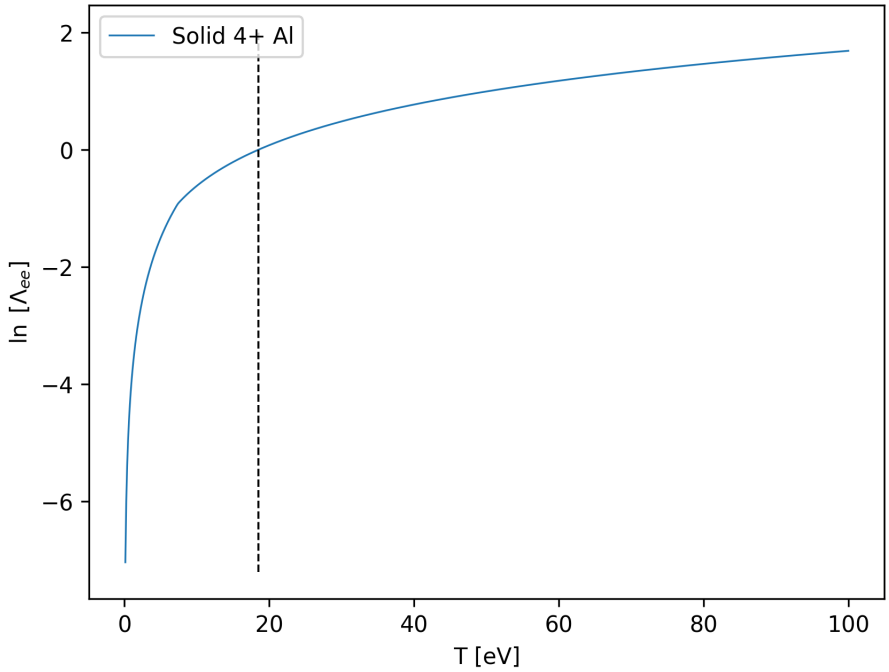


Figure 5.1: Electron-electron Coulomb logarithm calculated from Equation 5.1.5, computed for solid density aluminium with ionisation $Z = 4$. $\ln(\Lambda_{ee})$ becomes negative (unphysical) to the left of vertical line at 18.5 eV.

Now however, a problem emerges for application of the Fokker-Planck framework to dense plasmas, namely that the Coulomb logarithm becomes ill-defined. Derivation of the Coulomb logarithm is built upon the assumptions of binary, small-angle collisions, which breaks down when inter-particle coupling becomes large. A plot of $\ln(\Lambda_{ee})$ computed accorded to Equation (5.1.5) for solid density 4+ aluminium, as investigated in the following section, is given in Figure 5.1. This clearly shows how $\ln(\Lambda_{ee}) < 0$ when $T_e$ falls below roughly 20 eV, leading to a divergent relaxation time $\tau_{S_{\mathrm{ee}}}$ in Equation (5.1.6).

Ref. [178] compared a more accurate quantum kinetic approach to the usual Spitzer analysis [177, 179] for ion-electron temperature equilibration. They demonstrated that while the Spitzer theory for ion-electron relaxation is improved by judicious selection of impact parameters in the Coulomb logarithm, it still fails for small values ($< 2$).

Uncertainty in $\ln(\Lambda)$ and therefore $\tau_{S_{\mathrm{ee}}}$ for moderately to strongly coupled plasmas motivates use of explicit simulation techniques that capture collisions directly. While

electron-ion thermal equilibration has been investigated previously with explicit simulation techniques [138, 139, 180], there has not been, to the author's knowledge, an equivalent investigation for electron-electron relaxation. Enter Bohm SPH for such an attempt.

## 5.2 Bohm SPH Simulation Setup

The starting point of this analysis is a non-thermal electron distribution generated by CCFLY for solid density aluminium under XFEL drive. The simulated XFEL beam has photon energy 2 keV with a Gaussian time profile of FWHM 0.1 fs, $2 \cdot 10^{19}$ Wcm$^{-2}$ peak intensity, spot size 1 $\mu$m$^2$, and is incident on a 10 $\mu$m thick aluminium target. The temporal profile is centred at 0.5 fs in the simulation time, as evident in Figure 5.3. Used together these parameters are not currently feasible on XFEL machines but are likely to be in the near future. The K-edge of Al is at 1560 eV, so the photons will ionise the 1s electrons.

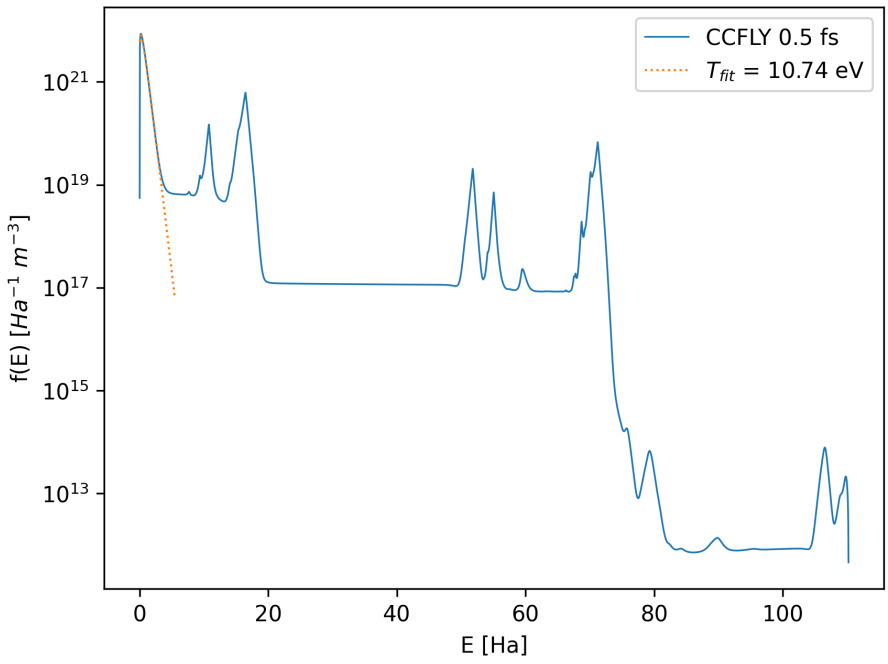


Figure 5.2: Maximally non-thermal electron distribution in aluminium at midpoint (time) of XFEL pulse, as calculated in CCFLY.

The maximally non-thermal electron distribution occurs around the maximal intensity of the XFEL pulse at 0.5 fs. The distribution at 0.5 fs of the CCFLY simulation is plotted in Figure 5.2. The distribution has pronounced non-thermal features, with K-shell photoionisation producing the peaks between 15 and 20 Ha, Auger decay the features around 55 Ha, and L-shell photoionisation the peak at 70 Ha. Additionally, a very weak feature above 100 Ha is visible, driven by collisional de-excitation. The thermal bulk of the distribution is well fitted by a Maxwellian at $T = 10.74\,\mathrm{eV}$, however an effective temperature is defined via

$$k_B T_{\mathrm{eff}} = \frac{\int E f(E)\, dE}{\int f(E)\, dE}, \tag{5.2.1}$$

which yields $T_{\mathrm{eff}} = 49.6\,\mathrm{eV}$ for the figure distribution.

Whereas in CCFLY the mean charge state and electron density evolves with time according to ionisation and recombination events, Bohm SPH requires a fixed ionisation and density given that it does not incorporate atomic kinetics. For full reference, the mean ionisation output from the CCFLY simulation is plotted in Figure 5.3. The corresponding mean charge for the non-thermal distribution at 0.5 fs plotted in Figure 5.2 is 3.38, however it continues to rise with time. For the Bohm SPH simulations, a fixed nuclear charge state of $Z = 4$ is used, corresponding to one ionised electron per atom and which is simple to implement. Clearly this does not match the later evolution of the mean ionisation in CCFLY in Figure 5.3, but I re-emphasise that this non-thermal analysis is between Bohm SPH and the Fokker-Planck operator, not CCFLY or experiment. A fixed nuclear charge state is satisfactory for this case where I exclude ion population dynamics. With $Z = 4$, the electron density is $n_e = 2.41 \cdot 10^{23}\,\mathrm{cm}^{-3}$. Along with the effective temperature, this corresponds to $\theta = 3.51$ and $\Gamma_{ee} = 0.291$ for the electrons, placing them on the periphery of the WDM regime. The ions remain cold during the XFEL drive since the predominant absorption pathway for the x-rays is photoionisation, and are not expected to equilibrate with the electrons for 100s of fs.

Hence, in the Bohm SPH simulations they are initialised on an FCC lattice at room temperature.

Now, using the velocity distribution from the CCFLY output in Figure 5.2 to sample the starting velocities for the SPH particles, a direct comparison can be made between the elastic electronic collision operator in the Fokker-Planck module used in CCFLY, and Bohm SPH. This is reasonable provided the total kinetic energy of the SPH particles remains roughly constant for the duration of the simulation after sampling. The Fokker-Planck module is run by taking the same starting energy distribution, and disabling the source and inelastic collision operators. For equivalence to Bohm SPH, the Fokker-Planck starting distribution is scaled to be equivalent to a mean density of $\mathrm{Z} = 4$. At the plasma conditions stated above ($n_e$, $T_{\mathrm{eff}}$) the Coulomb logarithm computed by Equation (5.1.5) is $\ln(\Lambda_{ee}) = 0.985$. While not negative, in light of previous investigations this is around the limit of applicability for the Fokker-Planck/Spitzer framework and is ripe for comparison with explicit simulations from Bohm SPH. For reference, the corresponding Spitzer relaxation time for electron collisions (5.1.6) with these parameters is $\tau_{S_{\mathrm{ee}}} = 0.137\,\mathrm{fs}$.

Seemingly there is a straightforward setup for Bohm SPH. However one must, as in the last chapter, consider the SPH electron density resolution and the subsequent effect of any additional degrees of freedom. At $T_{\mathrm{eff}} = 49.6\,\mathrm{eV}$ and $n_e = 2.41 \cdot 10^{23}\,\mathrm{cm}^{-3}$ the expected screening length is $\lambda_S = 2.06\,\mathrm{a_B}$. Requiring that the average SPH kernel be $\overline{h} < \lambda_S$ in the warm dense hydrogen simulations ensured that the ion-ion interaction was screened appropriately, yielding compelling IAW and static structure results. However, unlike in the previous chapter, I am not as interested in the ionic dynamics, especially given how cool the ions are. Rather, I wish to see how the electronic energy distribution thermalises in the presence of the ionic lattice. Hence I relax the requirement to $\overline{h} < r_{s_{ii}}$, with $r_{s_{ii}} = 2.99\,\mathrm{a_B}$ the ion Wigner Seitz radius at these conditions. In the following simulations, taking an SPH density-width parameter of $\zeta = 1.3 \cdot \sqrt{2}$ , this is satisfied

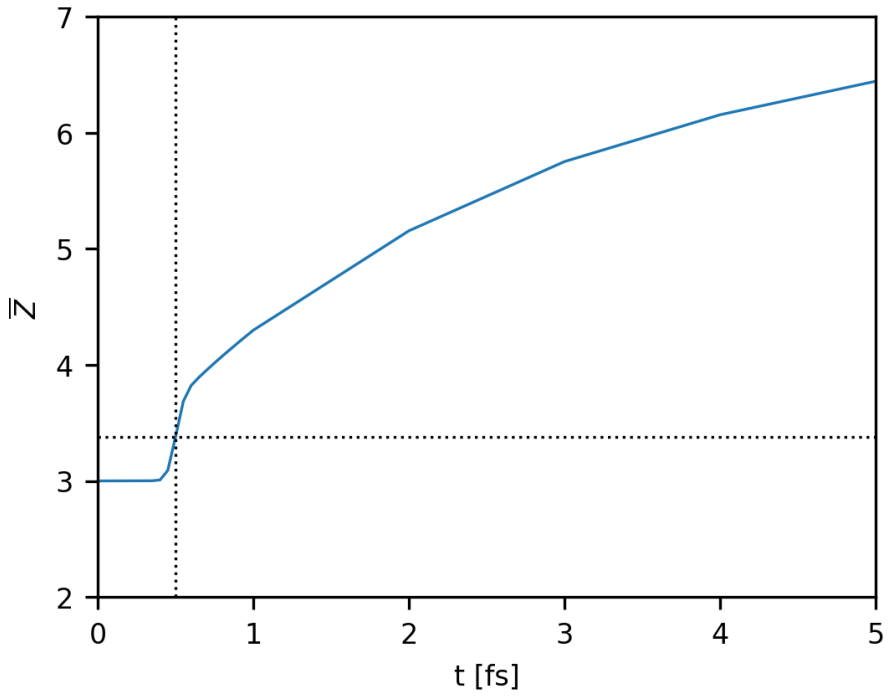


Figure 5.3: Mean charge state of aluminium in CCFLY simulation. Vertical dotted line at 0.5 fs corresponds to the time of the maximally non-thermal f(E) plotted in Figure 5.2, at which time the mean charge state is 3.38.

with $N_{ppe} = 8$ for which $\overline{h} = 2.79\,\mathrm{a_B}$. However to understand the effect of varying $N_{ppe}$ I also investigate values of $N_{ppe} = 4$, 16 and 32, and perform this variation in three different schemes, similarly to Chapter 4.

The three different schemes are characterised by how they sample the velocity (energy) distribution. The first approach, is to sample the same distribution regardless of $N_{ppe}$ value, equivalent to constant temperature. The second is to scale the distribution to ensure the same thermal energy in the system regardless of $N_{ppe}$, accomplished by scaling the energy axis of $f(E)$ by $1/N_{ppe}$. Finally, rather than applying a confinement potential, the third scheme is to ensure that the SPH particles experience the same average Coulomb coupling as the electrons in the physical system. This is motivated by the results from the first two schemes which suggest an inverse dependence between $\Gamma_S$, the SPH particle coupling, and its thermalisation time. Recall the definition of the SPH Coulomb coupling first written in Section 3.1.4

$$\begin{aligned}\Gamma_S &= \frac{q_S^2}{4\pi\epsilon_0 a_S k_B T_{\text{eff}}} \operatorname{erf}\left(\frac{a_S}{\sqrt{2}h_S}\right) \\ &= \frac{(e/N_{ppe})^2}{4\pi\epsilon_0 k_B T_{\text{eff}}} \left(\frac{4\pi N_{ppe} n_e}{3}\right)^{1/3} \operatorname{erf}\left(\frac{(N_{ppe}n_e)^{1/3}}{\sqrt{2}\zeta}\left(\frac{3}{4\pi N_{ppe}n_e}\right)^{1/3}\right) \\ &= \Gamma_e N_{ppe}^{-5/3} \operatorname{erf}\left(\frac{1}{\sqrt{2}\zeta}\left(\frac{3}{4\pi}\right)^{1/3}\right).\end{aligned} \tag{5.2.2}$$

Applying a factor of $N_{ppe}^s$ to the standard $\Gamma_S$ expression and setting it equal to a target coupling extracts the required value of $s$

$$\begin{aligned}\Gamma_S N_{ppe}^s &= \Gamma_e^{\text{target}} \\ \therefore s &= \frac{\ln(\Gamma_e^{\text{target}}/\Gamma_S)}{\ln(N_{ppe})}.\end{aligned} \tag{5.2.3}$$

Taking $T_{\text{eff}}$ as the variable I alter to achieve the required coupling, the energy axis $E$ in Equation (5.2.1) is compressed by a factor of $N_{ppe}^{-s}$ when sampling the CCFLY distribution. Hence when comparing the distribution shapes of different coupling values such as in Figure 5.7, the energy axis is always scaled by a factor $N_{ppe}^{-s}$ to ensure a direct comparison.

There are several further important details regarding the Bohm SPH simulations. Periodic boxes with $N_i = 500$ ions on an FCC lattice are used, corresponding to a box length of $L = 38.3\,\text{a}_\text{B}$. The aluminium ions are treated as bare 4+ charges and no pseudopotential is used for their interaction with SPH particles. The Pauli potential used between SPH particles is temperature dependent (see 3.1.2), using the effective temperature $T_{\text{eff}}$ for all simulations. The simulations commence with an equilibration stage. Initially the SPH particles sample velocities from the Maxwellian bulk and are kept at this temperature for the first 2.5 fs by an NVT thermostat. Note that the Maxwellian temperature undergoes the same scaling as $T_{\text{eff}}$ in the constant energy and

target coupling simulations. At the same time, the ions are also equilibrated under an NVT thermostat to room temperature, this occurs regardless of scalings in the SPH components. Then, at 2.5 fs, the SPH particles sample the (scaled) non-thermal distribution in Figure 5.2, and the whole system enters NVE, after which the SPH velocity distributions are computed. Outputs of the simulation kinetic and potential energies are given in Figure 5.10. Other than Figure 5.10, all times plotted or discussed in the results section consider the sampling time as $t = 0$. Simulations are run with a timestep of 0.2 as, and with $m_{iter} = 4$ iterations of the fixed point calculation of SPH density and kernel widths. Each condition is repeated three times, with the distributions averaged.

As a final aside prior to the results, it is acknowledged that to investigate thermal relaxation an arbitrary non-thermal distribution, such as beam-on-tail, could have been investigated. However, an experimentally plausible distribution has been selected here to emphasise the importance of this analysis to contemporary XFEL investigations and supporting simulations.

## 5.3 Results

First I examined the output from the simple approach of sampling the same $f(E)$ distribution across resolutions, keeping a constant effective temperature, plotted in Figure 5.4. The distributions are normalised hence have arbitrary units on y axis. Furthermore, in all Bohm SPH distributions plotted in this section, a Gaussian smoothing filter has been applied to the histograms with standard deviation $\sigma = 0.367$ Ha. Comparing the outputs for $N_{ppe} = 4, 8, 16, 32$ at the same timestep, 19.98 fs post sampling, the distributions are clearly at different stages of thermalisation. Smaller values of $N_{ppe}$ correspond to faster broadening of the non-thermal features. Also plotted on the figures are the effective couplings for each resolution via Equation (5.2.2), which scales as $N_{ppe}^{-5/3}$. For interest, I compared different time outputs of the different resolutions scaled

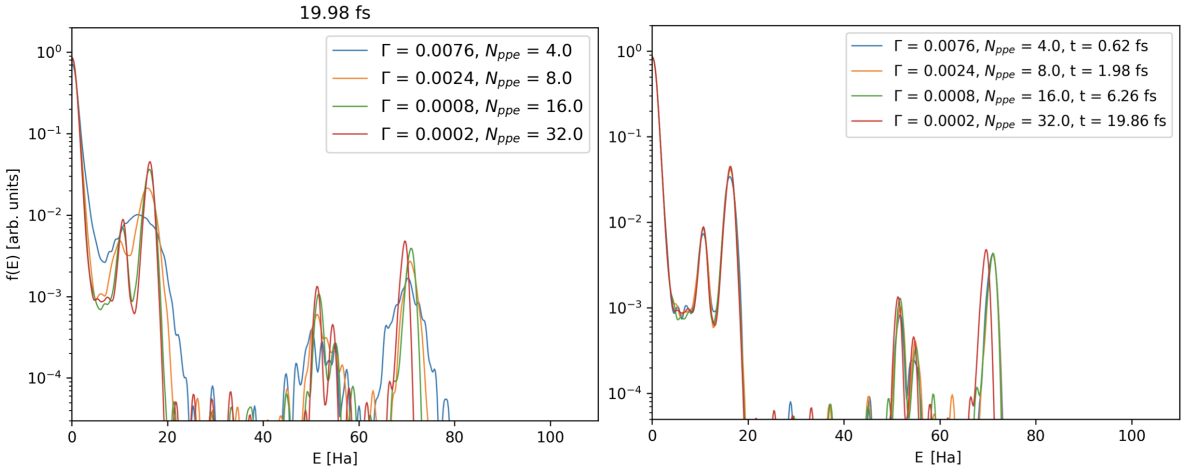


Figure 5.4: Constant Temperature: SPH particle kinetic energy distributions for Bohm SPH simulations of an initially non-thermal electronic distribution of 4+ aluminium. Left: comparison across resolutions $N_{ppe}$ at the same time (19.98 fs). Right: comparison across resolutions at times scaled by $N_{ppe}^{5/3}$.

by $N_{ppe}^{5/3}$, and observed that the distributions are near identical, with only a slight discrepancy at the highest energy feature. This is the first evidence of the thermalisation timescale being inversely proportional to the Coulomb coupling.

Subsequently I investigated the case of constant thermal energy while scanning resolutions $N_{ppe} = 4, 8, 16$. The energy distribution was sampled with the energy axis scaled by $N_{ppe}^{-1}$, such that the total thermal energy of the SPH particles equals that of $N_e$ electrons. Consider the results of the 'two-temperature' approach of the previous chapter where the SPH particles are forced to have the thermal energy of $N_e$ electrons. This approach enabled better screening of the ions, with compelling static and dynamic ion structure outputs. One might expect promising results with such an approach here, with convergence achieved as $N_{ppe}$ increases. This is not the case, as shown in the left inset of Figure 5.5. At 5.02 fs, the distributions are at noticeably different stages of thermalisation. However if a factor of $N_{ppe}^{2/3}$ is applied to the time outputs, the inverse of the coupling ratios, the distributions match very well.

Armed with the observation that the timescale for thermalisation in Bohm SPH $\tau$ is seemingly determined by the coupling parameter, I confirmed this by scanning $N_{ppe}$

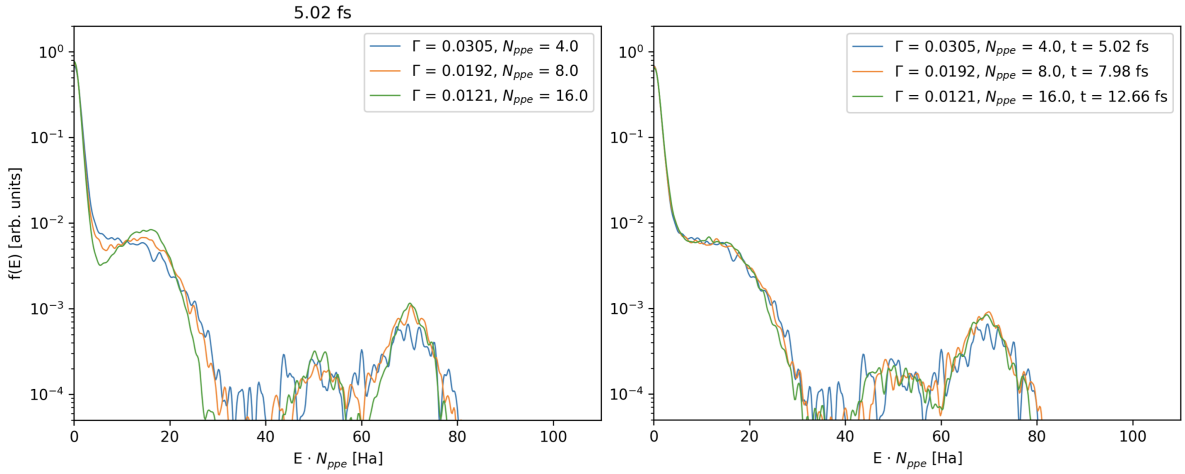


Figure 5.5: Constant Energy: SPH particle kinetic energy distributions for Bohm SPH simulations of an initially non-thermal electronic distribution of 4+ aluminium. Left: comparison across resolutions $N_{ppe}$ at the same time (5.02 fs). Right: comparison across resolutions at times scaled by $N_{ppe}^{2/3}$. Histogram x axes scaled by $N_{ppe}$ to give better shape comparison.

while keeping $\Gamma_S$ constant, here at 0.272. The outputs are plotted in Figure 5.6, with the distributions matching well at the example times of 0.26 fs and 4.02 fs. This result is also interesting given that at $N_{ppe} = 4$, $\overline{h} = 3.52\,\mathrm{a_B}$ which is larger than the ion Wigner Seitz radius $r_{s_{ii}} = 2.99\,\mathrm{a_B}$ suggested as a limit on the kernel sizes above. This is evidence that ion-SPH particle interactions are subsidiary to inter-SPH collisions, and do not have a strong impact on the SPH particle thermalisation behaviour.

Next I checked the inverse proportionality between the SPH Coulomb coupling and thermalisation $\tau \propto \Gamma_S^{-1}$. Input energy distributions are scaled according to Equation (5.2.3) to scan $\Gamma_S$ over two orders of magnitude, from 0.00431 to 0.431. In all these simulations $N_{ppe} = 8$. Their outputs are plotted in Figure 5.7, both at the same time (1.02 fs) in the left inset, and with their timesteps scaled by $\Gamma_S^{-1}$ in the right inset. Interestingly, with the $\Gamma_S^{-1}$ scaling the distributions do not match exactly, with sequential differences in the broadening of the non-thermal features. However, their Maxwellian bulks are very consistent.

An quantifiable timescale of thermalisation $\tau$ can be defined by examining the ratio of the effective and Maxwellian fitted temperatures of the SPH energy distribution,

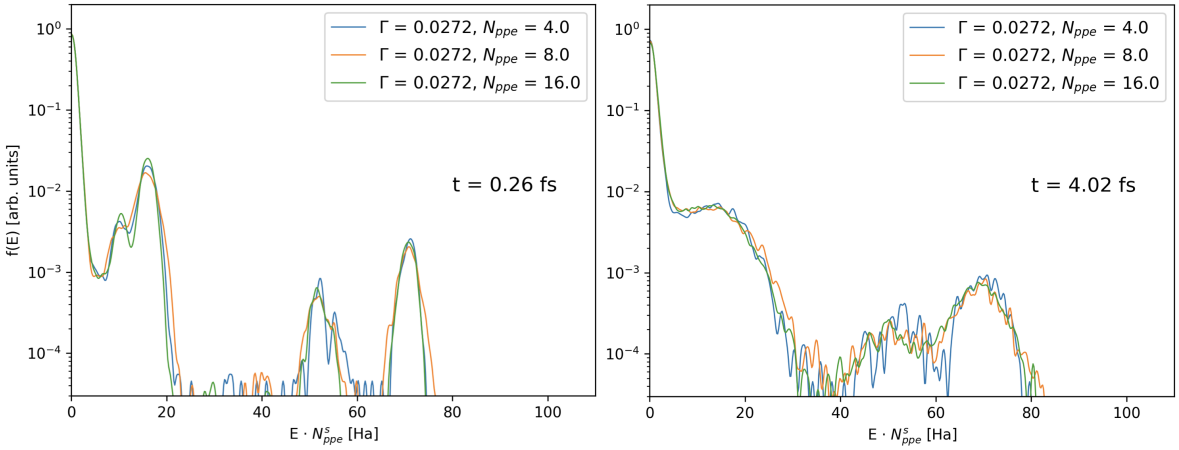


Figure 5.6: Comparison of Bohm SPH distributions with $\Gamma_S = 0.272$ across different resolutions $N_{ppe}$ at two example times: 0.26 and 4.02 fs.

$T_{\text{fit}}/T_{\text{eff}}$. For each distribution output, $T_{\text{eff}}$ is computed according to Equation (5.2.1), and a Maxwellian profile fitted to the bulk, as in Figure 5.2. These outputs for the scanned couplings are plotted in Figure 5.8. Then to extract the timescale, to each ratio $T_{\text{fit}}/T_{\text{eff}}$ is fitted a function of the form

$$g(t) = 1 - a \exp\left(-\frac{t}{\tau}\right) \tag{5.3.1}$$

with $a$ and $\tau$ the fitting parameters. This is demonstrated in Figure 5.8, with the fitted values subsequently plotted in Figure 5.9. Here, the $\tau \propto \Gamma_S^{-1}$ relation is clearly evident. For further reference, the total kinetic and potential energies of the coupling scan simulations are plotted in Figure 5.10.

Finally, having determined that the SPH Coulomb coupling determines thermalisation in Bohm SPH, at least the rate of transfer of energy to the bulk, I made a direct comparison with elastic Fokker-Planck. As stated, the expected electron Coulomb coupling for the Al 4+ system with the $f(E)$ distribution given in Figure 5.2 is $\Gamma_{ee} = 0.291$, so I set $\Gamma_S = 0.291$ as an analogue of this system and compare it to the Fokker-Planck outputs. Comparisons of the distributions from the two methodologies are plotted in Figure 5.11 across times from 0.25 to 8 fs. While the exact shape of the non-thermal

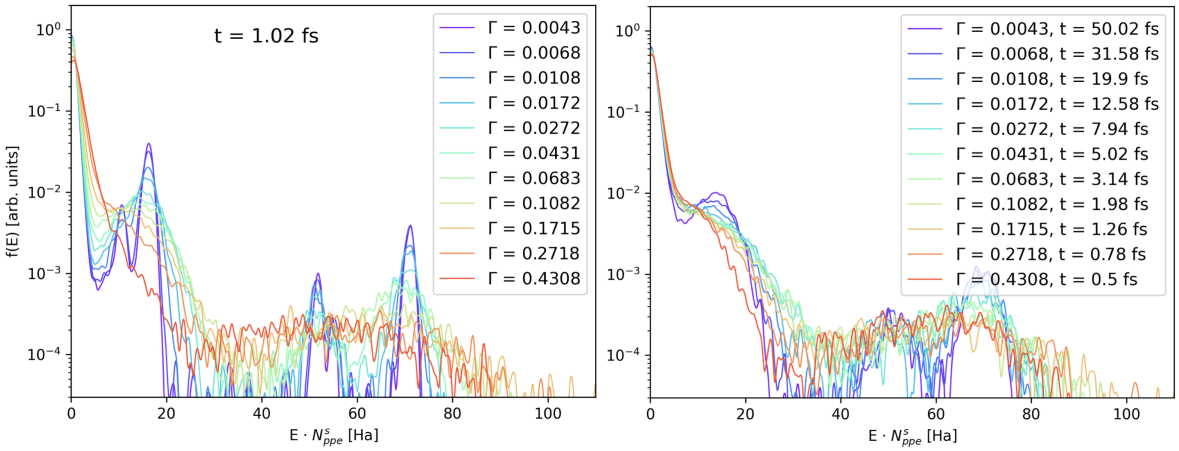


Figure 5.7: Coupling Scan: SPH particle kinetic energy distributions for Bohm SPH simulations of an initially non-thermal electronic distribution of 4+ aluminium. Left: comparison across couplings $\Gamma_S$ at the same time (1.02 fs). Right: comparison across couplings at times scaled by $\Gamma_S^{-1}$. Histogram x axes scaled by $N^s_{ppe}$ to give better shape comparison, with $N_{ppe} = 8$ in all cases.

peaks do not correspond well, with the Bohm SPH outputs broadening significantly quicker than Fokker-Planck, the transfer of energy to the bulk is quite consistent and the schemes have very similar Maxwellian bulk shapes. This is confirmed by $T_{\text{fit}}/T_{\text{eff}}$ analysis plotted in Figure 5.12. The shapes of the ratios are similar, in particular up to around 5 fs after which they slightly diverge and the Fokker-Planck ratio approaches 1 roughly 10 fs later. The fitted timescale for the Bohm SPH output at $\Gamma_S = 0.291$ is $\tau = 2.96$ fs. Note that the timescale $\tau$ defined in Equation (5.3.1) does not correspond with the Spitzer timescale $\tau_{S_{\text{ee}}}$,although by thorough comparison of estimations for $\tau_{S_{\text{ee}}}$ and calculations of $\tau$ from Fokker-Planck simulations at different conditions, a relation might be established between the two.

An additional test is to check the thermalisation behaviour when the ion motion is disabled. In this case, while the SPH particles still experience the Coulomb attraction to the ions, the ions are fixed in place on the FCC lattice. This comparison is shown in Figure 5.13 at two example timesteps, and we observe essentially identical SPH energy distributions. The equivalence between having ion motion on or off demonstrates that there is not significant energy exchange between the ions and SPH-particles on the

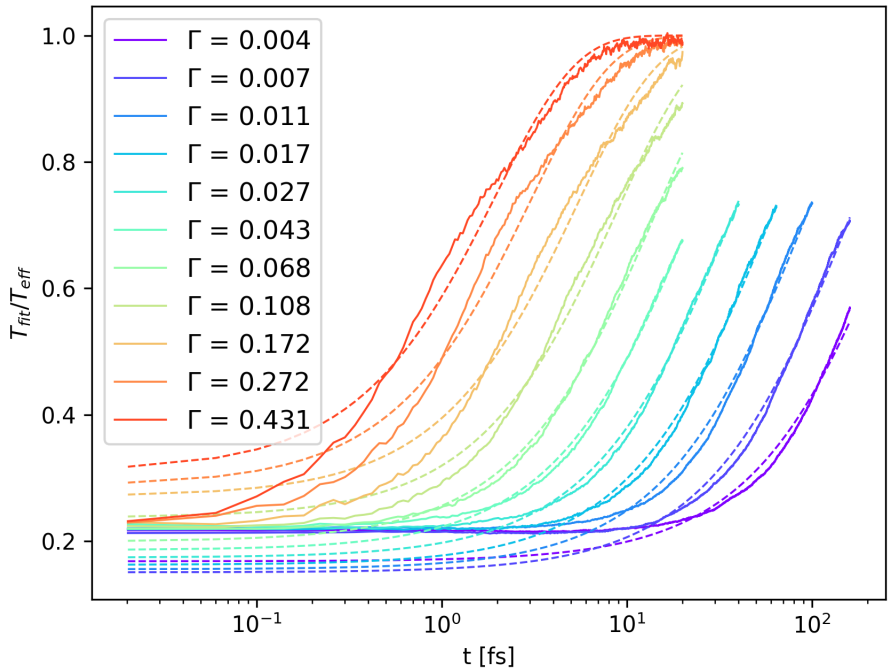


Figure 5.8: Ratios of fitted to effective electronic temperature for Bohm SPHs simulations scanning couplings $\Gamma_S$. Dotted lines correspond to time profiles fitted according to Equation (5.3.1) with $\tau$ values plotted in Figure 5.9.

timescale of the SPH thermalisation.

## 5.4 Conclusions

A first attempt at simulating the explicit electronic thermalisation behaviour of an XFEL-generated aluminium plasma has been presented in this chapter. The starting non-thermal energy distribution was generated via CCFLY. When fixing the ionisation to $Z = 4$, this distribution yielded a (classical) electron Coulomb coupling of $\Gamma_{ee} = 0.291$, and Coulomb logarithm of $\ln(\Lambda_{ee}) = 0.985$ using the semi-empirical formula in Equation (5.1.5). This moderate electron coupling is around the limit of applicability of Fokker-Planck computation and Spitzer analysis, and hence would benefit from comparison to an explicit simulation. This has been done with Bohm SPH, albeit after thermodynamic considerations similar to the previous chapter.

Ions were explicitly included in Bohm SPH that have full energy exchange with the

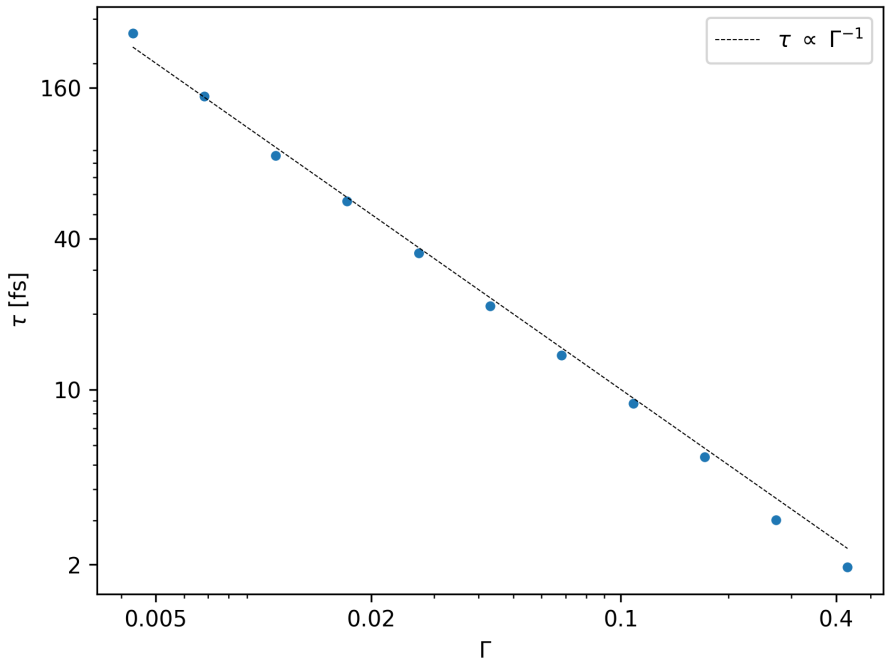


Figure 5.9: Relaxation timescales $\tau$ for Bohm SPH simulations scanning couplings $\Gamma_S$, computed via fitting profiles in Figure 5.8.

SPH particles. While the requirement of having average kernel lengths less than the expected screening length of the plasma ($\overline{h} < \lambda_S$) is slightly relaxed in these simulations (where I am uninterested in the cold ion dynamics) to the requirement that it be less than the ion Wigner Seitz radius $\overline{h} < r_{s_{ii}}\,\mathrm{a_B}$, this still demands a value of $N_{ppe} = 8$ with $\zeta = 1.3 \cdot \sqrt{2}$. Hence there are additional degrees of freedom to the physical situation.

The effect of scanning the resolution $N_{ppe}$ was examined firstly in a constant temperature case, where all simulations sample the same energy distribution $f(E)$ regardless of $N_{ppe}$. This was repeated for a constant thermal energy case, where the energy axis of the sampled distribution is scaled by $1/N_{ppe}$. However, in neither case was convergence observed as $N_{ppe}$ increases, instead the distributions seem to evolve at rates inversely proportional to their SPH Coulomb coupling $\Gamma_S$. That $\Gamma_S$ determines the relaxation in these Bohm SPH simulations was borne out by a scan of resolution while keeping $\Gamma_S$ constant, and subsequently, the $\tau \propto \Gamma_S^{-1}$ relation was demonstrated by scanning a range of couplings and recording the evolution of the ratio $T_{\mathrm{fit}}/T_{\mathrm{eff}}$. Although I em-

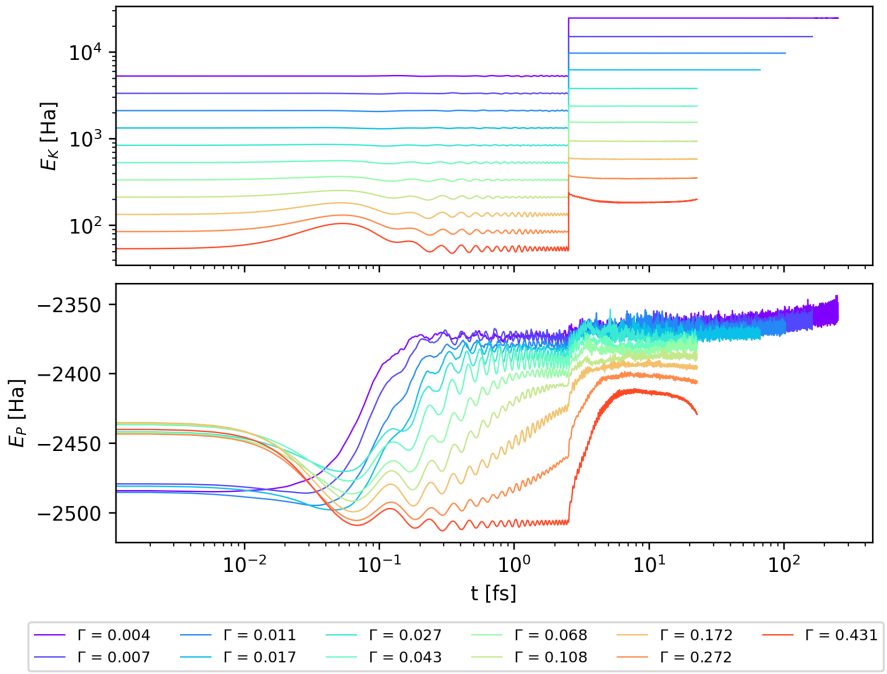


Figure 5.10: Total kinetic (top) and potential (bottom) energies for Bohm SPH simulations scanning couplings $\Gamma_S$. The sampling of the non-thermal electronic distribution occurs instantaneously at 2.5 fs in all cases, after which the system remains in NVE.

phasise that this relation describes the rate of energy transfer into the bulk, and not necessarily the broadening of the non-thermal features.

The dependence of $\tau$ on the SPH coupling motivated that to make a direct comparison between Bohm SPH and Fokker-Planck, the SPH coupling must be set to the electron coupling, which was done for $\Gamma_S = \Gamma_{ee} = 0.291$. Here, the rate of transfer of energy from the non-thermal features into the bulk agreed well, but the broadening of the non-thermal peaks was not equivalent, with Bohm SPH faster. Alongside the $\Gamma_S$ scan outputs, this suggests that there are at least two timescales at play, one which describes the the rate of energy transfer into the bulk, and one which determines the specific broadening of the non-thermal features. Additionally, the near identical $f(E)$ output from Bohm SPH at this coupling with the ion motion disabled demonstrated the relative unimportance of ion-SPH particle energy exchange in these conditions.

The confinement approach of the previous chapter was not explored here. Using confinement potentials is effective for simultaneous computation of ion and electron

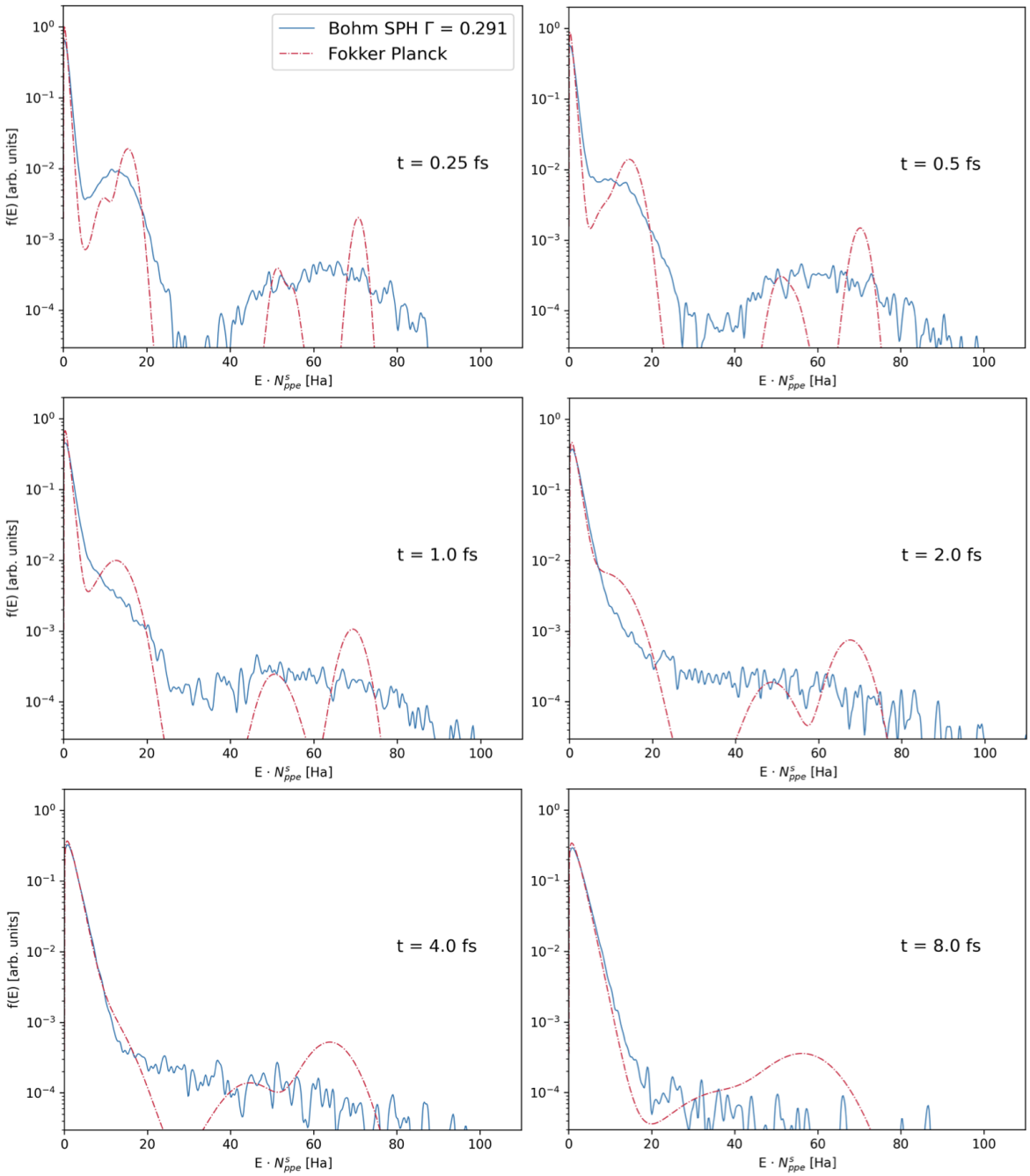


Figure 5.11: Bohm SPH with average particle coupling $\Gamma_S = 0.291$ distributions compared to Fokker-Planck simulation with the same electron coupling, from 0.25 to 8.0 fs. Both distributions are normalised. Due to different sampling frequencies there is a slight time discrepancy with the Bohm SPH outputs 0.01 or 0.02 fs after the Fokker-Planck (plotted times are Fokker-Planck). $N_{ppe} = 8$ for Bohm SPH with scaling value $s = 2.307$ on x axis. No scaling is applied to Fokker-Planck distribution.

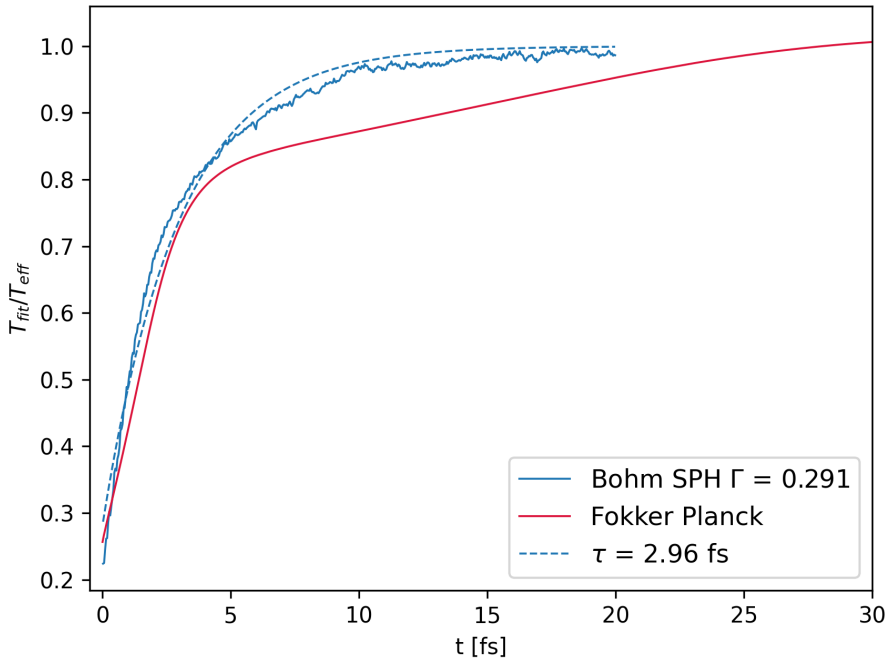


Figure 5.12: Ratio of fitted to effective electronic temperature for Bohm SPH with average particle coupling $\Gamma_S = 0.291$ and Fokker-Planck simulation with the same electron coupling. The value $\tau = 2.96\,\text{fs}$ is computed by fitting Equation (5.3.1).

dynamics, but would be a complication to the thermalisation analysis: adding the confinement strength as a free parameter and forcing the non-thermal $f(E)$ sampling to be for the electron centre of mass velocities.

While the agreement between Bohm SPH at the appropriate coupling and Fokker-Planck was notable for these conditions, in future one may investigate more extreme non-thermal distributions with stronger couplings and where standard formulae for $\ln(\Lambda_{ee})$ become negative, beyond the limits of Fokker-Planck and Spitzer theory. In these situations Bohm SPH may suggest how to adapt $\ln(\Lambda_{ee})$ in the Fokker-Planck operator, and thus CCFLY in its computation of experimental emission spectra.

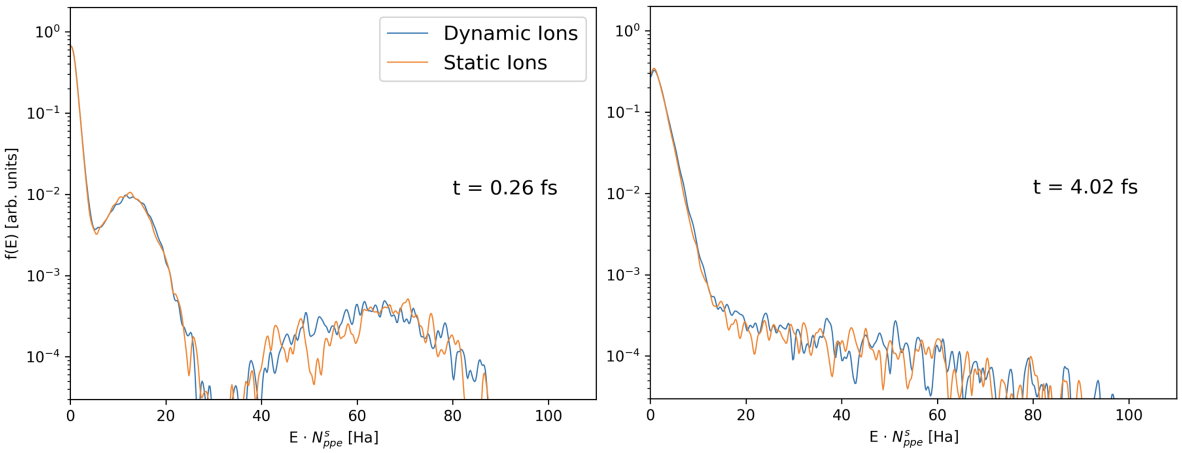


Figure 5.13: Comparison of Bohm SPH distributions with ion motion enabled and disabled at two example times: 0.26 and 4.02 fs. Average particle coupling is $\Gamma_S = 0.291$. $N_{ppe} = 8$ with scaling value $s = -2.307$ on x axis.

# Chapter 6

# Conclusion

I have presented Bohm SPH, a novel code for modelling quantum plasmas, in particular warm dense matter. The code uses a smoothed particle hydrodynamic scheme to resolve the electron density, upon which a quantum hydrodynamic Bohm force is calculated. Furthermore, it introduces a new method for computing the Coulomb interaction amongst SPH particles, as well as using an approximate Pauli potential to capture symmetry effects. With the electron density and ions exchanging energy via the (SPH resolved) Coulomb potential, Bohm SPH is non-adiabatic. This explicit evolution of the electronic component is not only vital to capturing various transport phenomena, but arguably also important to calculating accurate ion dynamics. While Bohm SPH is not a computational free lunch, utilising the LAMMPS structure it has impressive parallel scaling which can be used on high perfomance computing architectures to investigate large warm dense matter systems. Indeed, relatively large ($N_i \sim 10^3$) systems have already been investigated on STFC's SCARF cluster with picosecond durations and sub-attosecond timesteps.

The earlier content of this work describes Bohm SPH in detail, before demonstrating its validity on single-particle wavefunction problems where the Bohm pressure is exact. While of course the QHD Bohm pressure is only approximate for many-particle

systems, this poises the model for application on warm dense matter. However, a problem emerges when simultaneously modelling the ion and electron dynamics in Bohm SPH due to the thermodynamic effect of additional degrees of freedom. These degrees of freedom are introduced to ensure the electron density is well resolved and, as a minimum, the ionic interactions are correctly screened. The use of more SPH particles than there are electrons complicates the concept of temperature/thermal energy in the model if we describe the ions as whole point particles. While there is a certain irony that the non-adiabaticity of Bohm SPH, an important motivating feature, causes this statistical mechanical problem, it clearly applies to any model where the degrees of freedom do not correspond to the physical picture. Particle-in-Cell codes account for this via a global scaling, applicable since the positive and negative macroparticles are treated at the same resolution. In contrast, an equivalent situation to Bohm SPH would be the use of split-wavepacket bases for electrons alongside dynamic whole ions in WPMD simulations, for example. Fortunately, as we have explored in this work, there are schemes to navigate the thermodynamics of this construction of Bohm SPH. Depending on the scheme used, the extraction of at least one of the ionic or electronic dynamics, or both, is possible, ensuring we can still glean important information on the behaviour of warm dense matter.

Warm dense hydrogen ($\Gamma_i = 0.72$, $\theta = 1.32$) was simulated in Chapter 4. By scaling the temperature of the SPH particles by their resolution $1/N_{ppe}$, ion data was extracted that, independent of thermostat parameters, had excellent agreement with a WPMD reference calculation. However this method precluded generation of reasonable electron dynamics, specifically inhibiting calculation of the free electron structure. The introduction of a confining potential to localise electrons, whose centre of mass are then operated on by a thermostat, enabled the simultaneous extraction of ion and electron dynamics. A scan of confinement strengths was investigated, producing a range of average electron sizes. Beyond an interesting insight into how the finite size

of electrons (a quantum diffractive effect) affects dynamic screening in the plasma, this scan showed that best agreement when comparing to WPMD was achieved at the strongest confinement, with impressive agreement of the plasmon.

Electronic thermalisation was tackled in Chapter 5, relevant to XFEL-generated plasma. Here I showed that unless the average Coulomb coupling between SPH particles is kept constant, changing the resolution $N_{ppe}$ affects the thermalisation timescale. This observation was used to justify making a direct comparison between Bohm SPH and the elastic electron Fokker-Planck operator used in CCFLY, provided that the SPH Coulomb coupling was fixed at the physical electron coupling $\Gamma_S = \Gamma_e = 0.291$. Furthermore, an inverse relation between the timescale of transfer of energy from non-thermal features to the Maxwellian bulk and the SPH coupling $\tau \propto \Gamma_S^{-1}$, was confirmed with a scan from weak to moderate coupling values, although an alternative timescale seems to define the specific broadening of non-thermal features. Reasonable agreement between Bohm SPH and Fokker-Planck for $\tau$ at $\Gamma = 0.291$ was observed, despite this moderate coupling being at the expected limit of applicability for Fokker-Planck and Spitzer theory. This result was also replicated when disabling the ion motion in Bohm SPH, indicating the relative unimportance of ion-SPH energy exchange in the system.

## 6.1 Future Work

This section details a number of ideas for future work building on this first iteration of Bohm SPH. A first suggestion is to apply the Bohm SPH framework on further single-particle wavefunction problems where the Bohm pressure is exact. Beyond toy quantum problems which have already been explored with such a scheme [101], one can use the novel SPH coulomb treatment alongside the Bohm for more single-electron ground state calculations. While the relaxation of SPH particle motion was difficult, the convergence of ground state calculations of hydrogen in Chapter 3 are very encouraging.

Now onto small modifications to the existing code structure. First would be to

generalise the SPH Coulomb expressions derived in Chapter 3 to arbitrary kernel shapes, not specifically Gaussian. This would follow a similar form to the SPH expressions for softened gravity [133]. The use of alternative kernels with better compact support, such as the cubic spline mentioned in Chapter 2, would reduce the computation cost of the SPH routines. Next would be to implement SPH-compatible pseudopotential expressions, enabling investigation of higher $Z$ atoms. An attempt has been made to implement these expressions, but an undiagnosed problem with energy conservation means this work was omitted. Finally, the Many-Fermion Bohm potential 3.1.5 is also worth investigating properly, despite the expected unforgiving $N_e^2$ scaling.

Addressing the thermodynamical behaviour of Bohm SPH with SPH particles and ions in an NVE ensemble is clearly a priority. A further idea would be to sub-divide the ion, so that there are $N_{ppe}$ particles describing each ion and each electron. However this would have to be without repeating the poor ionic screening observed with $N_{ppe} = 1$ in Chapter 4, which would be likely to occur if the sub-ion particles are dispersed homogeneously across the simulation domain. A confining potential localising sub-ion particles to single ion centres of mass might avoid this pitfall.

That Bohm SPH could be applied to solve the general quantum hydrodynamic equations is noted in Chapter 2. This is accomplished by assigning each SPH particle a mass (significantly) larger than the electron mass $m_S > m_e$, and introducing an equation of state (additional pressure) to close the dynamical equations. Care would have to be taken on the treatment of the ions, which are typically included as a neutralising homogeneous background in QHD. Adopting the QHD equations would enable investigation of much larger length scales, relevant to metallic nano-objects [100] for example. Of course however, the model would no longer be microscopic and able to make estimations of more accurate equations of state or transport coefficients. Additionally, one could apply a phenomenological exchange-correlation potential as in Ref. [120] borrowed from DFT, or indeed attempt to solve the full Bloch-QHD equations outlined in Ref. [121]

within an SPH structure. When applying a density dependent exchange-correlation potential instead of the purely repulsive Minoo potential, care must be taken that it does not lead to the tensile instability of SPH.

Finally, as a very brief footnote, perhaps Bohm SPH could be modified to become a truly pilot-wave approach, as in the early conceptions of de Broglie. Here the SPH scheme would be used to evolve the $\psi$ field, from which electrons sample the Bohm potential. This is inspired by reading of Ref. [116], where Bohm SPH seems well suited for handling some of the requirements of quantum trajectories approaches, such as adaptive resolution, spatial derivatives, and node handling.

# References


[1] D. Riley. *Warm Dense Matter: laboratory generation and diagnosis*. IOP Publishing, 2021. ISBN: 9780750323468.

[2] K. Falk. "Experimental methods for warm dense matter research". *High Power Laser Science and Engineering*, 6:e59, 2018.

[3] R. Betti and O. Hurricane. "Inertial-confinement fusion with lasers". *Nature Physics*, 12(5):435–448, 2016.

[4] H. Abu-Shawareb, R. Acree, P. Adams, J. Adams, B. Addis, R. Aden, P. Adrian, B. Afeyan, M. Aggleton, L. Aghaian, et al. "Lawson criterion for ignition exceeded in an inertial fusion experiment". *Physical Review Letters*, 129(7):075001, 2022.

[5] H. Abu-Shawareb, R. Acree, P. Adams, J. Adams, B. Addis, R. Aden, P. Adrian, B. Afeyan, M. Aggleton, L. Aghaian, et al. "Achievement of target gain larger than unity in an inertial fusion experiment". *Physical Review Letters*, 132(6): 065102, 2024.

[6] G. I. Kerley. "Equation of state and phase diagram of dense hydrogen". *Physics of the Earth and Planetary Interiors*, 6(1-3):78–82, 1972.

[7] T. Guillot. "Interiors of giant planets inside and outside the solar system". *Science*, 286(5437):72–77, 1999.

[8] N. Nettelmann, B. Holst, A. Kietzmann, M. French, R. Redmer, and D. Blaschke. "Ab initio equation of state data for hydrogen, helium, and water and the internal structure of jupiter". *The Astrophysical Journal*, 683(2):1217, 2008.

[9] J. Daligault and S. Gupta. "Electron–ion scattering in dense multi-component plasmas: Application to the outer crust of an accreting neutron star". *The Astrophysical Journal*, 703(1):994, 2009.

[10] T. Boehly, D. Brown, R. Craxton, R. Keck, J. Knauer, J. Kelly, T. Kessler, S. Kumpan, S. Loucks, S. Letzring, et al. "Initial performance results of the omega laser system". *Optics Communications*, 133(1-6):495–506, 1997.

[11] M. L. Spaeth, K. Manes, D. Kalantar, P. Miller, J. Heebner, E. Bliss, D. Spec, T. Parham, P. Whitman, P. Wegner, et al. "Description of the nif laser". *Fusion Science and Technology*, 69(1):25–145, 2016.

[12] S. Hu, L. Collins, T. Boehly, J. Kress, V. Goncharov, and S. Skupsky. "First-principles thermal conductivity of warm-dense deuterium plasmas for inertial confinement fusion applications". *Physical Review E*, 89(4):043105, 2014.

[13] S. Hu, V. Goncharov, T. Boehly, R. McCrory, S. Skupsky, L. A. Collins, J. D. Kress, and B. Militzer. "Impact of first-principles properties of deuterium–tritium on inertial confinement fusion target designs". *Physics of Plasmas*, 22(5), 2015.

[14] S. Hu, L. Collins, T. Boehly, Y. Ding, P. Radha, V. Goncharov, V. Karasiev, G. Collins, S. Regan, and E. Campbell. "A review on ab initio studies of static, transport, and optical properties of polystyrene under extreme conditions for inertial confinement fusion applications". *Physics of Plasmas*, 25(5), 2018.

[15] B. Fryxell, K. Olson, P. Ricker, F. X. Timmes, M. Zingale, D. Lamb, P. MacNeice, R. Rosner, J. Truran, and H. Tufo. "Flash: An adaptive mesh hydrodynamics code for modeling astrophysical thermonuclear flashes". *The Astrophysical Journal Supplement Series*, 131(1):273, 2000.

[16] M. S. Green. "Markoff random processes and the statistical mechanics of time-dependent phenomena. ii. irreversible processes in fluids". *The Journal of Chemical Physics*, 22(3):398–413, 1954.

[17] R. Kubo. "Statistical-mechanical theory of irreversible processes. i. general theory and simple applications to magnetic and conduction problems". *Journal of the Physical Society of Japan*, 12(6):570–586, 1957.

[18] M. Bonitz, J. Vorberger, M. Bethkenhagen, M. P. Böhme, D. M. Ceperley, A. Filinov, T. Gawne, F. Graziani, G. Gregori, P. Hamann, et al. "Toward first principles-based simulations of dense hydrogen". *Physics of Plasmas*, 31(11), 2024.

[19] P. E. Grabowski, A. Markmann, I. V. Morozov, I. A. Valuev, C. A. Fichtl, D. F. Richards, V. S. Batista, F. R. Graziani, and M. S. Murillo. "Wave packet spreading and localization in electron-nuclear scattering". *Physical Review E*, 87(6): 063104, 2013.

[20] J. P. Mithen, J. Daligault, and G. Gregori. "Extent of validity of the hydrodynamic description of ions in dense plasmas". *Physical Review E*, 83(1):015401, 2011.

[21] H. Kählert. "Thermodynamic and transport coefficients from the dynamic structure factor of yukawa liquids". *Physical Review Research*, 2(3):033287, 2020.

[22] G. Kelbg. "Theorie des quanten-plasmas". *Annalen der Physik*, 467(3-4):219–224, 1963.

[23] H. Minoo, M. Gombert, and C. Deutsch. "Temperature-dependent coulomb interactions in hydrogenic systems". *Physical Review A*, 23(2):924, 1981.

[24] A. Filinov, M. Bonitz, and W. Ebeling. "Improved kelbg potential for correlated coulomb systems". *Journal of Physics A: Mathematical and General*, 36(22):5957, 2003.

[25] B. Larder, D. O. Gericke, S. Richardson, P. Mabey, T. White, and G. Gregori. "Fast nonadiabatic dynamics of many-body quantum systems". *Science Advances*, 5(11):eaaw1634, 2019.

[26] E. J. Heller. "Time-dependent approach to semiclassical dynamics". *The Journal of Chemical Physics*, 62(4):1544–1555, 1975.

[27] H. Feldmeier. "Fermionic molecular dynamics". *Nuclear Physics A*, 515(1):147–172, 1990.

[28] M. Knaup, P. Reinhard, C. Toepffer, and G. Zwicknagel. "Wave packet molecular dynamics simulations of warm dense hydrogen". *Journal of Physics A: Mathematical and General*, 36(22):6165, 2003.

[29] D. Michta, F. Graziani, and M. Bonitz. "Quantum hydrodynamics for plasmas–a thomas-fermi theory perspective". *Contributions to Plasma Physics*, 55(6):437–443, 2015.

[30] Z. A. Moldabekov, M. Bonitz, and T. Ramazanov. "Theoretical foundations of quantum hydrodynamics for plasmas". *Physics of Plasmas*, 25(3), 2018.

[31] T. White, S. Richardson, B. Crowley, L. Pattison, J. Harris, and G. Gregori. "Orbital-free density-functional theory simulations of the dynamic structure factor of warm dense aluminum". *Physical Review Letters*, 111(17):175002, 2013.

[32] H. R. Rüter and R. Redmer. "Ab initio simulations for the ion-ion structure factor of warm dense aluminum". *Physical Review Letters*, 112(14):145007, 2014.

[33] C. Starrett and D. Saumon. "Fully variational average atom model with ion-ion correlations". *Physical Review E—Statistical, Nonlinear, and Soft Matter Physics*, 85(2):026403, 2012.

[34] C. Starrett and D. Saumon. "A simple method for determining the ionic structure of warm dense matter". *High Energy Density Physics*, 10:35–42, 2014.

[35] M. A. Marques and E. K. Gross. "Time-dependent density functional theory". *Annu. Rev. Phys. Chem.*, 55(1):427–455, 2004.

[36] C. A. Ullrich. *Time-Dependent Density-Functional Theory: Concepts and Applications*. OUP Oxford, 2011. ISBN: 9780199563029.

[37] A. D. Baczewski, L. Shulenburger, M. Desjarlais, S. Hansen, and R. Magyar. "X-ray thomson scattering in warm dense matter without the chihara decomposition". *Physical Review Letters*, 116(11):115004, 2016.

[38] S. Hu, B. Militzer, V. Goncharov, S. Skupsky, et al. "First-principles equation-of-state table of deuterium for inertial confinement fusion applications". *Physical Review B*, 84(22):224109, 2011.

[39] T. Dornheim, S. Groth, and M. Bonitz. "The uniform electron gas at warm dense matter conditions". *Physics Reports*, 744:1–86, 2018.

[40] M. Bonitz, T. Dornheim, Z. A. Moldabekov, S. Zhang, P. Hamann, H. Kählert, A. Filinov, K. Ramakrishna, and J. Vorberger. "Ab initio simulation of warm dense matter". *Physics of Plasmas*, 27(4), 2020.

[41] B. Militzer, F. González-Cataldo, S. Zhang, K. P. Driver, and F. Soubiran. "First-principles equation of state database for warm dense matter computation". *Physical Review E*, 103(1):013203, 2021.

[42] L. B. Fletcher, J. Vorberger, W. Schumaker, C. Ruyer, S. Goede, E. Galtier, U. Zastrau, E. P. Alves, S. D. Baalrud, R. A. Baggott, et al. "Electron-ion temperature relaxation in warm dense hydrogen observed with picosecond resolved x-ray scattering". *Frontiers in Physics*, 10:838524, 2022.

[43] T. G. White, J. Dai, and D. Riley. "Dynamic and transient processes in warm dense matter". *Philosophical Transactions of the Royal Society A*, 381(2253): 20220223, 2023.

[44] A. Turrell, M. Sherlock, and S. Rose. "Ultrafast collisional ion heating by electrostatic shocks". *Nature Communications*, 6(1):8905, 2015.

[45] A. Levy, P. Audebert, R. Shepherd, J. Dunn, M. Cammarata, O. Ciricosta, F. Deneuville, F. Dorchies, M. Fajardo, C. Fourment, et al. "The creation of large-volume, gradient-free warm dense matter with an x-ray free-electron laser". *Physics of Plasmas*, 22(3), 2015.

[46] S. H. Glenzer and R. Redmer. "X-ray thomson scattering in high energy density plasmas". *Reviews of Modern Physics*, 81(4):1625, 2009.

[47] L. Fletcher, A. Kritcher, A. Pak, T. Ma, T. Döppner, C. Fortmann, L. Divol, O. Jones, O. Landen, H. Scott, et al. "Observations of continuum depression in warm dense matter with x-ray thomson scattering". *Physical Review Letters*, 112 (14):145004, 2014.

[48] H. Poole, D. Cao, R. Epstein, I. Golovkin, T. Walton, S. Hu, M. Kasim, S. Vinko, J. Rygg, V. Goncharov, et al. "A case study of using x-ray thomson scattering to diagnose the in-flight plasma conditions of dt cryogenic implosions". *Physics of Plasmas*, 29(7), 2022.

[49] P. Mabey, S. Richardson, T. White, L. Fletcher, S. Glenzer, N. Hartley, J. Vorberger, D. O. Gericke, and G. Gregori. "A strong diffusive ion mode in dense ionized matter predicted by langevin dynamics". *Nature Communications*, 8(1): 14125, 2017.

[50] Y. Yao, Q. Zeng, K. Chen, D. Kang, Y. Hou, Q. Ma, and J. Dai. "Reduced ionic diffusion by the dynamic electron–ion collisions in warm dense hydrogen". *Physics of Plasmas*, 28(1), 2021.

[51] J. T. Su and W. A. Goddard. "The dynamics of highly excited electronic systems: Applications of the electron force field". *The Journal of Chemical Physics*, 131 (24), 2009.

[52] W. A. Angermeier and T. G. White. "An investigation into the approximations used in wave packet molecular dynamics for the study of warm dense matter". *Plasma*, 4(2):294–308, 2021.

[53] W. A. Angermeier, B. S. Scheiner, N. R. Shaffer, and T. G. White. "Disentangling the effects of non-adiabatic interactions upon ion self-diffusion within warm dense hydrogen". *Philosophical Transactions of the Royal Society A*, 381(2253): 20230034, 2023.

[54] T. G. White, H. Poole, E. E. McBride, M. Oliver, A. Descamps, L. B. Fletcher, W. A. Angermeier, C. H. Allen, K. Appel, F. P. Condamine, et al. "Speed of sound in methane under conditions of planetary interiors". *Physical Review Research*, 6 (2):L022029, 2024.

[55] S. A. Khan and M. Bonitz. "Quantum hydrodynamics". *Complex plasmas: Scientific Challenges and Technological opportunities*, pages 103–152, 2014.

[56] P. E. Grabowski. "A review of wave packet molecular dynamics". *Frontiers and Challenges in Warm Dense Matter*, pages 265–282, 2014.

[57] H. Feldmeier and J. Schnack. "Molecular dynamics for fermions". *Reviews of Modern Physics*, 72(3):655, 2000.

[58] P. Svensson, T. Campbell, F. Graziani, Z. Moldabekov, N. Lyu, V. S. Batista, S. Richardson, S. M. Vinko, and G. Gregori. "Development of a new quantum trajectory molecular dynamics framework". *Philosophical Transactions of the Royal Society A*, 381(2253):20220325, 2023.

[59] D. Bohm. "A suggested interpretation of the quantum theory in terms of" hidden" variables. i". *Physical Review*, 85(2):166, 1952.

[60] L. De Broglie. "Onde et quanta". *Compte Rendus*, 177:507–510, 1923.

[61] E. Madelung. "Quantum theory in hydrodynamical form". *z. Phys*, 40:322, 1927.

[62] J.-P. Hansen and I. R. McDonald. *Theory of Simple Liquids: with Applications to Soft Matter*. Academic press, 2013. ISBN: 9780080455075.

[63] K. Sturm. "Dynamic structure factor: An introduction". *Zeitschrift für Naturforschung A*, 48(1-2):233–242, 1993.

[64] G. Gregori and D. O. Gericke. "Low frequency structural dynamics of warm dense matter". *Physics of Plasmas*, 16(5), 2009.

[65] L. Van Hove. "Correlations in space and time and born approximation scattering in systems of interacting particles". *Physical Review*, 95(1):249, 1954.

[66] J. Mithen. *Molecular dynamics simulations of the equilibrium dynamics of non-ideal plasmas*. PhD thesis, Oxford University, UK, 2012.

[67] J. Wax and T. Bryk. "An effective fitting scheme for the dynamic structure of pure liquids". *Journal of Physics: Condensed Matter*, 25(32):325104, 2013.

[68] M. Schörner, H. R. Rüter, M. French, and R. Redmer. "Extending ab initio simulations for the ion-ion structure factor of warm dense aluminum to the hydrodynamic limit using neural network potentials". *Physical Review B*, 105(17): 174310, 2022.

[69] J. Chihara. "Difference in x-ray scattering between metallic and non-metallic liquids due to conduction electrons". *Journal of Physics F: Metal Physics*, 17(2): 295, 1987.

[70] J. Chihara. "Interaction of photons with plasmas and liquid metals-photoabsorption and scattering". *Journal of Physics: Condensed Matter*, 12(3): 231, 2000.

[71] P. Svensson, Y. Aziz, T. Dornheim, S. Azadi, P. Hollebon, A. Skelt, S. M. Vinko, and G. Gregori. "Modeling of warm dense hydrogen via explicit real-time electron dynamics: Dynamic structure factors". *Physical Review E*, 110(5):055205, 2024.

[72] J. J. Monaghan. "Smoothed particle hydrodynamics". *Reports on Progress in Physics*, 68(8):1703, 2005.

[73] S. Rosswog. "Astrophysical smooth particle hydrodynamics". *New Astronomy Reviews*, 53(4-6):78–104, 2009.

[74] M. Liu and G. Liu. "Smoothed particle hydrodynamics (sph): an overview and recent developments". *Archives of Computational Methods in Engineering*, 17: 25–76, 2010.

[75] V. Springel. "Smoothed particle hydrodynamics in astrophysics". *Annual Review of Astronomy and Astrophysics*, 48:391–430, 2010.

[76] J. J. Monaghan. "Smoothed particle hydrodynamics and its diverse applications". *Annual Review of Fluid Mechanics*, 44:323–346, 2012.

[77] R. A. Gingold and J. J. Monaghan. "Smoothed particle hydrodynamics: theory and application to non-spherical stars". *Monthly Notices of the Royal Astronomical Society*, 181(3):375–389, 1977.

[78] L. B. Lucy. "A numerical approach to the testing of the fission hypothesis". *Astronomical Journal, vol. 82, Dec. 1977, p. 1013-1024.*, 82:1013–1024, 1977.

[79] J. J. Monaghan. "Smoothed particle hydrodynamics". *In: Annual Review of Astronomy and Astrophysics. Vol. 30 (A93-25826 09-90), p. 543-574.*, 30:543–574, 1992.

[80] J. J. Monaghan and J. C. Lattanzio. "A refined particle method for astrophysical problems". *Astronomy and Astrophysics (ISSN 0004-6361), vol. 149, no. 1, Aug. 1985, p. 135-143.*, 149:135–143, 1985.

[81] M. Liu, G. Liu, and K. Lam. "Constructing smoothing functions in smoothed particle hydrodynamics with applications". *Journal of Computational and Applied Mathematics*, 155(2):263–284, 2003.

[82] I. J. Schoenberg. "Contributions to the problem of approximation of equidistant data by analytic functions. part b. on the problem of osculatory interpolation. a second class of analytic approximation formulae". *Quarterly of Applied Mathematics*, 4(2):112–141, 1946.

[83] M. S. Fulbright, W. Benz, and M. B. Davies. "A method of smoothed particle hydrodynamics using spheroidal kernels". *Astrophysical Journal, Part 1 (ISSN 0004-637X), vol. 440, no. 1, p. 254-262*, 440:254–262, 1995.

[84] P. R. Shapiro, H. Martel, J. V. Villumsen, and J. M. Owen. "Adaptive smoothed particle hydrodynamics, with application to cosmology: methodology". *Astrophysical Journal Supplement v. 103, p. 269*, 103:269, 1996.

[85] J. M. Owen, J. V. Villumsen, P. R. Shapiro, and H. Martel. "Adaptive smoothed particle hydrodynamics: Methodology. ii.". *The Astrophysical Journal Supplement Series*, 116(2):155, 1998.

[86] M. Liu and G. Liu. "Meshfree particle simulation of micro channel flows with surface tension". *Computational Mechanics*, 35:332–341, 2005.

[87] S. Mas-Gallic and P. Raviart. "A particle method for first-order symmetric systems". *Numerische Mathematik*, 51(3):323–352, 1987.

[88] R. Fatehi and M. T. Manzari. "Error estimation in smoothed particle hydrodynamics and a new scheme for second derivatives". *Computers & Mathematics with Applications*, 61(2):482–498, 2011.

[89] B. Ben Moussa and J. P. Vila. "Convergence of sph method for scalar nonlinear conservation laws". *SIAM Journal on Numerical Analysis*, 37(3):863–887, 2000.

[90] M. J. Berger and P. Colella. "Local adaptive mesh refinement for shock hydrodynamics". *Journal of Computational Physics*, 82(1):64–84, 1989.

[91] V. Springel and L. Hernquist. "Cosmological smoothed particle hydrodynamics simulations: the entropy equation". *Monthly Notices of the Royal Astronomical Society*, 333(3):649–664, 2002.

[92] L. Hernquist and N. Katz. "Treesph-a unification of sph with the hierarchical tree method". *Astrophysical Journal Supplement Series*, 70:419–446, 1989.

[93] S. Sibilla. "An algorithm to improve consistency in smoothed particle hydrodynamics". *Computers & Fluids*, 118:148–158, 2015.

[94] S. Korzilius, W. H. Schilders, and M. J. Anthonissen. "An improved cspm approach for accurate second-derivative approximations with sph". *Journal of Applied Mathematics and Physics*, 5(1):168–184, 2016.

[95] M. Basa, N. J. Quinlan, and M. Lastiwka. "Robustness and accuracy of sph formulations for viscous flow". *International Journal for Numerical Methods in Fluids*, 60(10):1127–1148, 2009.

[96] J. J. Monaghan. "Sph compressible turbulence". *Monthly Notices of the Royal Astronomical Society*, 335(3):843–852, 2002.

[97] D. J. Price. "Smoothed particle hydrodynamics and magnetohydrodynamics". *Journal of Computational Physics*, 231(3):759–794, 2012.

[98] F. Haas. "A magnetohydrodynamic model for quantum plasmas". *Physics of Plasmas*, 12(6), 2005.

[99] R. Schmidt, B. Crowley, J. Mithen, and G. Gregori. "Quantum hydrodynamics of strongly coupled electron fluids". *Physical Review E—Statistical, Nonlinear, and Soft Matter Physics*, 85(4):046408, 2012.

[100] G. Manfredi, P.-A. Hervieux, and J. Hurst. "Fluid descriptions of quantum plasmas". *Reviews of Modern Plasma Physics*, 5:1–38, 2021.

[101] P. Mocz and S. Succi. "Numerical solution of the nonlinear schrödinger equation using smoothed-particle hydrodynamics". *Physical Review E*, 91(5):053304, 2015.

[102] D. Bohm. "A Suggested Interpretation of the Quantum Theory in Terms of "Hidden" Variables. II". *Physical Review*, 85(2):180–193, 1952. doi: 10.1103/PhysRev.85.180.

[103] A. Einstein, B. Podolsky, and N. Rosen. "Can quantum-mechanical description of physical reality be considered complete?". *Physical Review*, 47(10):777, 1935.

[104] N. Bohr. "Can quantum-mechanical description of physical reality be considered complete?". *Physical Review*, 48(8):696, 1935.

[105] D. Bohm. "Proof that probability density approaches— $\psi$— 2 in causal interpretation of the quantum theory". *Physical Review*, 89(2):458, 1953.

[106] D. Bohm and J.-P. Vigier. "Model of the causal interpretation of quantum theory in terms of a fluid with irregular fluctuations". *Physical Review*, 96(1):208, 1954.

[107] A. Valentini and H. Westman. "Dynamical origin of quantum probabilities". *Proceedings of the Royal Society A: Mathematical, Physical and Engineering Sciences*, 461(2053):253–272, 2005.

[108] M. Towler, N. Russell, and A. Valentini. "Time scales for dynamical relaxation to the born rule". *Proceedings of the Royal Society A: Mathematical, Physical and Engineering Sciences*, 468(2140):990–1013, 2012.

[109] A. Valentini. "Astrophysical and cosmological tests of quantum theory". *Journal of Physics A: Mathematical and Theoretical*, 40(12):3285, 2007.

[110] E. Wigner. "On the quantum correction for thermodynamic equilibrium". *Physical Review*, 40(5):749, 1932.

[111] J. E. Moyal. "Quantum mechanics as a statistical theory". In *Mathematical Proceedings of the Cambridge Philosophical Society*, volume 45, pages 99–124. Cambridge University Press, 1949.

[112] T. Takabayasi. "The formulation of quantum mechanics in terms of ensemble in phase space". *Progress of Theoretical Physics*, 11(4-5):341–373, 1954.

[113] V. Tatarskiĭ. "The wigner representation of quantum mechanics". *Soviet Physics Uspekhi*, 26(4):311, 1983.

[114] G. Manfredi, P.-A. Hervieux, and J. Hurst. "Phase-space modeling of solid-state plasmas: A journey from classical to quantum". *Reviews of Modern Plasma Physics*, 3(1):13, 2019.

[115] M. Bonitz, Z. A. Moldabekov, and T. Ramazanov. "Quantum hydrodynamics for plasmas—quo vadis?". *Physics of Plasmas*, 26(9), 2019.

[116] R. E. Wyatt. *Quantum Dynamics with Trajectories: Introduction to Quantum Hydrodynamics*, volume 28. Springer Science & Business Media, 2005. ISBN: 9780387281452.

[117] G. Manfredi and F. Haas. "Self-consistent fluid model for a quantum electron gas". *Physical Review B*, 64(7):075316, 2001.

[118] G. Manfredi. "How to model quantum plasmas". *Fields Inst. Commun*, 46:263–287, 2005.

[119] F. Haas. *Quantum Plasmas: An Hydrodynamic Approach*, volume 65. Springer Science & Business Media, 2011. ISBN: 9781441982018.

[120] N. Crouseilles, P.-A. Hervieux, and G. Manfredi. "Quantum hydrodynamic model for the nonlinear electron dynamics in thin metal films". *Physical Review B—Condensed Matter and Materials Physics*, 78(15):155412, 2008.

[121] D. Michta. *Quantum hydrodynamics: theory and computation with applications to charged particle stopping in warm dense matter*. PhD thesis, Princeton University, 2020.

[122] M. Bonitz. *Quantum Kinetic Theory*, volume 412. Springer, 2016. ISBN: 9783319342603.

[123] W. Jones and W. Young. "Density functional theory and the von weizsacker method". *Journal of Physics C: Solid State Physics*, 4(11):1322, 1971.

[124] A. Kompaneets and E. Pavlovskii. "The self-consistent field equations in an atom". *Sov. Phys. JETP*, 4(328):17, 1957.

[125] D. Kirzhnits. "Quantum corrections to the thomas-fermi equation". *Soviet Phys. JETP*, 5, 1957.

[126] Z. Moldabekov, T. Schoof, P. Ludwig, M. Bonitz, and T. Ramazanov. "Statically screened ion potential and bohm potential in a quantum plasma". *Physics of Plasmas*, 22(10), 2015.

[127] B. Larder. *Prediction and inference of dynamics in quantum plasmas*. PhD thesis, University of Oxford, 2020.

[128] N. Metropolis, A. W. Rosenbluth, M. N. Rosenbluth, A. H. Teller, and E. Teller. "Equation of state calculations by fast computing machines". *The journal of Chemical Physics*, 21(6):1087–1092, 1953.

[129] P. K. Shukla and B. Eliasson. "Novel attractive force between ions in quantum plasmas". *Physical Review Letters*, 108(16):165007, 2012.

[130] M. Bonitz, E. Pehlke, and T. Schoof. "Attractive forces between ions in quantum plasmas: Failure of linearized quantum hydrodynamics". *Physical Review E—Statistical, Nonlinear, and Soft Matter Physics*, 87(3):033105, 2013.

[131] F. Haas, G. Manfredi, and M. Feix. "Multistream model for quantum plasmas". *Physical Review E*, 62(2):2763, 2000.

[132] Z. Moldabekov, T. Dornheim, G. Gregori, F. Graziani, M. Bonitz, and A. Cangi. "Towards a quantum fluid theory of correlated many-fermion systems from first principles". *SciPost Physics*, 12(2):062, 2022.

[133] D. J. Price and J. J. Monaghan. "An energy-conserving formalism for adaptive gravitational force softening in smoothed particle hydrodynamics and n-body codes". *Monthly Notices of the Royal Astronomical Society*, 374(4):1347–1358, 2007.

[134] S. W. de Leeuw, J. W. Perram, and E. R. Smith. "Simulation of electrostatic systems in periodic boundary conditions. i. lattice sums and dielectric constants". *Proceedings of the Royal Society of London. A. Mathematical and Physical Sciences*, 373(1752):27–56, 1980.

[135] T. Darden, D. York, and L. Pedersen. "Particle mesh ewald: An n log (n) method for ewald sums in large systems". *The Journal of Chemical Physics*, 98(12):10089–10092, 1993.

[136] M. Deserno and C. Holm. "How to mesh up ewald sums. i. a theoretical and numerical comparison of various particle mesh routines". *The Journal of Chemical Physics*, 109(18):7678–7693, 1998.

[137] A. Filinov, V. Golubnychiy, M. Bonitz, W. Ebeling, and J. Dufty. "Temperature-dependent quantum pair potentials and their application to dense partially ionized hydrogen plasmas". *Physical Review E—Statistical, Nonlinear, and Soft Matter Physics*, 70(4):046411, 2004.

[138] J. Hansen and I. McDonald. "Thermal relaxation in a strongly coupled two-temperature plasma". *Physics Letters A*, 97(1-2):42–44, 1983.

[139] J. Glosli, F. Graziani, R. More, M. Murillo, F. Streitz, M. Surh, L. Benedict, S. Hau-Riege, A. Langdon, and R. London. "Molecular dynamics simulations of temperature equilibration in dense hydrogen". *Physical Review E*, 78(2):025401, 2008.

[140] J. P. Morris. *Analysis of smoothed particle hydrodynamics with applications*. PhD thesis, Monash University Australia, 1996.

[141] J. J. Monaghan. "Sph without a tensile instability". *Journal of Computational Physics*, 159(2):290–311, 2000.

[142] L. Brey, J. Dempsey, N. F. Johnson, and B. Halperin. "Infrared optical absorption in imperfect parabolic quantum wells". *Physical Review B*, 42(2):1240, 1990.

[143] L. Hedin and B. I. Lundqvist. "Explicit local exchange-correlation potentials". *Journal of Physics C: Solid State Physics*, 4(14):2064, 1971.

[144] P. A. Dirac. "Note on exchange phenomena in the thomas atom". In *Mathematical Proceedings of the Cambridge Philosophical Society*, volume 26, pages 376–385. Cambridge University Press, 1930.

[145] K. Burke, J. Werschnik, and E. Gross. "Time-dependent density functional theory: Past, present, and future". *The Journal of Chemical Physics*, 123(6), 2005.

[146] M. Bonitz, A. Filinov, J.-W. Abraham, K. Balzer, H. Kählert, E. Pehlke, F. X. Bronold, M. Pamperin, M. Becker, D. Loffhagen, et al. "Towards an integrated modeling of the plasma-solid interface". *Frontiers of Chemical Science and Engineering*, 13:201–237, 2019.

[147] J. M. Dawson. "Particle simulation of plasmas". *Reviews of Modern Physics*, 55 (2):403, 1983.

[148] M. D. Acciarri, C. Moore, L. P. Beving, and S. D. Baalrud. "When should pic simulations be applied to atmospheric pressure plasmas? impact of correlation heating". *Plasma Sources Science and Technology*, 33(3):035009, 2024.

[149] L. Bai and D. Breen. "Calculating center of mass in an unbounded 2d environment". *Journal of Graphics Tools*, 13(4):53–60, 2008.

[150] A. P. Thompson, H. M. Aktulga, R. Berger, D. S. Bolintineanu, W. M. Brown, P. S. Crozier, P. J. In't Veld, A. Kohlmeyer, S. G. Moore, T. D. Nguyen, et al. "Lammps-a flexible simulation tool for particle-based materials modeling at the atomic, meso, and continuum scales". *Computer Physics Communications*, 271: 108171, 2022.

[151] D. J. Evans and B. L. Holian. "The nose–hoover thermostat". *The Journal of Chemical Physics*, 83(8):4069–4074, 1985.

[152] G. C. Ganzenmüller, M. O. Steinhauser, P. Van Liedekerke, and K. U. Leuven. "The implementation of smooth particle hydrodynamics in lammps". *Paul Van Liedekerke Katholieke Universiteit Leuven*, 1(1-26):31, 2011.

[153] M. Baus and J.-P. Hansen. "Statistical mechanics of simple coulomb systems". *Physics Reports*, 59(1):1–94, 1980.

[154] Z. A. Moldabekov, S. Groth, T. Dornheim, H. Kählert, M. Bonitz, and T. Ramazanov. "Structural characteristics of strongly coupled ions in a dense quantum plasma". *Physical Review E*, 98(2):023207, 2018.

[155] G. Gregori, A. Ravasio, A. Höll, S. Glenzer, and S. Rose. "Derivation of the static structure factor in strongly coupled non-equilibrium plasmas for x-ray scattering studies". *High Energy Density Physics*, 3(1-2):99–108, 2007.

[156] D. Pines. *Theory of Quantum Liquids: Normal Fermi Liquids*. CRC Press, 2018. ISBN: 9780429961212.

[157] D. Pines and D. Bohm. "A collective description of electron interactions: Ii. collective vs individual particle aspects of the interactions". *Physical Review*, 85 (2):338, 1952.

[158] T. Dornheim, S. Groth, J. Vorberger, and M. Bonitz. "Ab initio path integral monte carlo results for the dynamic structure factor of correlated electrons: From the electron liquid to warm dense matter". *Physical Review Letters*, 121(25): 255001, 2018.

[159] C. Fortmann, A. Wierling, and G. Röpke. "Influence of local-field corrections on thomson scattering in collision-dominated two-component plasmas". *Physical Review E—Statistical, Nonlinear, and Soft Matter Physics*, 81(2):026405, 2010.

[160] S. Ichimaru. "Strongly coupled plasmas: high-density classical plasmas and degenerate electron liquids". *Reviews of Modern Physics*, 54(4):1017, 1982.

[161] G. Gregori, S. Glenzer, and O. Landen. "Strong coupling corrections in the analysis of x-ray thomson scattering measurements". *Journal of Physics A: Mathematical and General*, 36(22):5971, 2003.

[162] R. Thiele, T. Bornath, C. Fortmann, A. Höll, R. Redmer, H. Reinholz, G. Röpke, A. Wierling, S. Glenzer, and G. Gregori. "Plasmon resonance in warm dense matter". *Physical Review E—Statistical, Nonlinear, and Soft Matter Physics*, 78 (2):026411, 2008.

[163] Y.-F. Shi, S. Ren, H.-K. Chung, J. S. Wark, and S. M. Vinko. "Exploring relaxation dynamics in warm dense plasmas by tailoring non-thermal electron distributions with a free electron laser". *Physics of Plasmas*, 31(8), 2024.

[164] C. Bostedt, S. Boutet, D. M. Fritz, Z. Huang, H. J. Lee, H. T. Lemke, A. Robert, W. F. Schlotter, J. J. Turner, and G. J. Williams. "Linac coherent light source: The first five years". *Reviews of Modern Physics*, 88(1):015007, 2016.

[165] Z. Huang and K.-J. Kim. "Review of x-ray free-electron laser theory". *Physical Review Special Topics—Accelerators and Beams*, 10(3):034801, 2007.

[166] P. Emma, R. Akre, J. Arthur, R. Bionta, C. Bostedt, J. Bozek, A. Brachmann, P. Bucksbaum, R. Coffee, F.-J. Decker, et al. "First lasing and operation of an ångstrom-wavelength free-electron laser". *Nature Photonics*, 4(9):641–647, 2010.

[167] S. Vinko, O. Ciricosta, B. Cho, K. Engelhorn, H.-K. Chung, C. Brown, T. Burian, J. Chalupskỳ, R. Falcone, C. Graves, et al. "Creation and diagnosis of a solid-density plasma with an x-ray free-electron laser". *Nature*, 482(7383):59–62, 2012.

[168] O. Ciricosta, S. Vinko, B. Barbrel, D. Rackstraw, T. Preston, T. Burian, J. Chalupskỳ, B. I. Cho, H.-K. Chung, G. Dakovski, et al. "Measurements of continuum lowering in solid-density plasmas created from elements and compounds". *Nature Communications*, 7(1):11713, 2016.

[169] S. Ren, Y. Shi, Q. Y. van den Berg, M. F. Kasim, H.-K. Chung, E. V. Fernandez-Tello, P. Velarde, J. S. Wark, and S. M. Vinko. "Non-thermal evolution of dense plasmas driven by intense x-ray fields". *Communications Physics*, 6(1):99, 2023.

[170] H.-K. Chung, M. Chen, and R. Lee. "Extension of atomic configuration sets of the non-lte model in the application to the k$\alpha$ diagnostics of hot dense matter". *High Energy Density Physics*, 3(1-2):57–64, 2007.

[171] O. Ciricosta, H.-K. Chung, R. W. Lee, and J. S. Wark. "Simulations of neon irradiated by intense x-ray laser radiation". *High Energy Density Physics*, 7(3): 111–116, 2011.

[172] H.-K. Chung, M. Chen, W. Morgan, Y. Ralchenko, and R. Lee. "Flychk: Generalized population kinetics and spectral model for rapid spectroscopic analysis for all elements". *High Energy Density Physics*, 1(1):3–12, 2005.

[173] M. N. Rosenbluth, W. M. MacDonald, and D. L. Judd. "Fokker-planck equation for an inverse-square force". *Physical Review*, 107(1):1, 1957.

[174] M. Tzoufras, A. Bell, P. Norreys, and F. S. Tsung. "A vlasov–fokker–planck code for high energy density physics". *Journal of Computational Physics*, 230(17): 6475–6494, 2011.

[175] M. Tzoufras, A. Tableman, F. Tsung, W. Mori, and A. Bell. "A multi-dimensional vlasov-fokker-planck code for arbitrarily anisotropic high-energy-density plasmas". *Physics of Plasmas*, 20(5), 2013.

[176] J. D. Huba. *NRL Plasma Formulary*, volume 6790. Naval Research Laboratory, 1998. ISBN: 9781934939017.

[177] L. Spitzer Jr and R. Härm. "Transport phenomena in a completely ionized gas". *Physical Review*, 89(5):977, 1953.

[178] D. Gericke, M. Murillo, and M. Schlanges. "Dense plasma temperature equilibration in the binary collision approximation". *Physical Review E*, 65(3):036418, 2002.

[179] L. Spitzer. *Physics of Fully Ionized Gases*. Courier Corporation, 2006. ISBN: 9780486449821.

[180] Q. Ma, J. Dai, D. Kang, M. Murillo, Y. Hou, Z. Zhao, and J. Yuan. "Extremely low electron-ion temperature relaxation rates in warm dense hydrogen: Interplay between quantum electrons and coupled ions". *Physical Review Letters*, 122(1): 015001, 2019.